**Low Cost Wireless Fatigue Crack
Monitoring System Using RFID Arrays**

Prepared by: Rosana Martínez-Castro, P.E. and Shinae Jang, Ph.D.

University of Connecticut
Connecticut Transportation Institute

Submitted to:
Connecticut Department of Transportation
Research Section

Michael J. Connors

Assistant Director of Policy and Planning

TECHNICAL REPORT DOCUMENTATION PAGE

1. Report No. JHR 18-330	2. Government Accession No.	3. Recipients Catalog No.
4. Title and Subtitle Low Cost Wireless Fatigue Crack Monitoring System Using RFID Arrays		5. Report Date March 2018
		6. Performing Organization Code CCTRP 16-01
7. Author(s) Rosana Martínez-Castro, Shinae Jang		8. Performing Organization Report No. JHR 18-330
9. Performing Organization Name and Address University of Connecticut Connecticut Transportation Institute 270 Middle Turnpike, U-5202 Storrs, Connecticut 06269-5202		10. Work Unit No. (TRIS) N/A
		11. Contract or Grant No.
		13. Type of Report and Period Covered Final Report January 1, 2016 – June 30, 2017
12. Sponsoring Agency Name and Address Connecticut Department of Transportation 2800 Berlin Turnpike Newington, CT 06131-7546		
		14. Sponsoring Agency Code CCTRP 16-01

15. Supplementary Notes

16. Abstract

The use of welded steel cover plates had been a common design practice to increase beam section capacity in regions of high torsion for decades. Many steel girder bridges with cover plates are still in service. Steel girder bridges are subject to cyclic loading, which can initiate crack formation at the toe of the weld and reduce beam capacity. Thus, timely detection of fatigue cracks is of utmost importance in steel girder bridge monitoring. To date, crack monitoring methods using in-house radio frequency identification (RFID)-based sensors have been developed to complement visual inspection and provide quantitative information of damage level. Offering similar properties at a reduced cost, commercial ultra-high frequency (UHF) passive RFID tags have been identified as a more financially viable option for pervasive crack monitoring using a dense array of sensors. This project conducted a study on damage sensitivity of low-cost commercial UHF RFID tags for crack detection and monitoring on metallic structures. Using backscatter power as a parameter for damage identification, a crack sensing system has been developed for single- and multiple-tag configurations for increased sensing pervasiveness. The effect on backscatter power of the existence and stage of crack propagation has been successfully characterized, and compared with digital image correlation. For further automation of crack detection, a damage index based on the variation of backscatter power has also been established. The tested commercial RFID-based crack sensor contributes to the usage of this technology on steel girder bridges.

17. Key Words Bridge Monitoring, Fatigue Crack Monitoring, RFID Sensors		18. Distribution Statement No restrictions. This document is available to the public through the National Technical Information Service, Springfield, VA. 22161	
19. Security Classif. (Of this report) Unclassified	20. Security Classif.(Of this page) Unclassified	21. No. of Pages 115	22. Price N/A

DISCLAIMER

The contents of this report reflect the views of the authors who are responsible for the facts and accuracy of the data presented herein. The contents do not necessarily reflect the official views or policies of the University of Connecticut or the Connecticut Department of Transportation. This report does not constitute a standard, specification or regulation.

ACKNOWLEDGEMENTS

METRIC CONVERSION FACTORS

SYMBOL	WHEN YOU KNOW	MULTIPLY BY	TO FIND	SYMBOL
APPROXIMATE CONVERSIONS TO SI UNITS				
LENGTH				
in	inches	25.4	millimeters	mm
ft	feet	0.305	meters	m
yd	yards	0.914	meters	m
mi	miles	1.61	kilometers	km
AREA				
in^2	square inches	645.2	square millimeters	mm^2
ft^2	square feet	0.093	square meters	m^2
yd^2	square yard	0.836	square meters	m^2
ac	acres	0.405	hectares	ha
mi^2	square miles	2.59	square kilometers	km^2
VOLUME				
fl oz	fluid ounces	29.57	milliliters	mL
gal	gallons	3.785	liters	L
ft^3	cubic feet	0.028	cubic meters	m^3
yd^3	cubic yards	0.765	cubic meters	m^3
NOTE: volumes greater than 1000 L shall be shown in m^3				
MASS				
oz	ounces	28.35	grams	g
lb	pounds	0.454	kilograms	kg
T	short tons (2000 lb)	0.907	megagrams (or "metric ton")	Mg (or "t")
TEMPERATURE (exact degrees)				
^oF	Fahrenheit	5 (F-32)/9 or (F-32)/1.8	Celsius	^oC
ILLUMINATION				
fc	foot-candles	10.76	lux	lx
fl	foot-Lamberts	3.426	candela/m^2	cd/m^2
FORCE and PRESSURE or STRESS				
lbf	poundforce	4.45	newtons	N
lbf/in^2	poundforce per square inch	6.89	kilopascals	kPa

TABLE OF CONTENTS

LIST OF FIGURES

LIST OF TABLES

Executive Summary

The ability to rapidly assess the structural integrity of transportation systems is of critical importance to bridge owners and the public, at large, for elongated service life, reduced maintenance cost, and safety. Our transportation systems typically have everyday cyclic loads, which could induce fatigue crack on the metal structures, which could develop to unexpected sudden failure below the design load. The traditional crack monitoring systems, e.g., nondestructive evaluation or continuous monitoring with fiber optic sensors are typically expensive and require a high level of experience, which hindered widespread use of these monitoring systems for bridge inventory.

In recent years, wireless smart sensors have been state-of-the-art in civil structural health monitoring due to its versatility and low cost. Among them, radio frequency identification (RFID) has drawn attention by researchers to monitor strain and cracks leading their research in this area with in-house developed RFID tags. RFID is the wireless use of electromagnetic fields to transfer data, and is typically used in transportation such as freight tracking, railroads, E-ZPass®, and many other industries. Currently, RFID tags are mass produced at a very low cost, the communication protocols are standardized and efficient, making RFID an ideal wireless communication infrastructure for dense arrays of sensors, i.e., pervasive sensing.

An RFID crack system consists of a passive tag, or tags, attached on a metal surface, and a data acquisition unit. The data acquisition unit typically consists of a PC with software, data logger, and antenna, but it could be replaced by a handheld wireless unit. Once electromagnetic waves are transmitted from the antenna to the tag wirelessly, a portion of the waves are reflected to the antenna back. If there is any damage or cracks, the percentage of the reflected waves changes; i.e.,

the cracks can be detected. This works for an ideal laboratory environment without any interference; however, there are many interferences from the environment and metal surfaces. Damage sensitivity was not studied for commercial RFID tags at all, and if multiple tags are to be used for pervasive sensing, the configuration of tags and possible coupling effects have not been studied.

This project aimed to develop a very low-cost passive wireless crack sensor using commercial RFID tags for crack detection of field metal structures. We developed two configuration of wireless crack sensor using a single RFID tag and multiple RFID tag arrays. To enable communication between the tags and the reader antenna, we found a reasonable substrate material between the tag and the metal surface. Without the substrate material (i.e., if the tag is attached directly on the metal surface), there is no reflected power. A preliminary study to determine a good read distance between the sensor and the antenna was conducted. We found a good read distance is 3 ft or less; however, the sensors were responsive with up to 15 ft read distance. Since the read distance is constant before and after damage, the crack damage was able to be identified by comparing the changes of the received power.

The first major experimental study was on the crack detection capability and sensitivity to damage of both sensor configurations: single-tag and multiple-tag. For a single-tag configuration, the received power decreased in terms of increased damage on the tag sensor showing a good damage sensitivity. For a multiple-tag configuration, we compared the received power of many different arrangements to find the highest received power. For each case, we confirmed the damage sensitivity of multiple sensors. Therefore, the RFID tags sensors were experimentally validated for crack detection.

2

The next important experimental study was on the dynamic crack detection capability of the sensor when a crack is propagating. To do that, we created a standard metal specimen for crack propagation tests, and measured the change of the received power to validate the capability of this crack sensor for dynamic crack. Both single-tag configuration and multiple-tag configuration were employed for crack detection tests under crack propagation until failure. The received power of the RFID tag sensors changes to the crack progression. To give more objective reference, the received power from the RFID tags are matched with digital image correlation. The final results showed that the developed sensors have great potential to effectively detect the existence, location, and the degree of cracks. Therefore, the complete damage sensitivity of the RFID-based crack sensors were successfully validated.

The developed sensors are ready to be installed on any metal structures in the field and tested for its performance. The cost of a single tag is less than 10 cents if mass purchased, the substrate material is cheap EVA foam, rugged exterior adhesive can be used to elongate the life of sensors, and one data acquisition system can be used to scan many tags on multiple bridge sites. Through this project, a handheld reader has been purchased to show the potential to monitor bridges on-site using this equipment easily. Further research on field implementation, crack monitoring with handheld equipment, and autonomous crack detection system; as well as manuals, photos, and test parameters are detailed in the report.

CHAPTER 1. INTRODUCTION AND BACKGROUND

1. Motivation for Crack Monitoring

The ability to rapidly assess the structural integrity of transportation systems is of critical importance to bridge owners and the public, at large, for elongated service life, reduced maintenance cost, and safety. Metal and reinforced concrete (RC) structural systems are major components of our transportation systems, and cracking of the RC material is an intrinsic material problem due to low tensile strength under cyclic loading. The effect of cyclic loading could be more drastic in metal structures due to fatigue, because fatigue may induce progressive and localized structural damage, leading to unexpected sudden failure below the yield stress limit. Therefore, an efficient means for closely monitoring cracks in structural members is required to provide indicators to enable timely maintenance for better performance and elongated service life.

The main issue of fatigue is that the fatigue life is not governed by the ultimate stress limit, but rather by nominal stress range and the fatigue threshold under cyclic loads. Once the stress levels are above a specified threshold, fatigue cracks will initiate at the surface, and the crack will reach a critical size which may induce sudden failure. Typically, crack-prone areas in steel bridges include major connections, orthotropic decks, flange gusset plates, and welded cover plates. Among these, any welded area or welded cover plates are vulnerable to fatigue failure because of reduced strength in a heat-affected zone (HAZ), stress concentration near members with abrupt changes in geometry, or weld defects. The knowledge of material and stress level is crucial; furthermore, the fatigue level must also be experimentally measured.

However, current fatigue crack measurement systems have practical hurdles of cost, installation, and flexibility. To determine fatigue cracking of those plates, suspicious regions have to be first

4

identified during biennial routine visual inspection, mandated by FHWA, and then, further details are determined by subsequent crack-monitoring trips. High-quality fatigue-monitoring systems are often expensive, including sensors, data acquisition systems, and cables. The installation and maintenance of cables are more difficult and time/labor consuming in the field with expensive bucket truck usage. With the high cost and effort, the sensing system should remain on the specific bridge as a permanent installation on the structure. Furthermore, the strain data should be processed in a PC after data storage; long cables may cause additional noise; power line should be re-organized to supply power to the sensing systems; and other practical issues.

Wireless sensor networks (WSN) are state-of-the-art and have great potential to solve these issues of high costs and difficulty in installing sensors and cables. Recently, there has been interest in developing network of sensors using RFID (Radio-frequency identification) tags. RFID is the wireless use of electromagnetic fields to transfer data, and is typically used in transportation such as freight tracking, railroads, E-ZPass® tollbooths, and many other industries. Currently, RFID tags are mass produced at a very low cost. Furthermore, the communication protocols between the RFID tag and the reader are standardized and efficient, making RFID an ideal wireless communication infrastructure for dense arrays of sensors, i.e., pervasive sensing. Applications of RFID in sensing are getting broader, which include the measurement of strain, displacement, temperature, fluid level, moisture, etc. The RFID-based WSN offers various advantages to the traditional sensing technology including cost effectiveness, convenient installation, and easy scanning using any inspection vehicles in service. Therefore, the WSN-RFID can provide a means to provide convenient data and information to monitor fatigue-induced cracks of metal structures with low cost, convenience, and time efficiency.

2. Background

Traditionally, highway bridges use various types of steel welded beams for structural members. Cover plates are plates added to the flanges of beams to increase the flexural capacity of the beam [1] (see Figure 1.1). The use of cover plates in regions of high moment allows the use of a section of primary beam with lesser weight, lesser flexural capacity and lower cost [2 , 3]. However, the use of welded cover plates introduces a transverse weld periphery ('toe'), forming a line of elevated tension, where a crack can initialize and grow, resulting in earlier fatigue cracks on the plates or even on the main beams of which those plates were attached. Fisher *et al.*, [4] noted that fatigue crack propagation at nearly all other structural details occurred as cracks initiated from the toe of fillet or groove welds because of high stress concentration due to discontinuity and residual tension stress. Thus, welded cover-plated beams could more easily gain fatigue cracks than rolled beams, and this requires closely monitored information of stress level by frequent visual inspection and field measurement.

To find cracks on bridge structures, manual inspection is still the most common method. FHWA has mandated that all highway bridges located on public roads should be inspected every two years. Manual inspection has disadvantages, such as (1) lacking objectiveness, (2) only detecting specific types of damage, and, (3) having high costs. Therefore, subsequent crack monitoring activities are scheduled and conducted separately using crack-detecting sensors by experts.
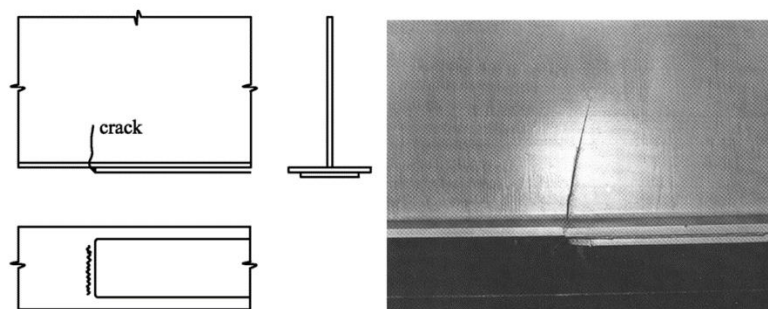
Figure 1.1 Fatigue cracking of cover-plate ends [1].

Extensive research has been performed in crack detecting sensors since the turn of the millennium and many non-destructive evaluation and testing methods have been developed. One common method to detect flaws and cracks in metallic materials is using angle beam ultrasound. The ultrasonic wave can be generated by wireless inductively-coupled piezoelectric transducers. This wave is reflected back to the transducer when it meets a discontinuity in the surface or a crack. Typically, crack inspection with this method requires experience and is manually performed by moving the transducer across the surface at different orientations [5]. Another mature technology is the usage of eddy currents induced by alternating the electromagnetic field to generate magnetic lines of force. This method is very effective in determining subsurface cracks due to its penetration depth [6, 7]. Other technologies that have been patented or are commercially available include ultrasonic flaw detectors [8], giant magneto-resistive sensors [9], surface-mount piezoelectric paint sensors [10, 11], probe-pump-based Brillouin sensor systems [12], coaxial cable sensors [13], and fiber-optic sensors [14]. However, the usage of these methods for long-term monitoring of crack patterns in larger scale civil infrastructure is highly time-consuming and expensive. To address such issues, Kalansuriya *et al.*, [15] introduced the concept of using radio frequency identification (RFID) tag antennas to sense surface cracks and the usage of a grid of RFID tags to monitor crack patterns in civil infrastructure.

RFID technology was introduced in 1999 and research in the area has seen significant growth since 2003 [5]. RFID tags have seen large-scale, highly-integrated deployment for object identification, particularly in the supply chain and apparel industry. The RFID method uses electromagnetic transmission by means of a radio frequency-compatible integrated circuit to

7

retrieve data from tags and send it to readers. A tag is a microprocessor chip that stores the manufacturer name, product type, and environmental factors, which can include temperature, humidity, etc. Tags can be active when powered by batteries or passive when no power source is required to operate them. RFID tags come in a broad range of frequencies to choose from, from the hundreds of kilohertz to microwave gigahertz. The tag's identity is broadcast to the reader, which operates on the same frequency under the same tag protocol. Readers can also write data that is compatible with the tag. Communication between tag and reader can be possible either by a wired or a wireless network communication system [5].

The usage of tag antenna to monitor crack patterns in civil infrastructure is based on the principle that the tip of a defect works as a single turn solenoid coil. This coil concentrates the magnetic flux and produces localized Lorentz forces. The presence of a crack changes the radiation and impedance of the tag antenna permanently [15]. In 2010, Deshmukh and Huang [16] reported that the resonant frequency of a microstrip patch antenna is sensitive to crack presence in the ground plane, so that antenna sensors are sensitive to strain and are capable of detecting cracks in metal structures.

RFID technology has been applied in several methods for crack detection. One involves embedding RFID wireless sensors into carbon fiber-reinforced plastics (CFRP) to detect delamination, which results in frequency oscillations [17]. One significant downfall to this system is that embedding sensors into CRFPs can cause decreases in static and fatigue capacities. Another system is the wireless microelectromechanical (MEMS) ultrasonic sensor. This sensor consists of a rectenna (rectifying antenna) circuit, silicon nitride membranes to generate Lamb waves, interdigital

transducers that serve as ultrasonic receivers, and a wireless circuit for transmission [18]. Further work on these systems is needed to assess the issue of sensitivity to damage.

WSNs and RFID technology are two complimentary technologies that, when combined, can overcome the shortcomings that each system faces by itself [19]. For instance, RFID systems operate as peer-to-peer communication, i.e. single-hop, so they cannot broadcast information reliably at long ranges. This is resolved by using the multi-hop capacity of WSNs, i.e., a series of multiple peer-to-peer communications, ensuring more accurate transmission of data. While RFID allows the detection of objects that are not easily distinguishable using other sensor technologies, it does not provide information on the condition of the objects while WSNs are capable of processing said information. RFID systems are closed systems, but WSNs allow programmability. There are four types of integration of RFID with WSN technologies [19]. These are integrations in which: (1) RFID is used to identify and WSN is used for sensing, (2) both RFID and sensors are used to identify, (3) a WSN is used to provide location and RFID is used to either identify or assist in positioning performed by sensors, and (4) a WSN is used to provide multi-hop communication and RFID is used to identify or track objects. However, establishing true integration between RFID and WSN with reliable data transfer capability and low cost is still far-reaching goal.

CHAPTER 2. LITERATURE REVIEW

A brief literature survey has been conducted to provide more detailed background of crack detection methodologies for steel bridges using traditional and other sensors than RFID-based sensors.

1. Types of Cracks on Steel Bridges

Steel bridges are vulnerable to fatigue induced damage in their parts, and a comprehensive report on fatigue-prone details in 400 European steel bridges was collected by Haghani *et al.* [1]. The key conclusions are summarized in this section.

Fatigue-prone details are typically the portion where general structural analysis cannot predict stress concentration because of construction details. For example, the connections between floor-beams and the main load-carrying members (see Figure 2.1). There is no way to put the stringer right at the end of the floor beam, or to connect the main members to the connection to main truss. To be able to do that, a small gap was created, and it was where the fatigue crack was initiated due to the secondary bending moment in the plan of floor-beam web, and out-of-plane bending. To detect initial cracking, the connection parts must be visually investigated, and putting a strain sensor near the tip of the gap or under the stringer is helpful to monitor excessive stress concentration, which could develop fatigue cracks.
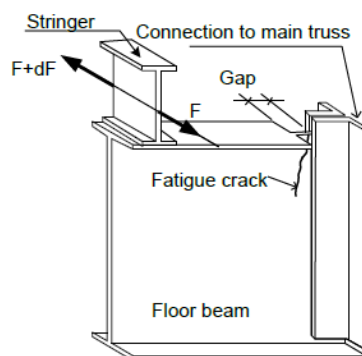

Figure 2.1 Fatigue-prone connection [1].

Other fatigue crack-prone details have similar characteristics, such that the detail attracts stress

concentration, and which develops to fatigue cracks. The examples include: diaphragms and cross-

bracing connections (Figure 2.2a) [1], copied and cut-short beam ends (Figure 2.2b) [1], stringer-to-

floor beam connections (Figure 2.2c) [1], and welded cover plates (Figure 2.2d) [1].
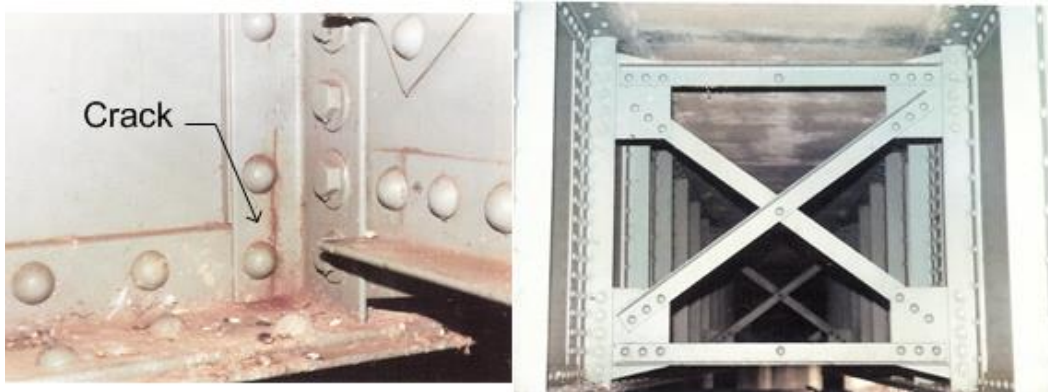
(a) Diaphragms and cross-bracing connections.
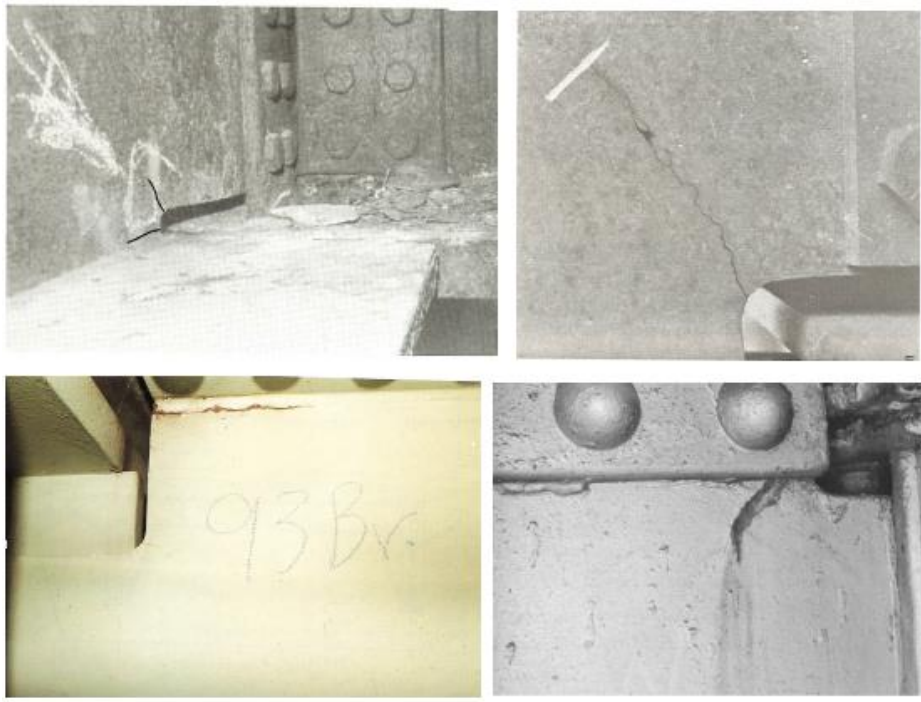
(b) Coped and cut-short beam ends.

FFigure 2.2 Examples of fatigue cracks in steel bridges [1].

(c) Stringer-to-floor beam connections.

7 foot long crack

(d) Welded cover plates.

Figure 2.2 Examples of fatigue cracks in steel bridges [1] (continued).

Steel bridges have intrinsic fatigue-prone details in their design for proper construction, and once the crack is initiated from any reason, that should be detected and controlled; either maintained or closely monitored before it develops to critical stage.

2. Crack Detection Methods and Their Applications

Currently, numerous bridges require testing beyond visual inspection to determine the structural integrity. Destructive Testing (DT) and Non-Destructive Testing (NDT) are two very different ways to obtain the full analysis for in-depth and routine inspection. This section summarizes traditional crack detection methods which are typically used for steel bridges in the field.

a. Traditional Non-Destructive Tests

Visual Inspection: The inspector visually inspects parts of the bridges. As the original form of bridge inspection, it is simple and the most widely used methods. Guidelines for visual inspection were developed for state departments of transportation [20]. Visual inspection is sometimes the only method to check and confirm minor and crack damage; however, it also has limitations such that only exterior damage can be determined; damage in some places where access is difficult is not possible; subjective to individual inspectors, requires multiple years of experience; time consuming and expensive.

Chain Drag/Hammer Tests: A chain or a hammer are moved over the surface of the bridge while the inspector listens for a change in tone or pitch, made by the dragged instrument. These methods are inexpensive and can be done by someone with limited training. If the sounds are different, the inspector marks the area with a circle of spray paint and takes a picture or lays out a grid to map the spots considered suspect. These methods do not go very deep into the member as compared to other methods.

Dye Penetrant Test: The penetrant is applied to the cracked surface, and the excess penetrant is removed and developer is added, rendering the crack visible [21]. This quick, low-cost method can

detect surface cracks that are not visible to the naked eye. This test only applies to non-porous materials such as metallic or ceramic surfaces; therefore, it is not applicable to concrete surfaces.

"D" Meter: A "D" meter shows the thickness of steel sections when one surface is exposed. It uses sound waves to determine the thickness of many materials including re-bars. The meter is pocket sized and can be used on the go.

Half Cell Tests: Corrosion of reinforcing steel is an electro-chemical process, and steel rebar's half-cell potential changes according to the degree of corrosion [22]. The greater the potential, the greater the probability that corrosion is taking place. The half-cell is attached to the reinforcement with a voltmeter in-between, and the potential is then read on the voltmeter. To check the potential, the rebars must be exposed, therefore, it is applicable when some portion of rebar is exposed out of concrete.

Fiber Optic Sensors: Optical fibers sensitive to stress, strain, temperature and other factors, can be used to monitor bridges by directly attaching the fibers on the rebar [23]. To effectively monitor deformation of rebar, it should be installed on the rebar in the construction period, and typically, is costly.

Ultrasonic Tests: Ultrasonic signal is transmitted to the surface of concrete, and the reflected signal is measured to detect flaws or cracks in the bridge [24]. Because of high power consumption, wireless option was not developed; therefore, the tests require an electrical source nearby. Typical patterns need to be pre-determined and used to train inspectors. This method also requires training and long-term experience, and typically costly.

b. Destructive Tests

Destructive tests are not the preferred method to inspect an in-service bridges because it will induce artificial damage on the structures, which is not desirable. Sometimes, destructive tests are required to check the strength in the construction stage, or for other purposes. This section summarizes current destructive methods in the field bridge inspection.

Concrete Strength Test: The standard cylindrical specimen of the concrete is sampled and its compressive strength is tested using the universal loading machine in the lab. Drilling and removing concrete cores from bridge structures put in jeopardy the structural integrity.

Reinforcement Steel Strength Test: A sample of rebar is removed from the concrete, and its compressive and tensile strengths are tested in the lab. Removing rebar from concrete is not easy, and the coring of rebar and concrete also induces damage on the bridge.

Moisture Content Test: The concrete's moisture contents can be measured before it has hardened using an electrical impedance meter. The moisture contents can be measured after hardening if sensors are embedded into the concrete. If no sensors are embedded, the final moisture contents cannot be measured.

Carbonation: Carbon dioxide from air can react with the calcium hydroxide in concrete to form calcium carbonate, which is called carbonation [25]. Carbonation of concrete is a slow and continuous progress from the outer surface inward, yet slows down with increased diffusion depth. This process exposes the reinforcement to be able to be inspected. This process can expose the rebar, making it vulnerable to the environment and also decreases the alkalinity of the concrete, which is essential to the corrosion resistance of the reinforcement steel.

These are selective methods that are used to inspect bridges in the field. Non-destructive tests are much preferred than destructive tests in the field to prevent damage to the bridges. Visual inspection is the most favored and wide-spread methods; however, it has limitations. The methods using advanced sensors, such as ultrasound or fiber optic sensors, can provide accurate measures of damage; however, they are costly, and need experience and training. Quick and inexpensive methods, such as "D" meter or chain drag/hammer tests, could give more information than visual inspection; however, it also has limitation on damage sensitivity. The quick and inexpensive crack/damage detection methods with reasonable damage measures are desirable.

c. Crack Detection in Metallic Materials

A few methods to detect cracks in metallic materials have been developed. One of the most common and effective methods to detect flaws and cracks is using angle beam ultrasound [5]. The ultrasonic wave can be generated by wireless inductively-coupled piezoelectric transducers. This wave is reflected back to the transducer by some form of discontinuity, such as another surface or a crack. Typically, crack inspection with this method requires an experienced operator and it is manually performed by moving the transducer across the surface at different orientations. Another mature technology is the usage of eddy currents where the alternation of the electromagnetic field generates magnetic lines of force that reveal hidden defects. This method is very effective in determining subsurface cracks due to its great penetration depth [6,7]. Other technologies that have been patented, or are commercially available, include ultrasonic flaw detectors [8], magnetorestive sensors [9], surface-mount piezoelectric paint sensors [10, 11], probe-pump-based Brillouin sensor systems [12], coaxial cable sensors [13], and fiber-optic sensors [14], among others. However, the

16

use of these methods for long-term monitoring of crack patterns in larger scale civil infrastructure is

time-consuming and expensive.

CHAPTER 3. BACKGROUND

This chapter provides a comprehensive, theoretical development of the mechanism of RFID antenna-based sensors for crack monitoring of metal surfaces, and basic components of RFID-based sensing. The backscatter power as a damage index will be introduced; the substrate material to measure the power on the metal surfaces will be investigated; and, the components of the RFID-based sensing is summarized.

1. Backscatter Power

Kalansuriya, *et al.* **Error! Reference source not found.** identify backscatter power as the most mportant measured value from a tag for crack detection and characterization. Backscatter power can be described by the radar range equation:

$$P_R = P_T \frac{G_T G_R}{4\pi} \left(\frac{\lambda}{4\pi R_T R_R}\right)^2 \sigma \qquad (3.1)$$

where P_R is the backscatter power, P_T is the transmitted power, G_T is the transmitting antenna gain, G_R is the receiving antenna gain, λ is the signal wavelength, R_T is the distance between the target (the tag chip, in this application) and the transmitting antenna, R_R is the distance between the target and the receiving antenna, and σ is the target's radar cross section. In a monostatic scattering application, the antenna emitting the electromagnetic signal also receives the echo from the target tag chip so that $R_R = R_T$ and $G_R = G_T$.

Equation 3.1 shows that backscatter power is attenuated as the reading distance increases by a quartic factor. P_R can be determined from the received signal strength indicator (RSSI) logged by the reader equipment from the following expression:

$$RSSI = 10 \log_{10} \left(\frac{P_R}{1 \, mW}\right) \qquad (3.2)$$

RSSI is then a decibel expression (dBm) of backscatter power.

Most reading equipment uses frequency hopping spread spectrum (FHSS), so the value of RSSI depends on the transmit frequency channel. The signal frequency varies in the range of 902-928 MHz in North America. The Impnj Speedway MultiReader software used in this study performs a frequency hopping sequence by changing the transmitting channel during each inventory session. Table 3.1 shows the signal frequency assigned to each channel. This study uses average values of RSSI of data samples equally weighted across all frequency channels.

Table 3.1 Impnj Speedway reader frequency plan for North America.

Channel number	1	2	3	4	…	49	50
Center Frequency (MHz)	902.75	903.25	903.75	904.25	…	926.75	927.25

2. Substrate Material: Image Theory Behind RFID Wave Propagation

The usage of RFID technology for crack detection on metallic surfaces adds a layer of complexity to the received backscatter power signal related to image theory. A steel plate is a large conductive surface that behaves as a ground plane. The backscatter power signal received at the antenna is equal to:

$$\exp(-j\beta_{air}z)\left(I_{tag} + I_{ground}\exp(-j\beta_{material}\Delta z)\right) \tag{3.3}$$

where, β_{air} is the phase constant of air, $\beta_{material}$ is the phase constant of the substrate material (a material separating the tag from the metallic surface), I_{tag} is the primary backscatter of the tag, and I_{ground} is the image backscatter. For a horizontal tag (i.e., a tag oriented parallel to the ground

plane), $I_{tag} = -I_{ground}$. If a horizontal metallic RFID tag is placed directly on the metallic surface

acting as a ground plane ($\Delta z = 0$), the power signal received at the antenna will be zero.

The magnitude of the reflected wave can be maximized when the reflection of the RFID tag

comes from an image source located half a wavelength below (see Figure 3.1) since a half

wavelength corresponds to a 180º phase change. In practical terms, this means that, ideally, the

RFID tag should be placed at a quarter wavelength in front of the metallic surface in order to

maximize the power received by the antenna.
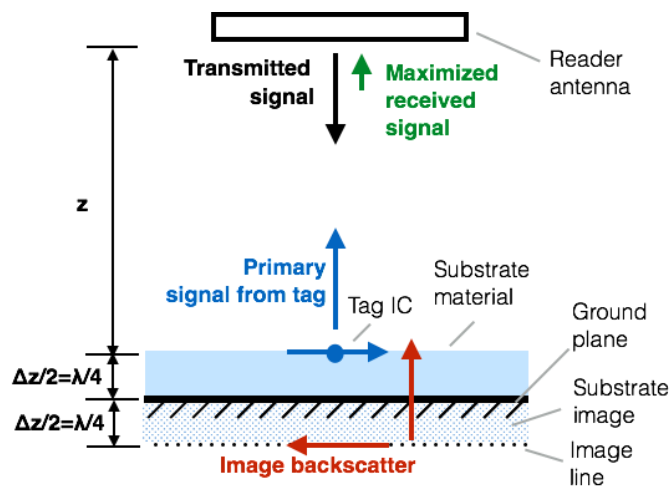
Figure 3.1 Effect of a ground plane on the reflected signal from an RFID tag.

The antenna used in this investigation is a right-hand circularly-polarized antenna that transmits

signals at frequencies ranging from 902-928 MHz. Since the wavelength of these signals is

approximately 1 ft, a substrate material closely resembling the relative permittivity of air (such as

polystyrene foam) should ideally be 3 in thick. However, such a thick substrate would raise

concerns on the structural effect that it would sustain on the girder. If the material selected to

separate the tag from the metallic surface has the adequate dielectric properties, it can be used to

reduce the physical separation between the tag and the ground plane. The wavelength of an electromagnetic wave in a dielectric medium is given as:

$$\lambda = \frac{c}{f} * \frac{1}{\sqrt{\epsilon_r}} \qquad (3.4)$$

where, f is the wave frequency, c is the speed of light, and ϵ_r is the relative permittivity of the material between the target tag and the ground plane. In vacuum conditions, $\epsilon_r = 1$. The relative permittivity of air is approximately 1. Relative permittivity can be related to the phase constant by:

$$\epsilon_r = \left(\frac{\beta c}{2\pi f}\right)^2 \qquad (3.5)$$

According to equation 3.4, a material with higher permittivity also reduces the wavelength in a dielectric medium, thus reducing the required distance Δz to maximize the received backscatter power. Therefore, a thinner substrate made of a material with a relative permittivity greater than one is preferred to increase the received backscatter power signal. This substrate must also be sufficiently elastic in order to transfer the strains at the extreme tension fiber of the girder into the RFID tag and it should also be able to adhere to a metallic surface with weatherproof adhesive. From the available materials that fulfill all of these characteristics, ethyl-vinyl acetate (EVA) rubber, which has a relative permittivity of approximately 2.8, has been found to increase RSSI satisfactorily while also being a very flexible and durable material.

3. Schematics of RFID Sensing

The basic setup of an RFID sensing system consists of a reader, a reader antenna and a tag (see Figure 3.2). The RFID reader communicates directly with a computer to determine the signal sent and collect the response from the sensing system. The reader antenna must be connected to the reader in order to send the transmitted power signal. The RFID tag receives this power signal.
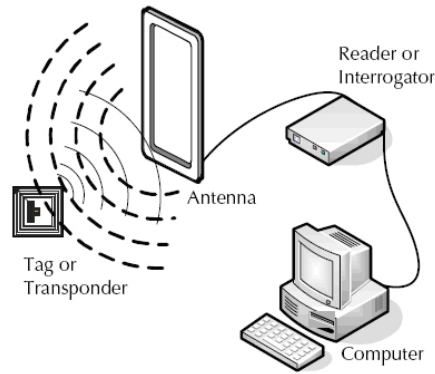
Figure 3.2 RFID sensing system [26].

The RFID tag consists of three main parts: an integrated circuit (IC), an antenna, and an inlay. The IC contains all the identification information of that particular tag. This allows a distinction between one tag and another when reading an array of tags in order to identify the exact location of that tag. The available memory in an IC may vary between 96 bits and 8KB and it may be protected by an access password if sensitive information is stored.

The tag antenna can be made of aluminum, copper or silver. For an ultra-high frequency (UHF) RFID application (that is, systems with frequency ranges between 860-960MHz), the reading distance between reader antenna and tag antenna can be rather large. The size of a tag antenna is directly proportional to the reading distance as well. This allows a reduction in antenna size for UHF RFID systems, reducing costs significantly. Tag antennas are susceptible to several environmental factors, such as metal, temperature and water. These effects are of particular interest to our application since all three factors will be present on bridge cover-plate deployment.

The tag encasement can be classified into three different kinds: inlay, label or hard encasement. The inlay contains the IC and tag antenna bonded to a polyethylene terephthalate (PET) layer. The layer may be dry or wet, indicating the absence or presence of a pressure-sensitive liner, respectively. For retail identification purposes, this only is oftentimes covered by a paper or

22

synthetic label with either a barcode or some other information. Hard encasements provide resistance to impact, water, temperature and distortions to power signal caused by metallic materials. Hard encasements can be attached to objects with adhesives such as epoxy or other parts such as screws or bolts. These encasements will be further investigated and evaluated to determine the proper encasement for our application.

CHAPTER 4. DEVELOPMENT OF RFID CRACK SENSORS

In this chapter, the development of RFID crack sensors are provided. All development procedure have been validated with appropriate experiments, which are also accompanied.

1.   Single RFID-Based Crack Sensor Development

The components of a single crack detection sensor include a commercial RFID tag, a layer of a substrate material, and adhesives (see Figure 4.1). Multiple adhesives including epoxy, double-sided tape, and a cyanoacrylate-based glue were used to test their effect on RSSI and no significant difference was found. Epoxy was finally chosen as an adhesive for bonding for both interfaces in field deployment because of its proven effectiveness in the strain transferring applications, such as with optical fiber sensors.
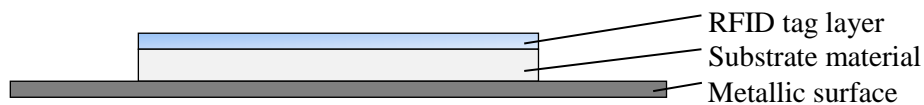
Figure 4.1 Single sensor configuration of RFID crack sensor.

The commercial UHF RFID tag used in this paper is the Alien Technology ALN-9662 Short Inlay tag (see Figure 4.2). This tag is EPG Gen 2 and ISO/IEC 18000-6C compliant and it uses a Higgs 3 EPC Class 1 Gen 2 RFID tag integrated circuit (IC). The tag antenna is made of a flexible metallic material, which is adhered to a wet inlay.

Figure 4.2 Example commercial RFID tags: ALN-9662 short inlay.

The substrates used in this paper are EVA rubber or polystyrene foam. Polystyrene foam is used for experiments where a material with relative permittivity similar to that of air is desired for basic

evaluations of backscatter power behavior. Since EVA rubber has a higher relative permittivity and is flexible and durable, it is used in experiments for sensing system performance evaluation where higher RSSI readings are desired.

2. Experimental Set-up

The purchase of RFID equipment is justified by the need of performing experimental validations on the RFID tag that will eventually be designed for crack detection in bridge cover plates. The Impnj Speedway Revolution R420 reader has ports to support readings from up to 4 reader antennas. This reader can deliver a transmit power of up to 32.5 dBm and can read a reflected power as low as -90 dBm. The accompanying software, Impinj MultiReader Software version 6.6.13, provides the controlling interface from the computer that is connected to the reader via Ethernet. MultiReader provides vital information for our application such as transmitted power, RSSI, time stamps, measurement frequency, and tag identification. The reader antenna is a standard Impnj circular polarized far field antenna with right hand polarization. The frequency range is in compliance with RFID in the United States (902-928 MHz). It has a gain of 9 dBic and a nominal impedance of 50 Ohms. Figure 4.3 shows the complete laboratory setup with a laptop computer with Impinj MultiReader Software, the MultiReader, and the reader antenna.
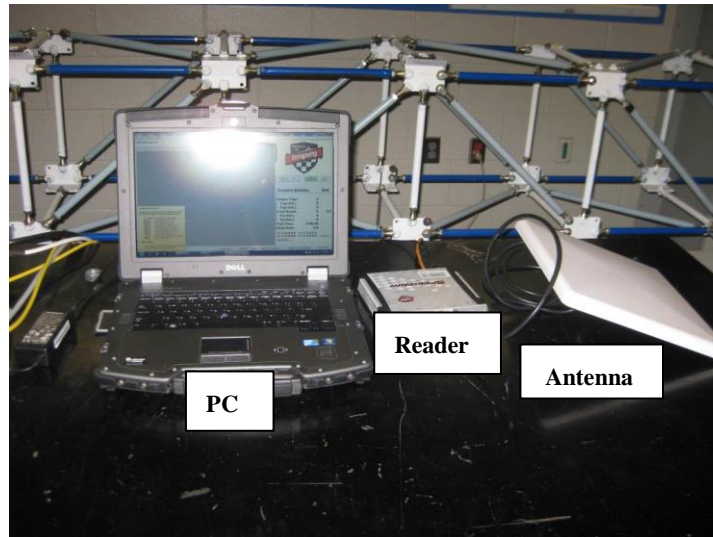
Figure 4.3 Laboratory set-up.

The Impnj Speedway MultiReader software has been used along with its accompanying reader. A circular right hand polarized far field antenna with a frequency range of 902-928 MHz (North America) and a gain of 9 dBic (3.98-in magnitude relative to an ideal isotropic antenna) is used.

In order to avoid unknown reflection or absorption of different materials, the experiments have been carried out outdoors such that obstructions that could interfere with the transmitted signal were kept out of the range of the reader antenna. The vertical and horizontal beam widths are 60º. However, since the angle for maximum range of the reader antenna is 0º on the vertical and horizontal planes (see Figure 4.4), the tag in question was set directly in front of the reader antenna.

(a) (b)
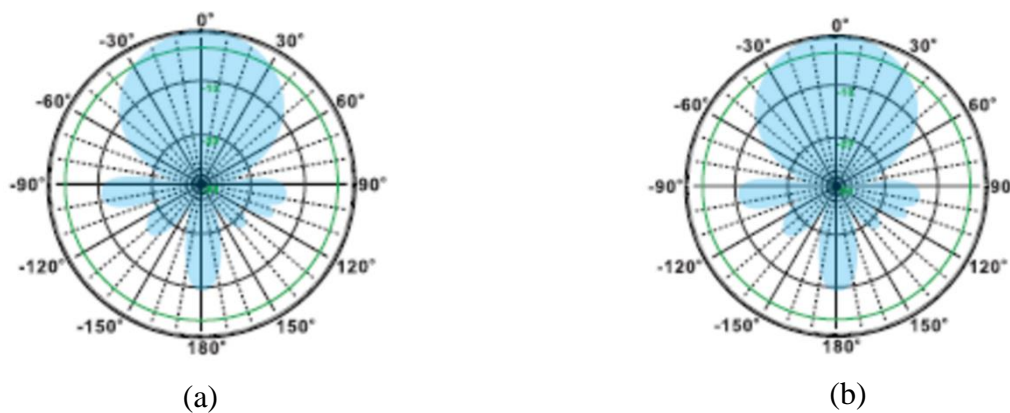
Figure 4.4 Reader antenna radiation pattern: (a) azimuth plane; (b) elevation plane.

The centers of the antenna and the tag were kept at an equal and constant distance from the ground. In circular polarized antennas, the preferred tag orientations are as shown in Figure 4.5. These orientations ensure that the reader antenna receives the maximum backscatter power. Orientation B was chosen for the laboratory experiments.
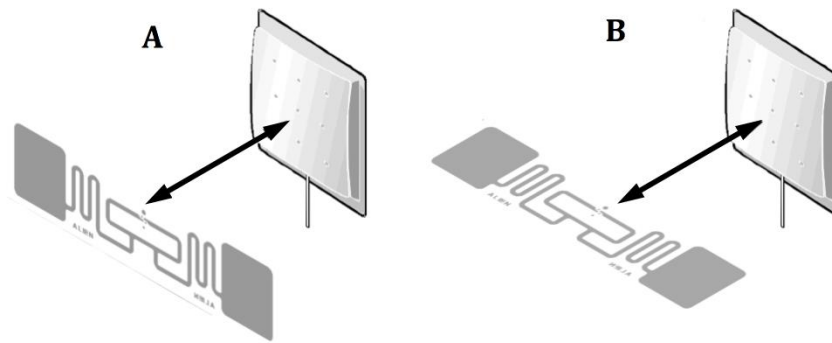
Figure 4.5 Preferred tag orientations.

3. Test 1: Read Distance

The greater read distances cause backscatter power from the tag in question to be reduced by a quartic factor. The effects of read distance on RSSI along with the effect of severing a portion of the tag antenna have been studied. RSSI was measured for read distances at 3-foot intervals up to 15 ft, as shown in Figure 4.6. The RFID tag was attached to a polystyrene foam block. Polystyrene foam is known to have low reflective and absorptive properties, closely simulating air.
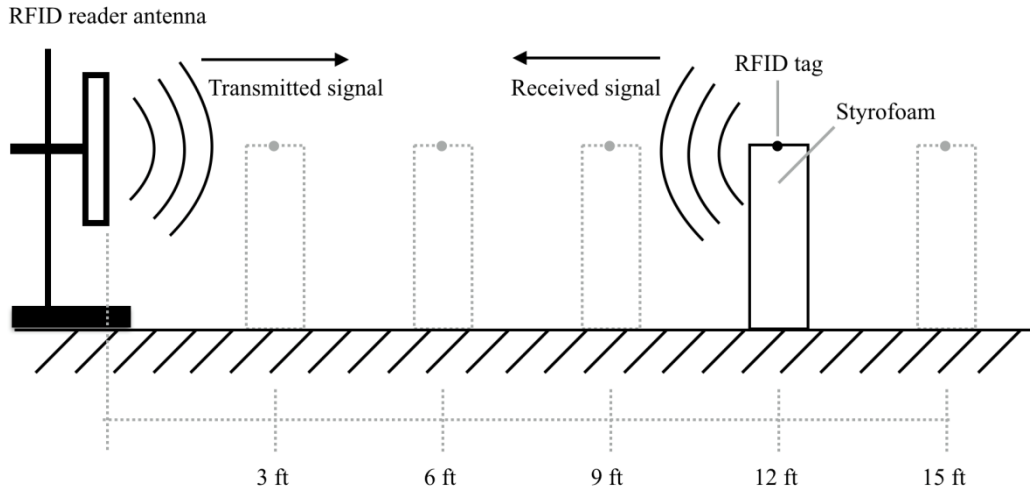
Figure 4.6 Elevation of experimental setup.

The subsequent measurements of RSSI were made for tags that were severed at different locations, simulating different scenarios of an underlying crack that has propagated into the antenna. The two cutting sequences shown in Figure 4.7 were examined. Each cut number represents a different location in which a crack disconnects an additional portion of the antenna from the IC. For example, Damage Scenario #2 in Sequence #1 represents the situation in which a crack along the dotted line #1 and another crack along the dotted line #2 disconnected the portions to the right of the dotted line #1 and to the left of the dotted line #2. Scenario #3 represents two cracks that disconnected the portions to the right of dotted line #3 and to the left of dotted line #2. The RSSI at each stage in the cutting sequence was measured at the distances shown in Figure 4.6.
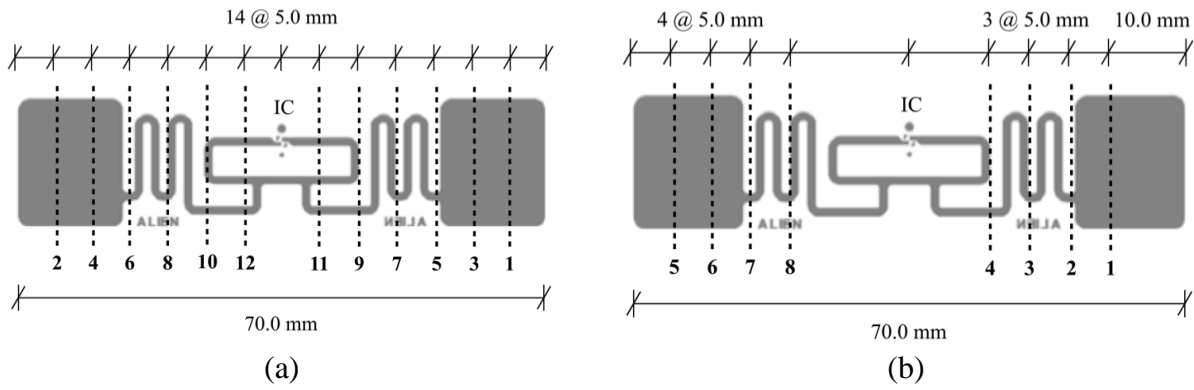
Figure 4.7 Cutting sequences of RFID tags: (a) sequence #1, (b) sequence #2.

The trends of RSSI versus damage scenario and read distance for both sequences are shown in Figure 4.8. As greater areas of the tag antenna were disconnected from the tag IC, RSSI exponentially decayed. Cuts made between the IC and the square patches do not yield as great a gradient in RSSI as cuts made within the square patches. When greater antenna surface area was disconnected from the IC loop, a larger drop in RSSI was detected. Therefore, damage within the tag can be more precisely located when the damage is within the square patch than when the damage is between the patch and the IC.

The reader was incapable of detecting the tag backscatter power at further distances. The dependence of RSSI on read distance establishes a requirement for read distance standardization. Since RSSI decreases with distance, the chosen parameter for crack detection will depend on the final choice of read distance.

Finally, it was noted that RFID tags could not reflect power when receiving direct sunlight. This limits the usage of RFID tags for crack detection to shaded areas. As the bridge deck covers bridge girders throughout most of the day, it is anticipated that proper scheduling will suffice for proper damage identification in the field.
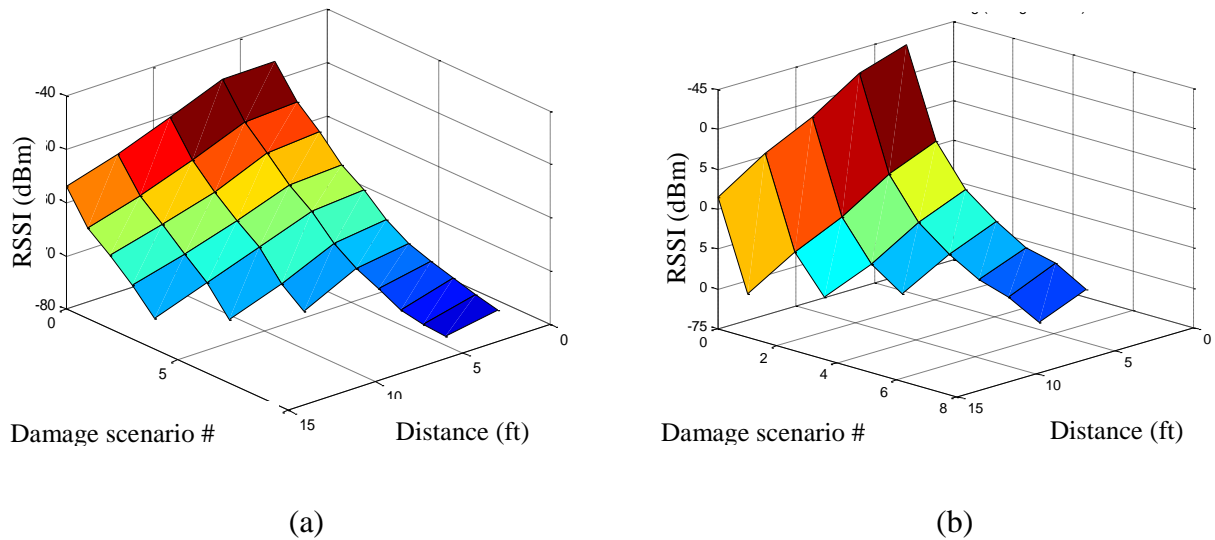
Figure 4.8 RSSI vs. Damage Scenario and read distance: (a) sequence #1, (b) sequence #2.

4. Test 2: Crack Detection Experiment

A second set of tests was conducted to demonstrate the crack propagation detection capability of commercial RFID tags on a metallic surface. Figure 4.9 shows the overall arrangement for these experiments. A PC with Impnj MultiReader software was connected to an Impnj Speedway Revolution R420 UHF RFID Reader. A high gain circular right hand polarized patch antenna was connected to the reader. A 1/8-in thick rectangular aluminum plate was used as a test specimen. A 1-in long incision was made into one side with a 1/16-in vertical band saw blade. The opposing side was left unaltered as a control surface.

As expected, no radiation was detected from the tag when it was directly attached to the metallic surface. A polystyrene foam plate was used as a substrate material to simulate air as closely as possible. In a similar setup, an EVA foam plate was also used as a substrate material for comparison. The aluminum plate, polystyrene foam or EVA foam plate, and the ALN-9662 RFID tag were raised onto a stack of polystyrene foam so that the tag IC would be elevated to the same

height as the center of the reader antenna while avoiding excessive radiation interference. The read distance was fixed at 3 ft.

Four damage scenarios were tested for detection: (1) undamaged surface with uncut tag, (2) cracked surface with uncut tag, (3) cracked surface and cracked substrate material with uncut tag, and (4) cracked surface with cut tag (see Table 4.1). Each scenario represents a stage in crack formation and propagation, the first being no damage at all and the last being the ultimate damage case. Damage stage #2 shows the initial stage of crack formation on the metallic surface while both the tag and the substrate material is untouched. Damage stage #3 represents the case when a crack is formed on the metallic surface and the substrate material, but the tag itself is undamaged. The inclusion of damage stage #3 is only tested for EVA foam to check the influence of a higher permittivity than the Styrofoam for crack propagation. Since polystyrene foam has a permittivity close to that of air, Damage stage #3 was not included. Figure 4.10 shows the tag placement on the substrate materials and the metallic surface.
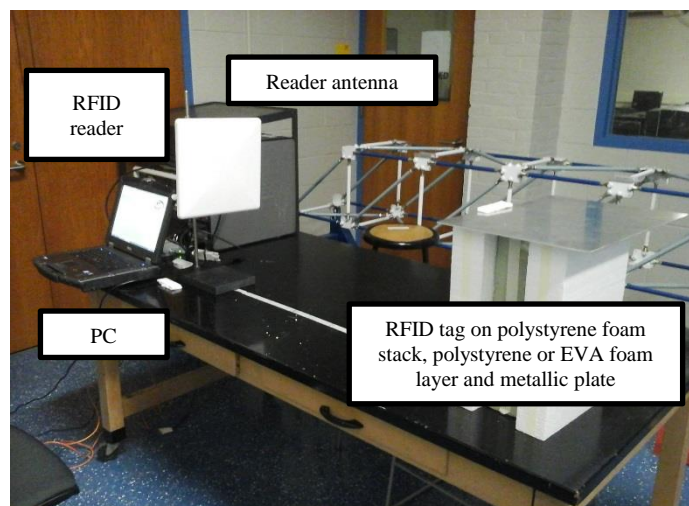
Figure 4.9 Setup for crack detection tests.

Table 4.1. Conditions in each damage scenario.

Damage scenario	Sensing component		Metallic surface
	Tag	Substrate	
1	Intact	Intact	Intact
2	Intact	Intact	Crack damage
3	Intact	Crack damage	Crack damage
4	Crack damage	Crack damage	Crack damage

(a)   (b)
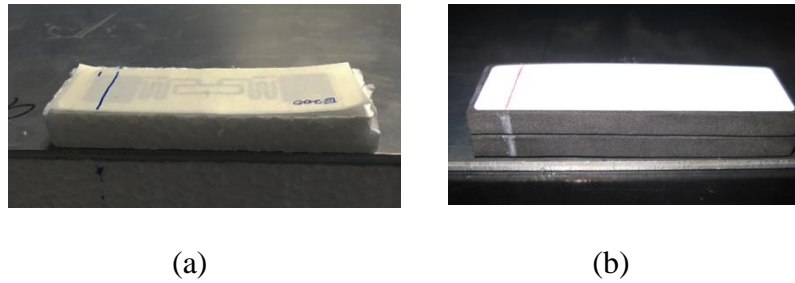
Figure 4.10 Front view of aluminum plate, foam plate, and RFID tag: (a) 0.4290-in thick polystyrene foam, (b) 0.5-in thick EVA foam.

Figure 4.11 shows the resulting measurements of RSSI for all damage scenarios using intermediate polystyrene foam and EVA foam. The overall performance of the tag was improved (i.e., RSSI was increased) when EVA foam used, as raw RSSI ranged between -52.87 and -40.46 dBm compared to the range of -56.03 and -45.38 dBm when polystyrene foam was used. As a crack formed on the metallic surface and propagated up to the substrate, RSSI consistently increased regardless of the substrate material. A drop in RSSI occurred upon the cracking of the tag antenna (Damage Scenario #4) compared to the control (Damage Scenario #1) when either EVA or polystyrene foams were used. It is clear then that the underlying metallic surface increases the

radiation efficiency of the system when a crack is present on the left side of the tag IC with respect to the direction of the incident electromagnetic wave. It is, therefore, possible to detect an underlying crack that has not propagated into the RFID sensor and that has opened a gap across the depth of the metallic surface.
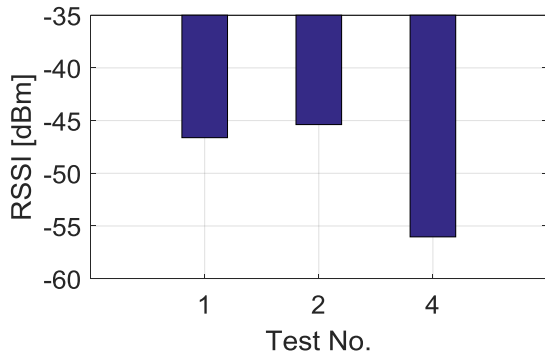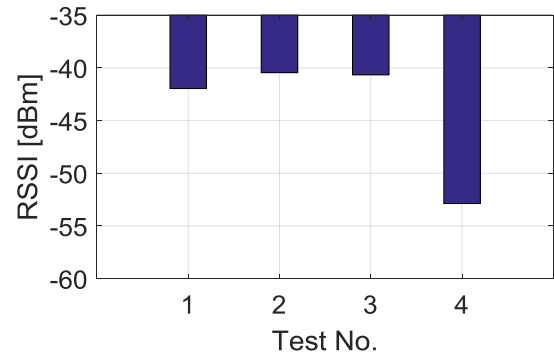
(a)　　　　　　　　　　　　　　　　　　(b)

Figure 4.11 RSSI for crack detection experiments: (a) 0.4290-in thick polystyrene foam, (b) 0.5-in thick EVA foam.

5. 2D Array Sensor Development

a. Multiple Sensor Array Configurations

To increase the pervasiveness of the crack propagation monitoring system, 2D arrays of tags were considered. It is known that the proximity of RFID tags has an effect in their sensitivity, causing some tags to report a gain or a reduction in backscatter power depending on the layout of the surrounding tags. This change in sensitivity is caused by tag detuning, tag shadowing, and re-radiation cancelation, collectively known as coupling, or proximity effects [27].

A 2D array of tags should behave in a way analogous to the parasitic elements in a Yagi-Uda antenna [28]. The principal tag of interest in an array (hereafter referred to as the control tag) would be the driven element. The RSSI of this tag will be the principal indicator of crack formation and propagation. The strength of the RSSI of the control tag will be influenced by the surrounding tags in the array, similar to how director parasitic elements work together in the Yagi-Uda antenna to increase the antenna's gain. Therefore, a 2D array must be selected such to improve pervasiveness with close spacing and to enhance sensitivity to damage with placements that increase RSSI in the control tag. Different tag array configurations were studied based on their effects on the RSSI of a control tag. There are two features that are primarily pertinent to the development of the tag array to be used in this sensing system: spacing between tags and configuration.

b. Test 1: Spacing Between Tags in 2D Arrangement

Coupling effects between tags can either increase or decrease the backscatter power of the tags involved. In order to optimize the backscatter power of a control tag (T-1), the configurations

shown in Table 4.2 were tested for the following separations: 1/8, 1/4, 1/2, 1, and 2 in. Distance 1-2 refers to the separation between tags T-1 and T-2 and distance 1-3 refers to the separation between tags T-1 and T-3. Tag separation was measured as a clear distance from the edge of a patch of one tag to the nearest edge of the patch of the other tag. Figure 4.12 shows the setup used for all tag array experiments. The substrate material used in this experiment to separate the array from the 1/8-inthick aluminum plate was polystyrene foam, and the read distance was kept constant at 3 ft, in reference to the control tag, T-1.

Table 4.2. RFID tag configurations used for spacing optimization.

	C1	C2	C3	C4A
Configuration	T-1	T-1　　T-2	T-1 T-3	T-1　　T-2 T-3
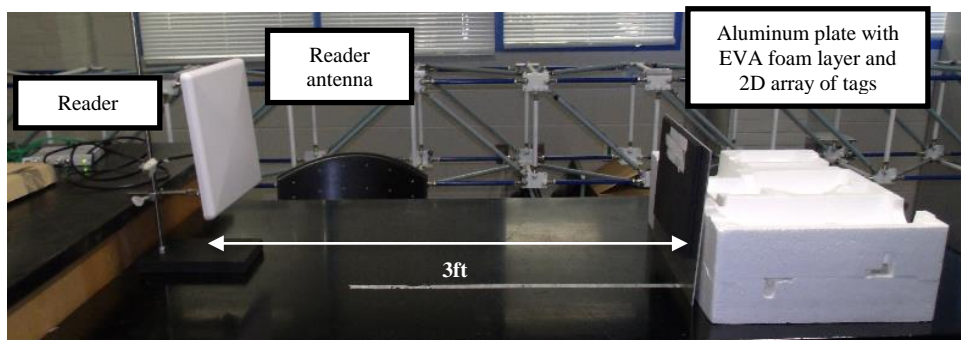
Figure 4.12 Experimental setup for 2D array tag experiments.

Figures 4.13 and 4.14 show the variation in RSSI on tag T-1 for different separations. The blue filled-in circle indicates the original received power of T-1 in standalone configuration (C1). Figure 4.15 shows the values of RSSI for all spacing combinations in configuration C4A. The spacing in horizontal configuration (C2) improved RSSI the most in tag T-1 at 1/4-in separation. The spacing in vertical configuration (C3) improved RSSI the most in tag T-1 at 1/8-in separation. Figure 4.15 shows that the same spacing increases RSSI the most. Therefore, the spacing combination that best

increases RSSI is 1/4 in for horizontal spacing and 1/8 in for vertical spacing. This spacing will be used in all experimentation involving 2D arrays.
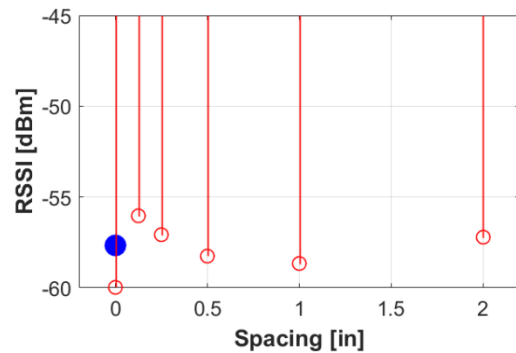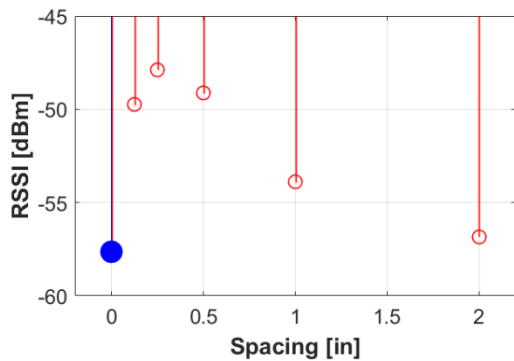
Figure 4.13 RSSI of T-1 in configuration C2.   Figure 4.14 RSSI of T-1 in configuration C3.
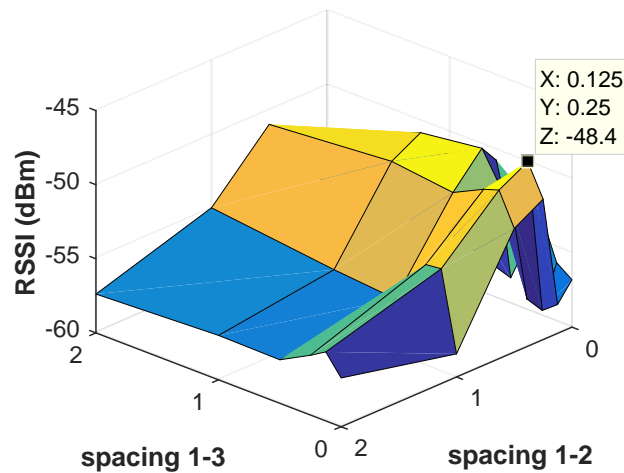
Figure 4.15 RSSI of T-1 in configuration C4A.

c. Test 2: Array Placement

The position of a tag in relation to others can also have a significant impact on its backscatter power. Since crack propagation monitoring requires an increased number of sensing units for greater pervasiveness, a basic array of three rows by two columns of RFID tags was chosen to determine the best configuration for increased received power. Using polystyrene foam as the substrate material, the configurations shown in Table 4.3 were tested for RSSI in the control tag, T-

36

1. The array was placed on a 1/8-in thick aluminum plate. These configurations have been ordered from the one yielding the lowest RSSI in T-1 to the one yielding the highest RSSI in T-1. Figure 4.16 shows a bar graph of the ordered configurations.

Table 4.3. 2D array configurations sorted by RSSI on T-1.
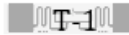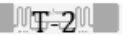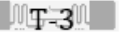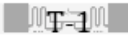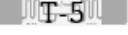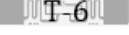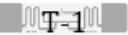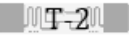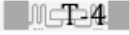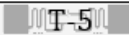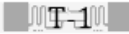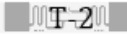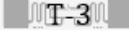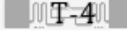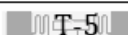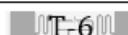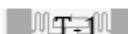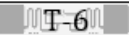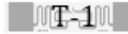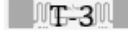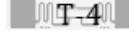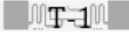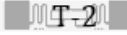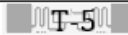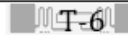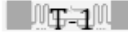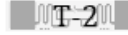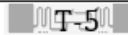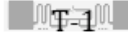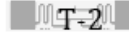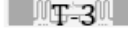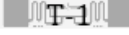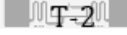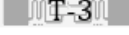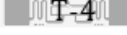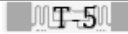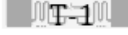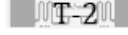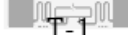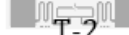
	C3	C6B		C1	C7D	
Configuration	T-1 T-3	T-5 T-1 T-3	T-2	T-1	T-5 T-1	T-6 T-2 T-4
RSSI (dBm)	-46.47	-45.44		-43.41	-41.34	

	C7B		C7C		C7A	
Configuration	T-5 T-1 T-3	T-2 T-4	T-5 T-1 T-3	T-6 T-2	T-6 T-1 T-3	T-2 T-4
RSSI (dBm)	-40.80		-40.77		-40.69	

	C4D		C5B		C8	
Configuration	T-6 T-1	T-2	T-5 T-1	T-6 T-2	T-5 T-1 T-3	T-6 T-2 T-4
RSSI (dBm)	-38.50		-38.32		-37.30	

	C5A		C4C		C4B	
Configuration	T-1 T-3	T-2 T-4	T-5 T-1	T-2	T-1	T-2 T-4
RSSI (dBm)	-37.22		-36.17		-35.98	

37

Table 4.3. 2D array configurations sorted by RSSI on T-1. (continued)

Configuration	C6A		C4A		C2	
	T-6					
	T-1	T-2	T-1	T-2	T-1	T-2
	T-4		T-3			
RSSI (dBm)	-35.33		-35.01		-33.83	

Figure 4.16 2D array configurations sorted by RSSI on T-1.

The configuration that most reduced backscatter power was a vertical array (C3) and the configuration that most increased backscatter power was a purely horizontal one (C2). The RSSI of T-1 was generally improved (in reference to itself in standalone configuration – C1) when there was at least one other tag somewhere on the column next to it. This implies that the array should include tags side by side to the control tag. This also suggests that a combination of configurations C4A, C4B, C4C, C5A, C5B, and C2 will be best to maintain a high RSSI while increasing pervasiveness.

To maintain consistency and cover as much surface area as possible, configurations C5A and C5B, i.e., a 2 by 2 configuration with 4 tags, were preferred for the performance evaluation of the array.

d. Test 3: Performance Evaluation Experiment: 2D Array

Using the same setup as in previous 2D array experiments (see Figure 4.12), a 2D array placed on a 0.5-in thick EVA foam sheet conforming to configuration C5A was used to verify the sensitivity of the system. The same four damage scenarios explained in Table 4.1 were examined: (1) undamaged surface with uncut tag; (2) cracked surface with uncut tag; (3) cracked surface and substrate with uncut tag; and, (4) cracked surface, substrate, and tag. Figure 4.17 shows the final damage stage (Damage Scenario #4). The crack made to the aluminum plate was a 1-in long incision into one side with a 1/16-in vertical band saw blade. The average RSSI of the control tag (upper left tag in the array) was used to compare changes in backscatter power at each damage stage.
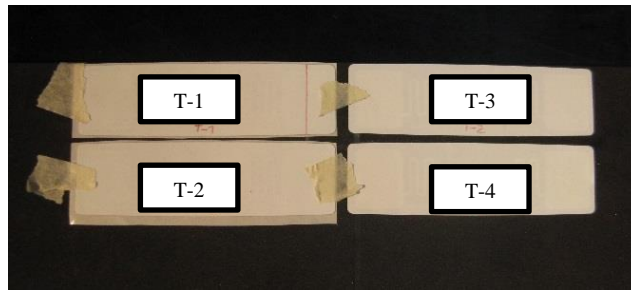
(a)
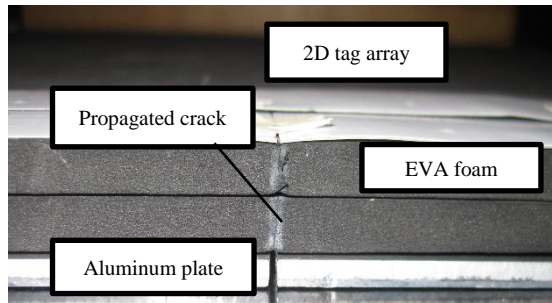
(b)

Figure 4.17 2D Damage stage #4 of 2D array: (a) front view, (b) top view.

The pattern of RSSI changes in the control tag as a crack propagated into the system is shown in Figure 4.18. The selection of the 2D array configuration C5A laid on EVA foam and oriented perpendicular to the reader antenna showed an improvement in performance, yielding RSSI values ranging between -42.91 and -39.25 dBm. In this 2D array, damage to the metallic surface underneath the right side of the control tag IC caused a small drop in RSSI. Further damage in the substrate decreased RSSI slightly more. Finally, the ultimate damage state (Damage Scenario #4) increased RSSI significantly, providing a notable change to indicate damage propagation onto the tag antenna. This trend is mirrored to the pattern observed in the single tag system because the location of the crack in the 2D array performance evaluation experiment was on the right side of the IC with respect to the incident electromagnetic wave instead of on the left side of the IC as was the case in the single tag performance evaluation experiment. This behavior has been observed in in-

house developments of linearly-polarized RFID-based crack sensors where the direction of the

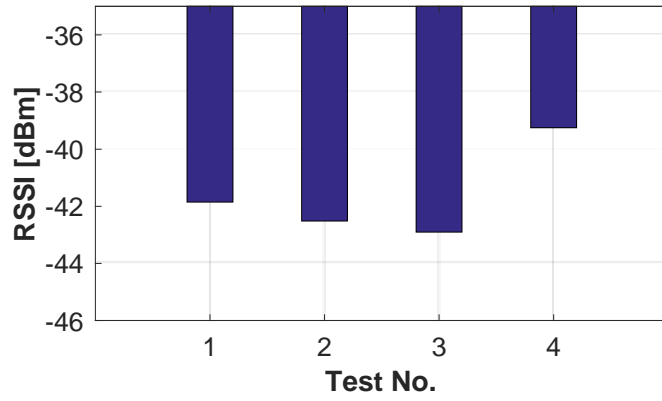change in backscatter power depends on the location of the crack with respect to the IC [15].

Figure 4.18 RSSI of control tag in a 2D array for damage scenarios 1- 4.

6. Damage Index for Crack Localization

Performance evaluation studies have revealed that raw RSSI varies from one commercial RFID tag to another when all other experimental parameters remain unaltered. For further automation of crack detection in bridges, establishing a damage index based on the change of RSSI instead of on raw RSSI values is desirable. Because the change in RSSI is proportional to the severity of crack propagation, percentage change in RSSI before and after crack damage can be used effectively as a measure of damage.

The RSSI percentage change is defined such that:

$$\Delta \text{RSSI} \ (\%) = \left(\frac{RSSI_{intact} - RSSI_{damaged}}{RSSI_{intact}} \right) \times 100 \qquad (4.1)$$

where $RSSI_{intact}$ is the RSSI of the unaltered state and $RSSI_{damaged}$ is the RSSI of the damage stage in question.

The algebraic sign of the percentage change is an indicator of the location of the crack formation with respect to the tag IC. Figure 4.19 shows the location of the crack formation with respect to the tag IC viewed from the angle of the incident electromagnetic wave in all performance evaluation experiments. In single-tag configuration experiments (Figures 4.19a and 4.19b), the crack was to the left of the IC while in the 2D tag array experiment (Figure 4.19c), the crack was to the right of the IC. Figures 4.20 and 4.21 show the percentage changes in RSSI for the single tag configuration and the 2D array configuration, respectively.
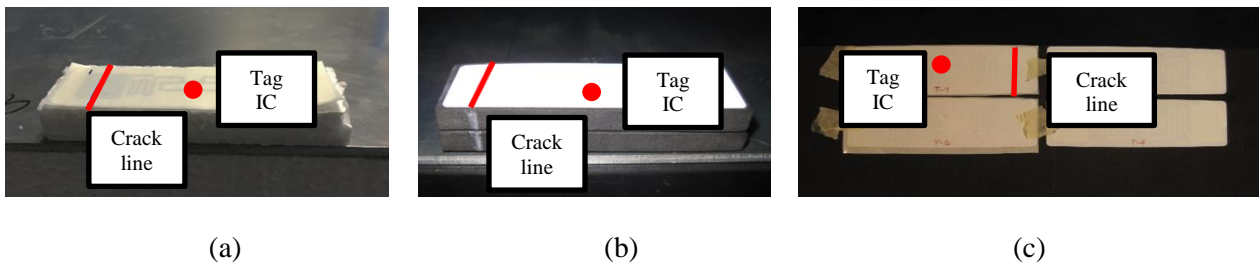
Figure 4.19 Location of crack formation as viewed from the reader antenna: (a) single tag on polystyrene foam, (b) single tag on EVA foam, (c) 2D tag array on EVA foam.

Damage occurring to the left of the tag IC presented small increases in RSSI during initial damage stages. When damage was to the right of the tag IC, small decreases in RSSI were observed during initial damage stages. In the single-tag performance evaluation experiment involving EVA, initial damage stages (Scenarios #2 and #3) induced percentage changes in RSSI ranging from 3.097-3.586%. The same damage stages yielded an RSSI percentage change of 2.665% on a single-tag configuration on polystyrene foam and a range of 1.586-2.52% on the control tag of a 2D array on EVA foam. Therefore, initial stages of damage can be detected when changes in RSSI are between 1.5% and 3.6%.

Furthermore, damage on the left of the tag IC yielded large drops in RSSI at the ultimate damage state (Scenario #4) while ultimate damage on the right of the tag IC exhibited the opposite behavior. Ultimate damage on a single-tag configuration on EVA foam presented an RSSI percentage change of 26.00%. The same configuration and damage state on polystyrene foam yielded a change of 20.19%. Ultimate damage on the control tag of the 2D array on EVA foam caused a 6.215% reduction in RSSI. Thus, advanced damage stages will cause the direction of RSSI gradient to change with values greater than 6%.
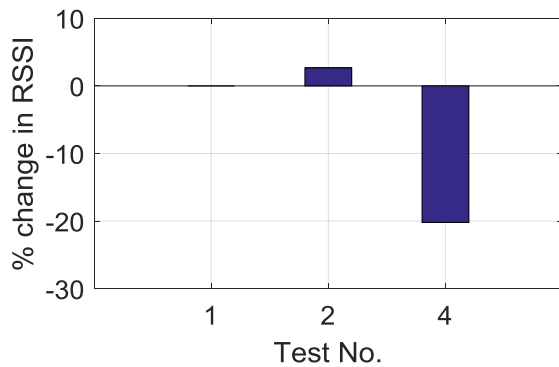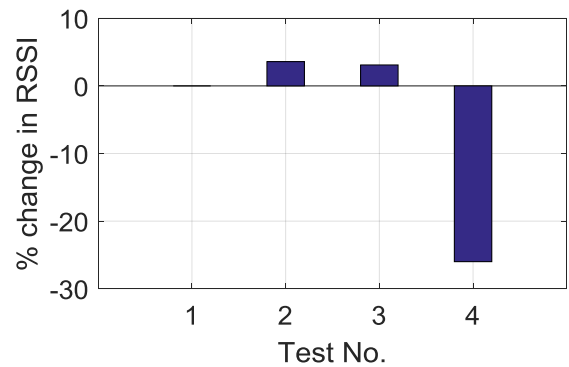
(a) (b)

Figure 4.20 Percentage change in RSSI of a single-tag with respect to the undamaged condition:

(a) 0.4290-in thick polystyrene foam, (b) 0.-in thick EVA foam.
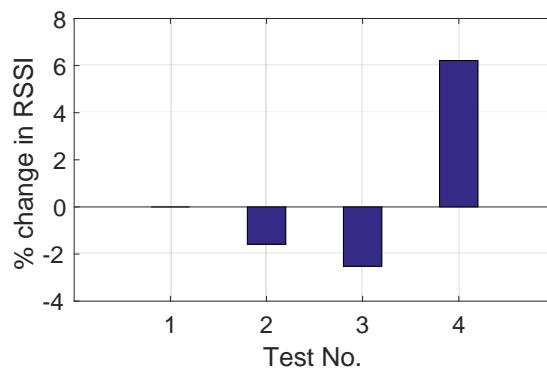
Figure 4.21 Percentage change in RSSI of the control tag in a 2D array with respect to the

undamaged condition.

In summary, single-tag and multiple-tag configurations can both be used for specific crack-monitoring situations. As percentage changes in RSSI in single-tag configurations are larger, small cracks can be monitored more accurately. On the other hand, multiple-tag arrangements reveal lower percentage changes in RSSI due to coupling effects. However, these gradients are sufficiently large to detect changes in longer cracks, which would produce larger percentage changes in RSSI.

2D arrays can also cover larger areas for expanded pervasiveness. The behavior of the sensing system makes percentage change in RSSI a competent damage index for crack monitoring.

CHAPTER 5. CRACK PROPAGATION TESTS

This chapter presents the performance evaluation of the RFID-based crack sensors when detecting crack propagation. The sensors were mounted on especially designed aluminum plates that were subjected to static tension failure tests. Single- and multiple-tag configurations were examined. In addition to correlating crack propagation to changes in backscatter power, a relationship has been found between changes in backscatter power and the region of mechanical behavior of the structure (ie., elastic, plastic or strain hardening regions). Section 5.1 presents the tests performed to refine sensor assembly and mounting for improved sensitivity to damage. Sections 5.2 and 5.3 discuss the performance evaluation of the single and multiple sensor configurations, respectively.

1. Preliminary Tests for Sensor Refinement

a. Specimen Design

The test specimens designed for single-sensor and multiple-sensor configurations are shown in Figures 5.1 and 5.2. The dimensions of these samples were chosen to conform to the proportions of a plate. The inclusion of anti-buckling plates prevented out-of-plane deformation in the plate during testing. All plates and anti-buckling plates were 0.25-in thick. A space of 1 in by 2 in was allowed for the grips of the testing machine, indicated by the red shaded regions. A pre-crack line of approximately 0.0875 in in the small sample and 0.1875 in in the large sample was made at the notch tip to ensure that the direction of crack propagation was straight. Figures 5.1d and 5.2d also show the general location of the sensors. The control tag was placed at the tip of the pre-crack line. (See section 5.1.4 for the explanation of the initial crack formation.) A straight through notch was machined into the specimens to ensure the location of crack formation. The dimensions of these

notches were calculated according to ASTM 399-12. The materials of the plate and the anti-buckling plates are highly machinable MIC6 aluminum and 6061 aluminum, respectively. Details of notch dimension calculations and material properties are presented in Appendix C.
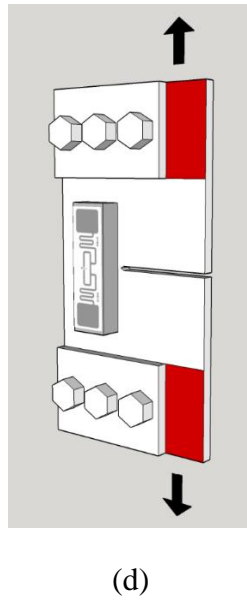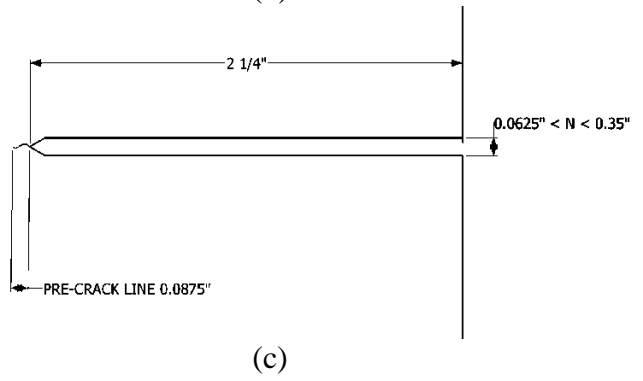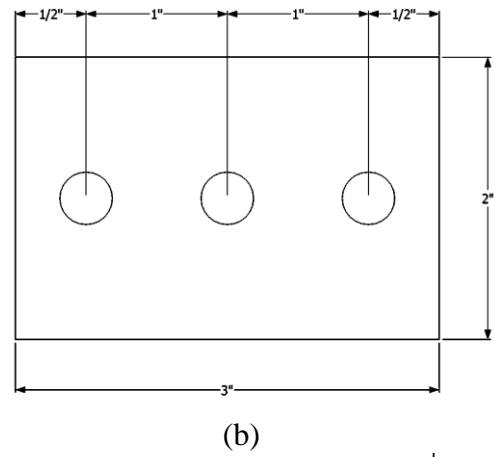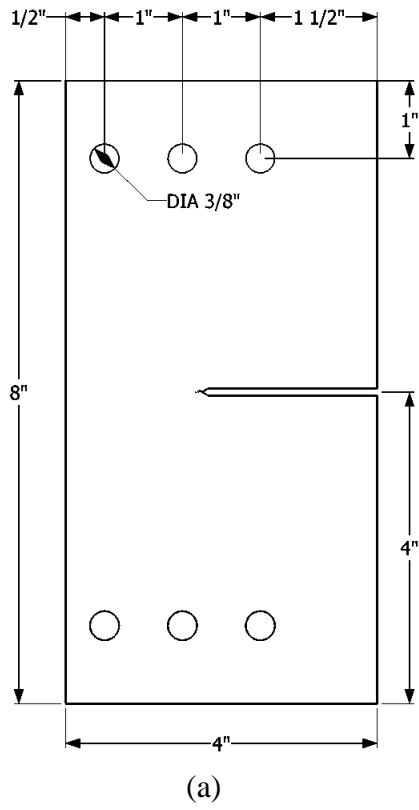
Figure 5.1 Specimen for single sensor testing: (a) plate dimensions, (b) anti-buckling plate dimensions, (c) notch dimensions, (d) assembly and force location.
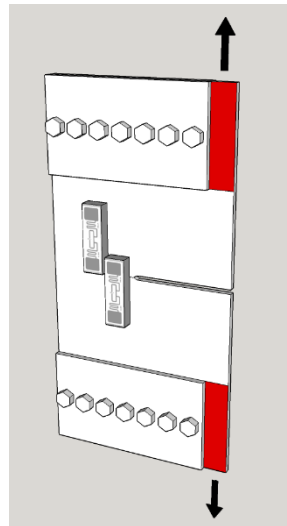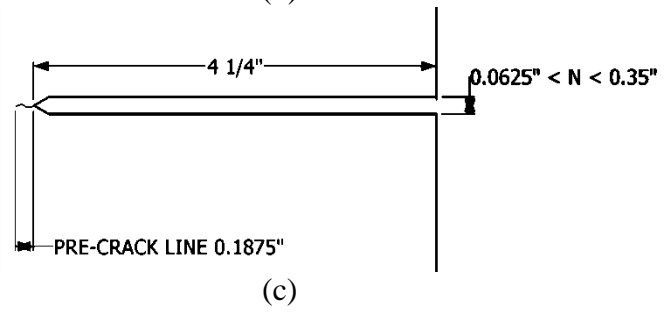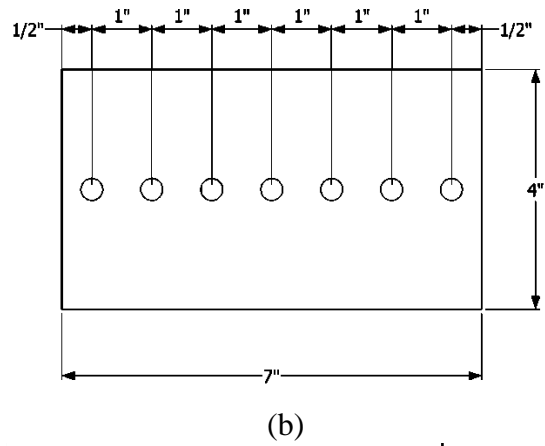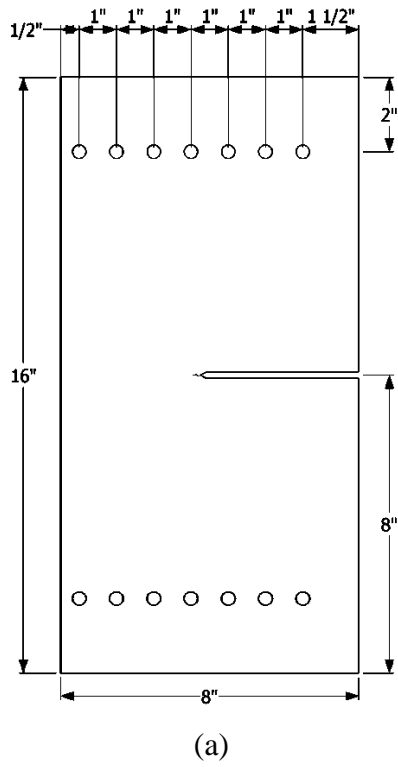
Figure 5.2 Specimen for multiple sensor testing: (a) plate dimensions, (b) anti-buckling plate dimensions, (c) notch dimensions, (d) assembly and force location.

b. Sensor Preparation

Each aluminum surface was prepared by sandblasting to an even and clean finish using a benchtop blasting cabinet. The bonding process of sensor assembly and mounting was performed using Loctite Epoxy Quick Set, a two-part adhesive consisting of epoxy resin and a hardener that achieves a tensile shear strength of 3437 psi (±58 psi) in 24 hours. Epoxy resin was chosen for the assembly of the present crack sensor because it is typically used in strain-sensitive applications, such as crack sensing with optical fiber. Epoxy resin had also been manually tested for interference with RFID power signals in the laboratory and no significant effect had been found.

Sensor assembly and mounting consists of adhering two interfaces (Refer to Figure 4.1.): the tag-substrate interface for assembly and the substrate-structure interface for mounting. During the initial tests described in this section, the entire surface of the RFID tag was attached to the substrate using a 1-mm thick layer of epoxy. Likewise, the entire surface of the substrate was attached to the testing sample during initial tests only. For a full description of the assembly and mounting process of the initial and final samples, refer to Appendix A.

c. Digital Image Correlation

Samples 4 and 1L were analyzed for strain and displacement mapping using digital image correlation (DIC). This would allow the detection of stress or strain concentrations at the crack tip to track damage occurrence during the test and aid in the correlation of changes in backscatter power. The program used to perform this analysis was Ncorr v1.2, an open source 2D MATLAB add-on [29]. DIC uses image processing techniques to track small subsections of current images, called subsets, in relation to an undisturbed reference image. DIC parameters include subset radius

and spacing, and iterative solver options that include a difference norm and iteration number cutoff. The problem is solved using non-linear optimization with the Gauss-Newton non-linear iterative least squares method. The software calculates strain and displacement using Green-Lagrange and Euler-Almansi strain tensors and displacement gradients. The parameters used for DIC in each sample along with the strain and displacement maps are shown in Appendix D.

d. Test Procedure

Tensile testing was completed with an ADMET eXpert 1655 Hydraulic Universal Test System (Norwood, MA) with 250kN load cell. The grips of the instrument were clamped flush with the interior edge of the anti-buckling plates. Images for DIC were collected with a Canon EOS 70D camera using a Neewer digital timer remote EZa. If DIC was implemented, samples were sprayed carefully with charcoal fine texture spray paint on a white primer to obtain a speckle pattern on the side opposite to the RFID tag in the area of crack propagation, as shown in Figure 5.3. A red filtered LED lamp was used to render a clearer speckle pattern on the spray-painted side of the sample. The camera, lamp and reader antenna were all placed on tripods to be level with the area of interest.
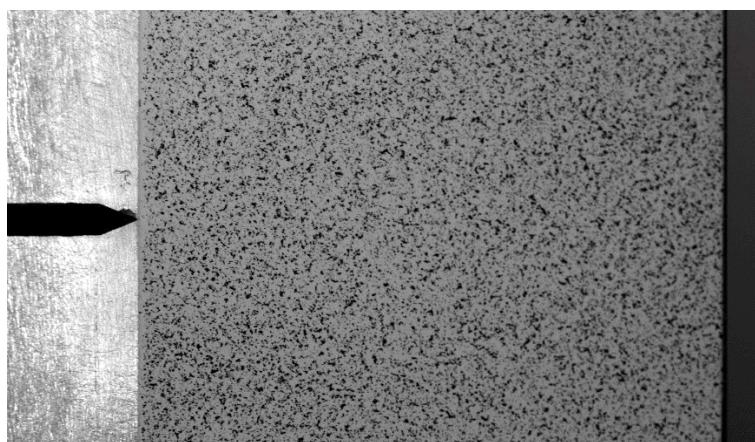

Figure 5.3 Speckle pattern on aluminum sample for DIC.

Pre-cracks were formed by applying a tensile load at low strain rate, typically 0.0025 in/min until a maximum load was reached followed by a visible crack extending from the machined notch, approximately 0.0875 inches for small samples and 0.1875 inches for large samples. The sample was monitored at roughly 10x magnification during this operation and crack length was measured to 0.05-mm precision. Table 5.1 shows a summary of the dimension of pre-cracking lines and dimensions of propagation area.

Table 5.1 Pre-crack information.

Sample ID	Notch width and length	Pre-crack length	Complete crack length (including pre-crack line)
1	0.1025 in (2.60 mm) x 2.23 in (56.68 mm)	0.557 in (14.16 mm)	1.720 in (43.69 mm)
2	0.0960 in (2.44 mm) x 2.22 in (56.39mm)	0.157 in (4.00 mm)	1.730 in (43.94 mm)
3	0.0960 in (2.44 mm) x 2.237 in (56.82 mm)	0.217 in (5.50 mm)	1.713 in (43.51 mm)
4	0.0965 in (2.45 mm) x 2.252 in (57.20 mm)	0.112 in (2.85 mm)	1.700 in (43.17 mm)
1L	0.0945 in (2.40 mm) x 4.250 in (107.95 mm)	0.220 in (5.59 mm)	3.712 in (94.28 mm)

During crack propagation, the tensile testing profile consisted of periodic strain and pause cycles in samples 3, 4 and 1L to facilitate image collection of the speckle pattern and 15 second RSSI reading during a static condition with the antenna placed 3ft from tags. The testing profile of sample 1 consisted of taking the sample to the plastic region and pausing the test to collect the 15

second RSSI reading at the peak loading and after unloading. The cycle was repeated until reaching full fracture. The tensile testing profile of sample 2 consisted of applying the strain rate continuously while collecting a 3360 second long RSSI reading during the duration of the test. All samples were taken to or near the ultimate condition. Specific strain rates for each sample are listed in Table 5.2. The environment was kept as static as possible aside from testing equipment, including isolation from nearby cell phone and Wi-Fi signals. Appendix B contains a complete photographic documentation of the testing preparation and procedure of all samples.

Table 5.2 Strain rates per sample tested.

Sample ID	Strain rate (in/min)
1	0.05
2	0.01 (up to 400 lb); 0.002 (from 400 lb to ultimate)
3	0.01 (up to 0.02 in displacement); 0.0075 (from 0.02 in to ultimate)
4	0.006
1L	0.015

e. Results

Sample 1

The test procedure for Sample 1 consisted of loading the sample until the elastic region was past, until the load would drop approximately 5 lbs. Each one of these instances consisted of a cycle. At the moment of peak loading, the test would be paused and an RSSI reading and photo of the propagating crack would be taken. The sample would be unloaded and reloaded for the next cycle. Figure 9.15 in Appendix D shows a selection of photos of the crack as it propagated in sample 1. Figure 5.4 shows the backscatter power changes and crack length at the end of each cycle.

It also shows the load-displacement curves for each cycle, the first cycle being the one with the smallest position (distance between the grips) and the last cycle containing the largest displacements. The sensor was oriented with the tag IC facing left and the crack propagating above the IC (see Figure 9.10). It was placed flush with the outer edge of the aluminum sample.

The relationship between crack length and loading cycle seems to be linear. A linear fit reveals that this relation can be described by the equation:

$$x = 1.0388n + 2.2518 \tag{5.1}$$

where, n is the cycle number and x is the crack length. This fit has a coefficient of correlation of 0.9924, which indicates a precise regression as it is very close to unity. However, the changes in backscatter power do not behave as predictably in relation to the cycle of loading.

The crack is present under the tag at the second cycle. Cycle 1 presents an increase in RSSI and Cycle 2 a decrease in RSSI. In Cycle 3, backscatter seems to increase slightly, only to continue dropping until Cycle 5. In cycles 6-11, RSSI is mostly constant while the crack continues to increase in length. During the last nine cycles, RSSI generally drops, except between Cycles 19 and 20, and Cycles 22 and 23. This region of the last nine cycles is where approximately 80% of the sample displacement occurs. During the last four cycles, it is clear from Figure 5.4c that strain hardening occurs. In this region, RSSI consistently decreases significantly and damage reaches the ultimate state. However, the changes in backscatter power cannot be clearly correlated to crack damage with this sample.
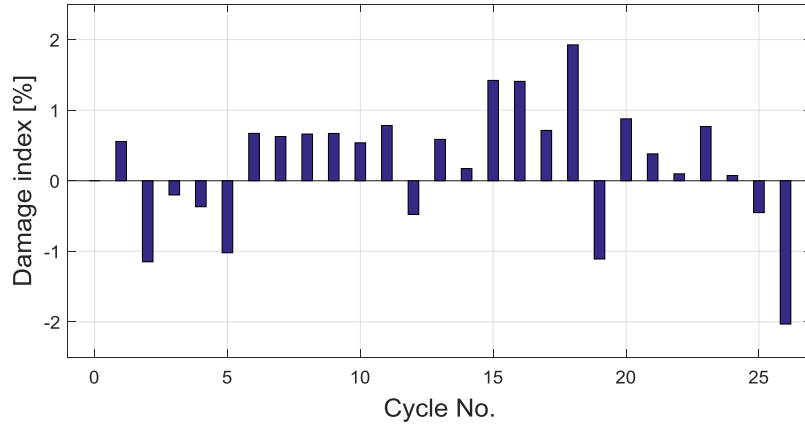
(a)
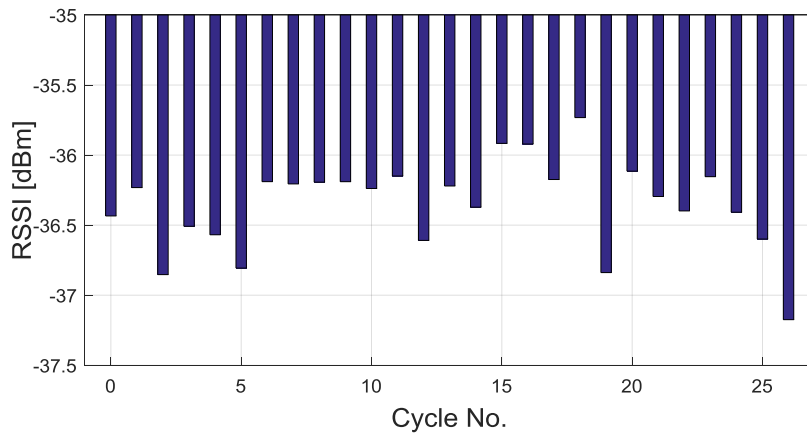
(b)
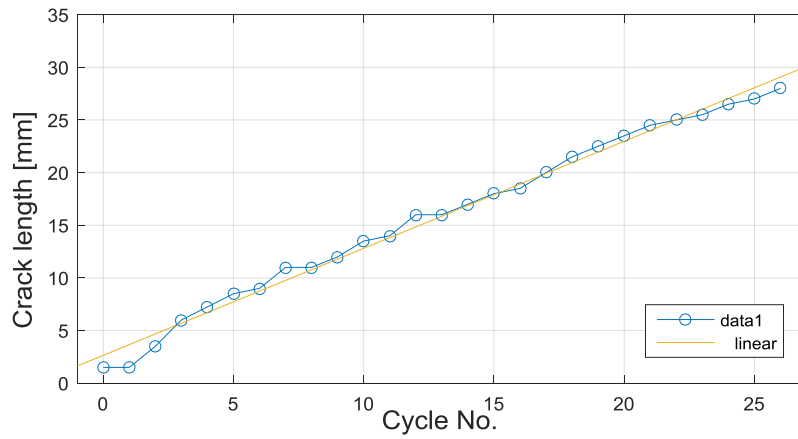
(c)

Figure 5.4 Results for sample 1: (a) Damage indices per cycle, (b) RSSI changes per cycle, (c) crack length per cycle, (d) load-displacement curves.
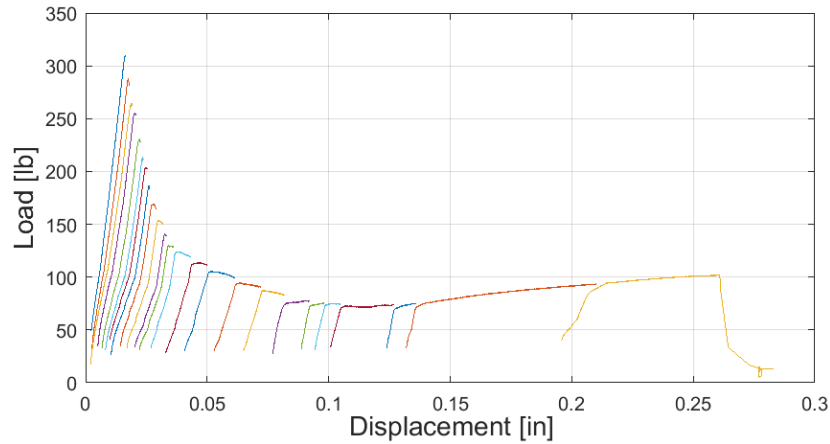
(d)

Figure 5.4. Results for sample 1: (a) Damage indices per cycle, (b) RSSI changes per cycle, (c) crack length per cycle, (d) load-displacement curves (continued).

Sample 2

Testing of Sample 2 was performed with a continuous RSSI reading from initial loading until ultimate. The sensor was oriented with the IC facing left and the crack propagating below the IC (see Figure 9.10). The sensor was placed at the tip of the pre-crack line. The RSSI time history and load-displacement curve are shown in Figure 5.5. The total test time was 56 minutes. The load-displacement curve is missing part of the initial elastic region because the sampling rate of the controller of the uniaxial testing machine was set so that only 2,600 seconds (43.33 minutes) of data could be stored. Since the reader uses FHSS, each channel would reveal a different discrete value of RSSI and averaging could not be used. The result is the time history shown below where no distinct value of RSSI can be attributed to the stage of crack propagation nor to mechanical behavior. However, it can be noted that after 1,688 seconds, the channels receiving backscatter power of -45 dBm up to that point were then receiving increased power. The strain-hardening region was initiated at about the same time (at about 0.065-in displacement). Moreover, at the latter stages of strain-hardening right before ultimate failure, after about 3,000 seconds, RSSI no longer presents values of -39 dBm and contains more signals of -45 dBm. At the ultimate point, RSSI drops off.

56
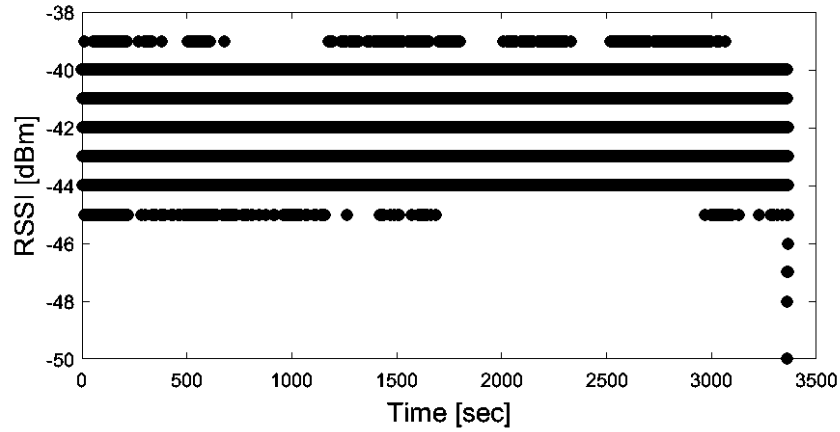
(a)
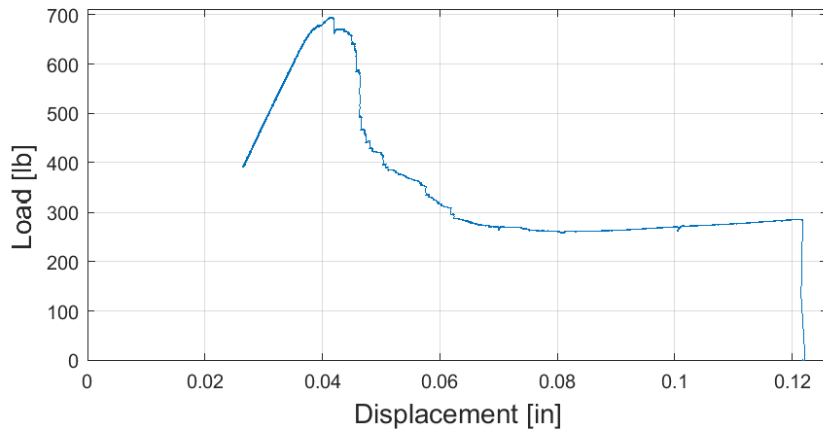
(b)

Figure 5.5 Results for sample 2: (a) RSSI time history, (b) load-displacement curve.

Sample 3

The sensor in this sample was also placed with the IC facing the left side of the sample with the

crack propagating below it (see Figure 9.10). It was placed at the tip of the pre-crack line. The test

was performed by separating the machine grips to a certain distance, pausing, and taking an RSSI

reading. Figure 5.6 shows the resulting averaged RSSI readings at each pause or step and the load-

displacement curve. The uniaxial testing machine recorded only 1,300 seconds of data because it

was again set at a very high sampling rate. This sample showed no clear relationship between backscatter power and crack presence or mechanical region.
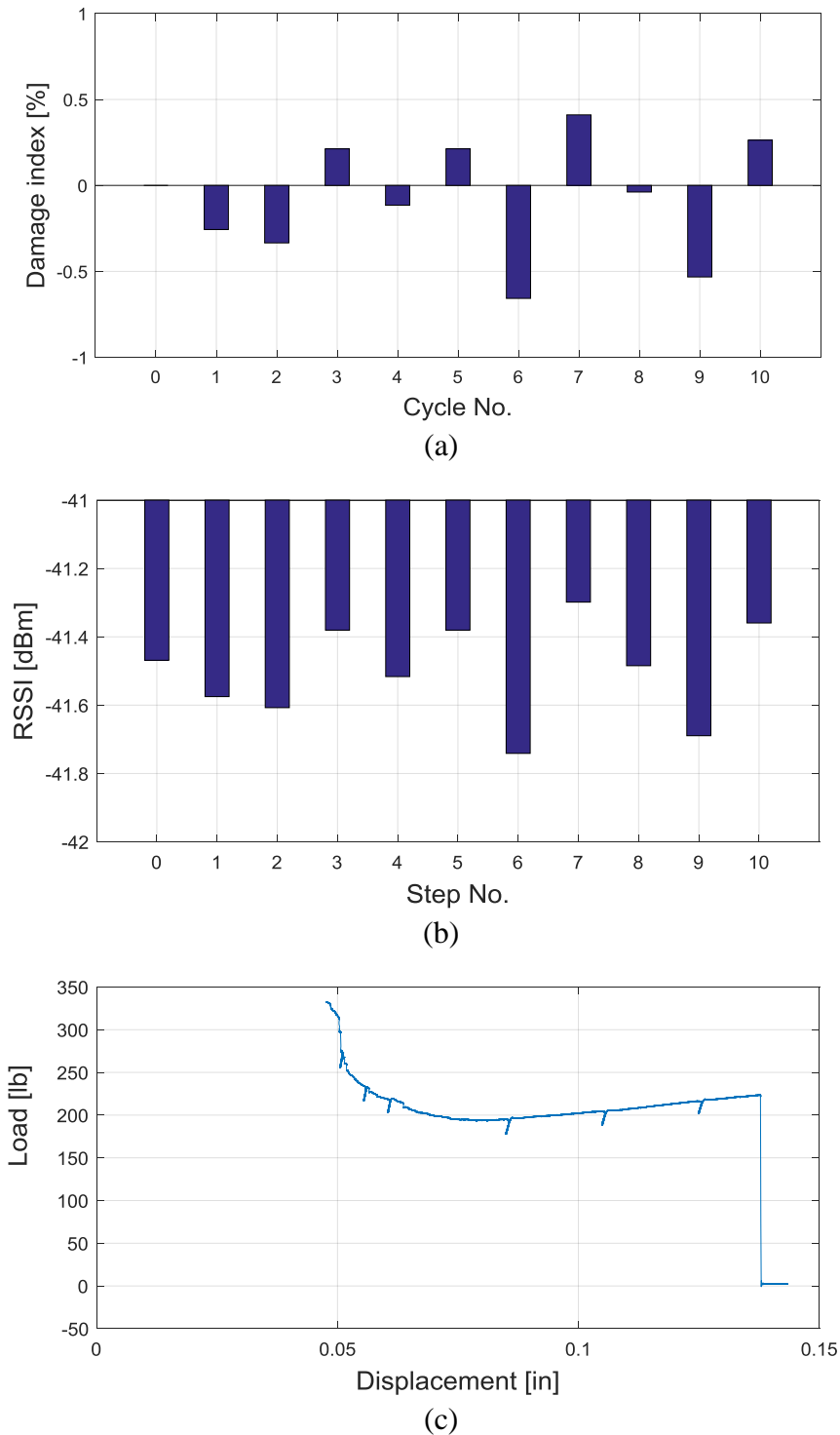

(a)

(b)

(c)

Figure 5.6 Results for sample 3: (a) Damage indices per step, (b) RSSI changes per step, (c) load-displacement curve.

f.   Sensor Refinement

Because of the sudden failure of previous tests and the lack of correlation between crack propagation and backscatter power, it was hypothesized that the application of adhesive to the full interface areas might be interfering with the deformation of the substrate. This deformation would alter the radiation pattern of the tag, thus, giving indication of damage presence. For this reason, the assembly and mounting procedure was modified such that only the outermost half of the tag antenna patches was adhered to the substrate. The projection of this region onto the substrate-structure interface was also the only area on which epoxy was applied. See Figure 5.7 below, and refer to Appendix A for a comparison of the initial and revisited sensor assembly and mounting procedures. The thickness of the adhesive was maintained to approximately 1 mm.

Figure 5.7 New adhesive area for sensor assembly and mounting.

2. Crack Propagation Test of Single Sensor

The sensor assembly and mounting for Sample 4 was performed according to the description in Section 5.1.6. Photos of the new assembly and mounting procedures have been documented in Appendix A. The sensor was placed such that the tag IC was facing right and the crack would be propagating below the IC (see Figure 9.10). The testing procedure of Sample 4 consisted of loading the sample at a constant displacement rate, and pausing the test at regular intervals to collect an RSSI reading statically. Simultaneously, photos of a speckle-pattern for DIC on the side opposing the sensor location were taken to trace the crack propagation and measure the strain and displacement field in the critical area. Figure 9.16 in Appendix D shows a selection of photos of the propagating crack and the speckle pattern that were used for DIC. Photos of the testing setup can be found in Appendix C. The averaged RSSI values and load-displacement curve are shown in Figure 5.8. Figure 5.9 shows the strain field calculated, using the Euler-Almansi method, for the critical area at the end of six critical stages.

From Steps 1-4, RSSI decreases while the specimen remains in the elastic region during the first 10% of its total deformation. During this stage, open crack length is between 0 and 2.18 mm. After Step 4, the crack length goes beyond the pre-crack length for this sample, 2.85 mm. The strain at the tip of the crack is approximately 0.002 mm/mm at the end of this stage.

From Steps 5-10, RSSI generally increases until the end of the elastic region which culminates at the peak load at approximately 818 lbs. The crack length reaches 6.545 mm at this stage, 3.695 mm below the sensor, which has a total width of 20.55 mm. The strain at the end of this stage has greatly increased to about 0.02 mm/mm.

During Steps 11-16, RSSI gradually increases after a very significant drop in RSSI. This stage marks the initiation of the plastic region, with the load dropping approximately 60%. When the crack length is 23.40 mm, the crack has moved completely under the sensor. This occurs after Step 13. The crack length is 29.45 mm at the end of Step 16, and strain is approximately 0.03 mm/mm.

During Steps 17-22, RSSI remains stable while the first part of the strain hardening region begins. Crack length reaches 36.55 mm at the end of this stage, and the crack width is approximately 0.5 mm. At this end of this stage, strain at the tip of the crack reaches 0.045 mm/mm.

After this, RSSI increases drastically from steps 23-30, marking great damage accumulation. During this stage, strain-hardening continues, the strain at the tip of the crack remains approximately constant at 0.045 mm/mm and the length reaches 40.36 mm. Crack width has reached approximately 1 mm.
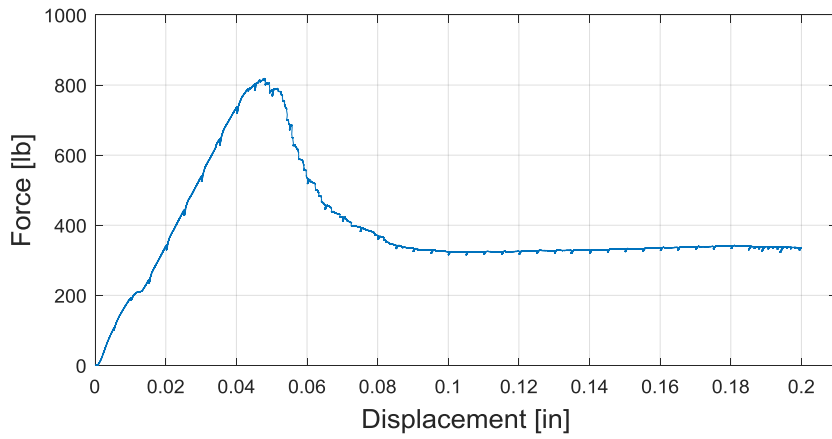
During the final Steps 31-41, RSSI continues to gradually increase in the strain hardening region. The strain at the tip of the crack right before failure is 0.055 mm/mm when the length reaches 41.45 mm. Crack width is approximate 1.6 mm at the end of this stage.
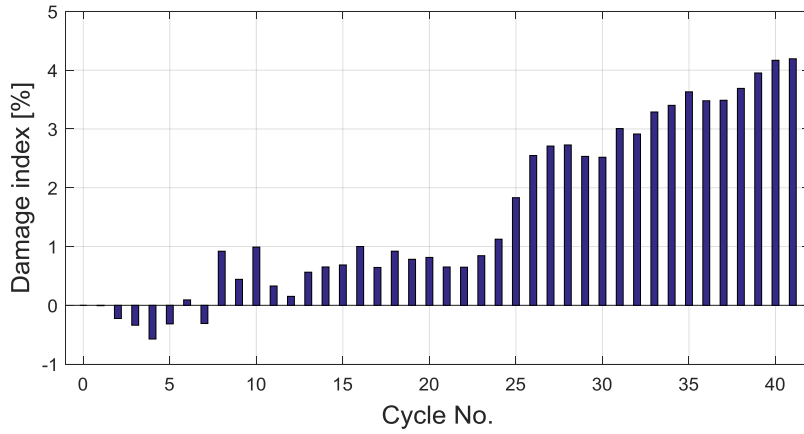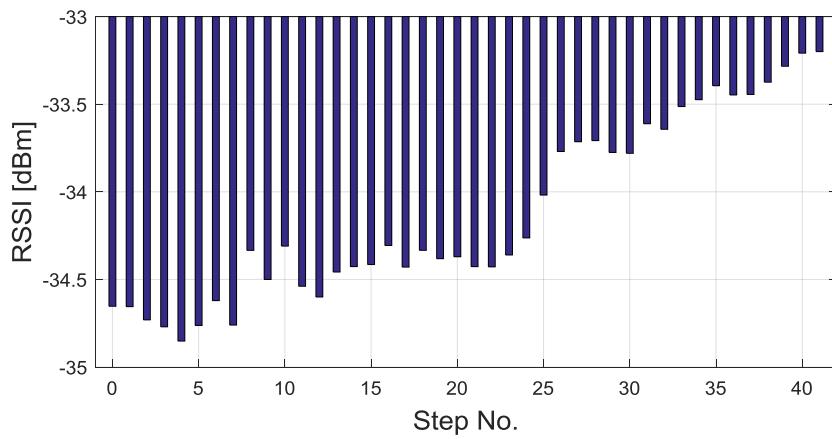
Figure 5.8 Results for sample 4: (a) Damage indices per step, (b) RSSI changes per step, (c) load-displacement curve.
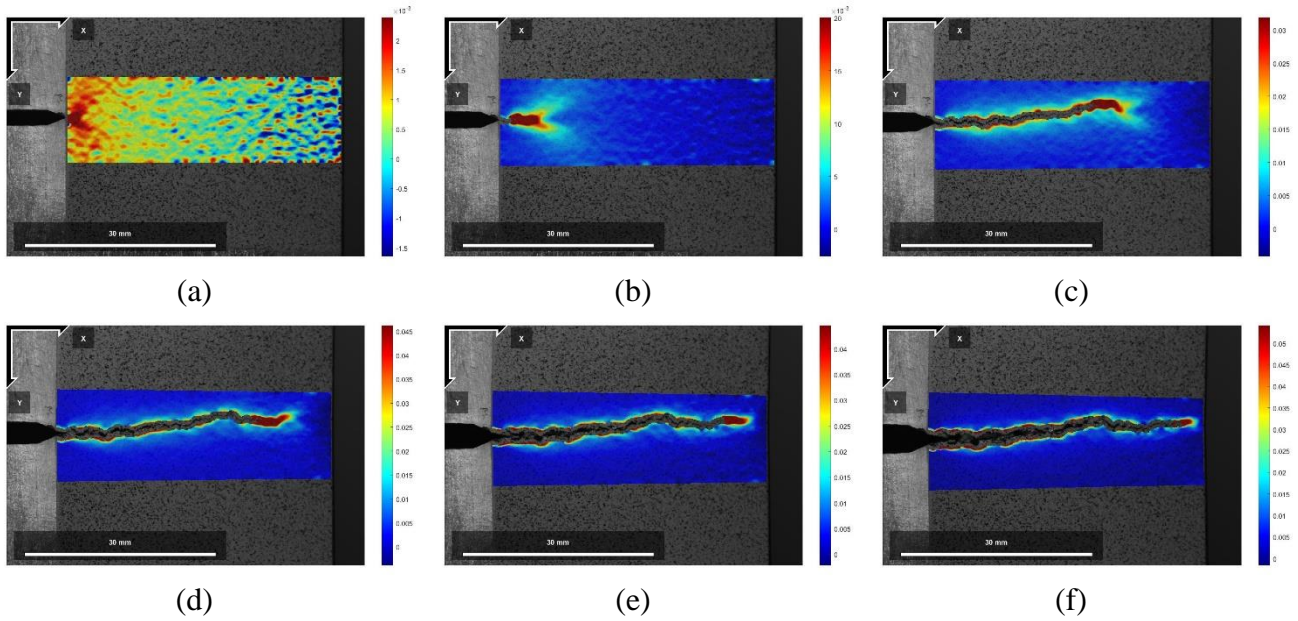
Figure 5.9 Strain maps at the end of: (a) step 4, (b) step 10, (c) step 16, (d) step 22, (e) step 30, (f) step 41.

3. Crack Propagation Test of Multiple Sensors

In order to settle for the best configuration consisting of two RFID tags, three different configurations were tested to find the one that had the best constructive interference. Figure 5.10 shows the configurations selected for evaluation in comparison to the single sensor. The single sensor was labeled Tag T-B (the control tag in way of the crack propagation). In Configurations C2-C4, this sensor is the lower-most, or right-most one, while the other sensor is Tag T-A. Table 5.3 shows the resulting RSSI averages on Tag T-B in each configuration. It was determined that Configuration C4 where the sensors were placed in a zig-zag manner increased RSSI in the control tag the most. Spacing in the vertical direction was 0.25 in and, in the horizontal direction was 0.125 in.
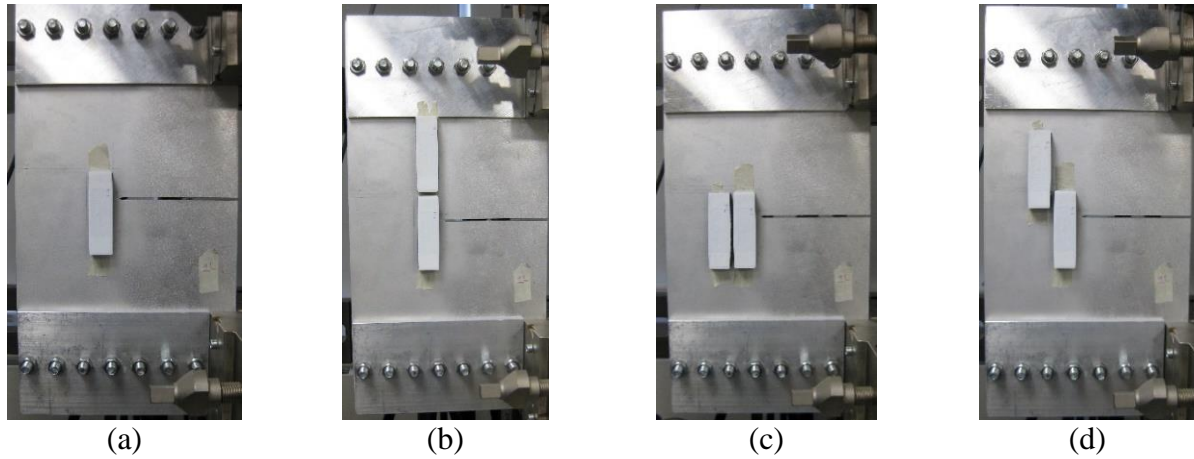
Figure 5.10 Configurations for a multiple sensor configuration: (a) C1, (b) C2, (c) C3, (d) C4.

Table 5.3 RSSI for various multiple sensor configurations.

Trial	RSSI (dBm)			
	C1	C2	C3	C4
1	-43.2857	-40.9916	-48.3039	-35.8220
2	-43.2927	-40.9933	-48.2927	-35.5588
3	-43.1365	-40.9377	-48.3268	-35.8190
Average	**-43.2383**	**-40.9742**	**-48.3078**	**-35.7333**

Similar to Sample 4, the sensors on Sample 1L were assembled and mounted according to the description in Section 5.1.6. Both sensors were mounted with the ICs facing left (see Figure 9.10). The crack propagated above the IC of Tag T-B. The testing procedure of Sample 1L consisted of loading the sample at a constant displacement rate and, pausing the test at regular intervals to statically collect an RSSI reading of both RFID tags at once. Simultaneously, photos of a speckle-pattern for DIC on the side opposing the sensor location were taken to trace the crack propagation and measure the strain and displacement field in the critical area. Figure 9.17 in Appendix D shows

a selection of photos of the propagating crack and the speckle pattern that were used for DIC Photos of the testing setup can be found in Appendix C.

The averaged RSSI values for each tag and the load-displacement curve are shown in Figure 5.11. Figure 5.12 shows the strain field calculated using the Euler-Almansi method of the critical area at the end of four critical stages. The first stage consists of Steps 1-2, where RSSI in Tag T-B decreases. This stage corresponds to the elastic region of approximately the first 10% of total displacement. Crack length at the end of this stage is 7.45 mm and the strain at the tip of the crack is approximately 0.0016 mm/mm. During this stage, the crack has propagated 1.86 mm beyond the pre-crack line.

The second stage consists of Steps 3-4, where RSSI increases and the end of the elastic region is reached. The strain at the tip of the crack at the end of this stage remains at approximately 0.0016 mm/mm and the crack has propagated to a length of 11.17 mm. As sensor T-B is 21.30 mm wide, the crack has gone 5.58 mm underneath the sensor T-B.

The next stage takes place during Steps 5-7. Here, the plastic region is initiated and RSSI increases gradually and significantly. The strain at the tip of the crack shows a large increase up to 0.036 mm/mm, and the crack opens under the full width of Sensor T-B and past the width of Sensor T-A ,with a length of 68.09 mm. The crack also begins to exhibit a width identifiable from the photos taken for DIC as approximately 0.5 mm.

The fourth and final stage covers Steps 8-22, where RSSI decreases gradually until failure is reached. This stage coincides with the strain-hardening region. Strain at the tip of the crack peaks at 0.06 mm/mm, and the crack reaches a length of 90.43 mm in the final step before breakage, 3.85 mm away from the sample edge. The crack width is approximate 3 mm at the end of this stage.
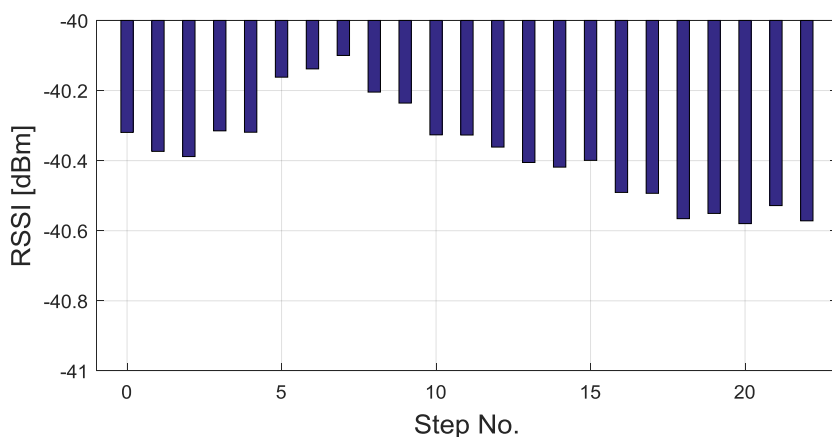
Sensor T-A exhibits a similar trend as T-B with RSSI changes presenting larger ranges. From Steps 1-7, RSSI is consistently increasing, while, from Steps 8-22, it decreases.
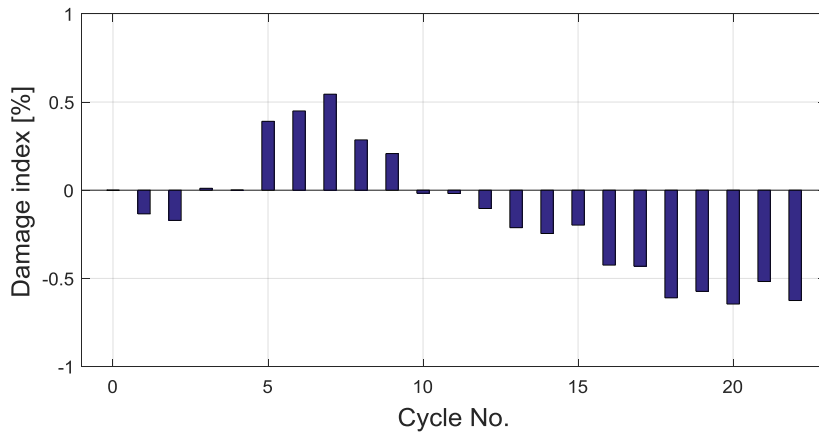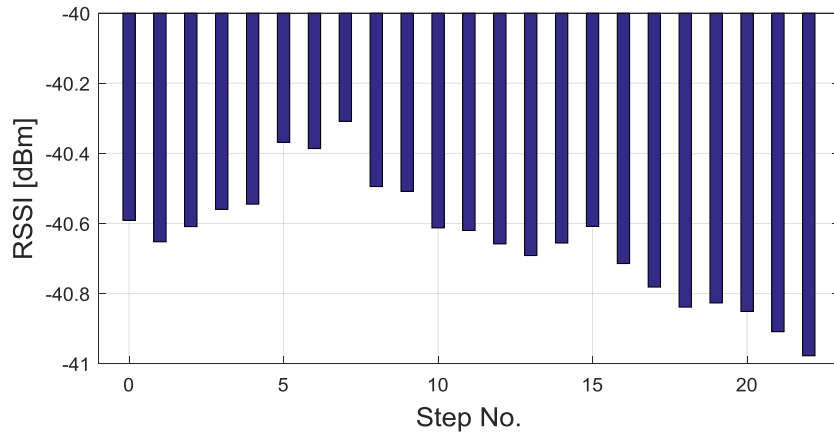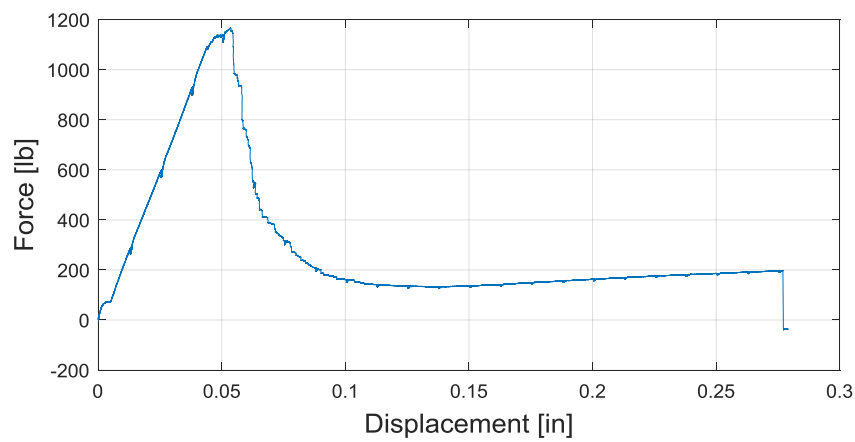

(a)
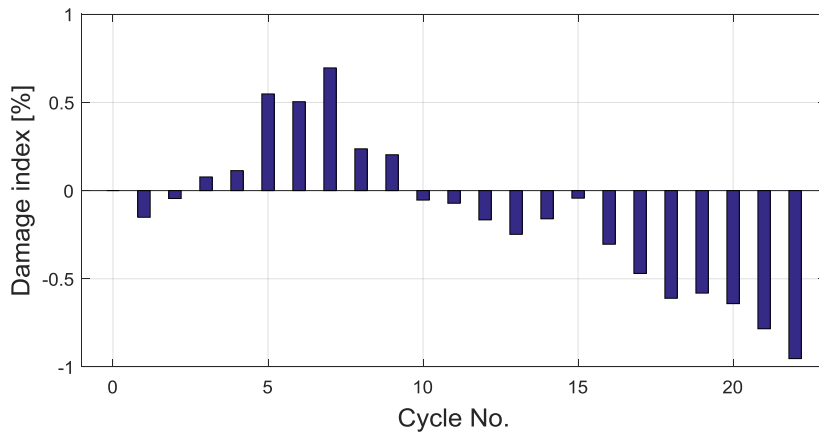
(b)

(c)

Figure 5.11 Results for sample 1L: (a) Damage indices per step in tag T-B, (b) Damage indices per step in tag T-A, (c) RSSI changes per step in tag T-B (control tag), (d) RSSI changes per step in tag T-A, (e) load-displacement curve.
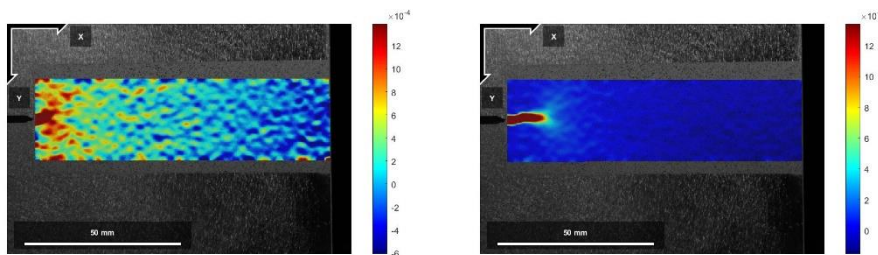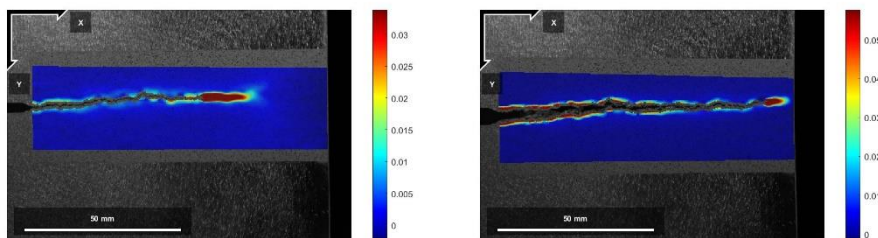
(d)

(e)

Figure 5.11 Results for sample 1L: (a) Damage indices per step in tag T-B, (b) Damage indices per step in tag T-A, (c) RSSI changes per step in tag T-B (control tag), (d) RSSI changes per step in tag T-A, (e) load-displacement curve (continued).

(a)

(b)

(c)

(d)

Figure 5.12 Strain maps at the end of: (a) step 2, (b) step 4, (c) step 7, (d) step 22.

67

CHAPTER 6. CONCLUSIONS, RECOMMENDATIONS AND SUGGESTED RESEARCH

1. Conclusions

An RFID-based crack sensor was successfully developed using low-cost commercial tags and its performance was validated with comprehensive laboratory-scale experiments. The percentage change in backscatter power from the RFID tags is a relevant damage index, as it is sensitive to crack propagation. The magnitude of the damage index consistently increases as crack damage gradually propagates from the metallic specimen to the substrate and the tag. This demonstrates the potential of the developed sensors for crack detection. Furthermore, the algebraic sign of the damage index indicates the location of damage within a tag with respect to its IC. A crack sensor with a single-tag configuration displayed the best performance in crack detection with a high damage index change. Yet, a 2D array of tags is preferred to increase the sensing range. Guidelines on optimal spacing and configuration of multiple tags for the development and operation of RFID-based crack-sensor arrays were defined. RFID crack-sensor arrays are also effective at crack-propagation monitoring, as indicated by the significant damage index changes measured in laboratory experimentation. Therefore, the developed system significantly propels the advancement of crack-propagation monitoring on steel structures at a low cost, enabling extensive usage on welded cover plates within a restricted budget.

2. Recommendations

The developed system is specifically recommended for monitoring the growth of initiated cracks of metal structures. As discussed in the literature survey, steel bridges have specific fatigue

crack-prone members such as major connections, welded cover plates, and gusset plates. This sensor could be attached near the tip of the crack to monitor the growth regularly to prioritize retrofit schedule based on limited budget. Also, this sensor could be easily carried by visual inspectors when they conduct mandated inspection; attach these at suspicious spots for cracks and check the baseline-received power. In their subsequent in-depth inspection, or the following routine inspection, they could check the changes in the received power to check the growth of the crack. In addition, the installed sensors can be scanned when Connecticut's PhotoLog Services are scheduled to pass nearby.

3. Suggested Future Research

For wide-spread field implementation, three more applied research topics are suggested. First, is the development of a guideline to set up a temperature calibration curve for a bridge. Because structural responses are directly affected by temperature due to thermal expansion/shrinkage, the baseline information needs to be set before using this sensor for crack detection. If temperature in maintained within a narrow range, e.g., California, this procedure may be omitted.

Next, the performance of the developed system on a full-scale bridge should be validated. The scope of this project is a pilot study in the laboratory, and the system worked well within a controlled mechanical system with narrow temperature range. However, the received power from the field condition should be interrupted by adjacent steel members, passing vehicles, or any electromagnetic waves in the ultra-high frequency range (~900 MHz). Therefore, further environmental hardening or field arrangement of the developed system to minimize the effects are recommended.

Last, but not least, the system has a great potential to be installed as a wireless monitoring system. The sensor itself is passive, therefore, no wires are needed for power supply or data transmission. However, the data logger requires both power and the means of data transmission, e.g., cellular modem. With current development of microprocessors, a data-logging system using a handheld reader and a mobile computer, which is powered by a solar panel, could be pursued for fully wireless operation. A cellular modem can be used to connect the mobile computer to the Internet, so that remote users can execute nearly continuous monitoring of crack-prone sites.

CHAPTER 7. IMPLEMENTATION OF RESEARCH RESULTS

The system will be fine-tuned for field implementation. Typically, a bridge site is located in the field without access to a power source. Therefore, wireless operation of crack detection is critical. Opportunely, a wireless handheld reader was purchased through this project, and a basic function to read the RSSI has been identified showing very high potential for such a system developed in the near future. Specific tasks for implementation have been listed to overcome the current limitations of system for field demonstration.

1. Task 1: Field demonstration treatment

Because of all unknown environmental factors in the field, a careful field testing plan should be prepared. The PI suggests the following steps to check:

a. Configuration of tag and the reader.

b. Optimal read distance using a handheld reader.

c. Sensor arrangement (single, multiple, arrangement) optimization to have highest baseline received power.

d. Means to remain constant read distance, e.g., a standard length reader handle or a motorized robot-type carrier.

When the configuration, read distance, sensor arrangement, and effective means to maintain controlled read distance has been determined, the sensing system is ready for the field demonstration.

2. Task 2: Temperature calibration curve

Because the received power will be dependent on temperature of the member, the baseline calibration curve for a target bridge (or a target member) should be pre-determined. Using the sensing system prepared in Task 2, the received power will be measured for different temperature conditions, ranging from 0° to 100°F. Then, the temperature correction coefficients will be developed from the slopes of the curve, and used to calibrate the future on-site measurement.

3. Task 3: Damage sensitivity demonstration

If there is a target bridge with a crack, this bridge would be the ideal testbed to check the damage sensitivity of the developed system. However, if there is no such bridge in Connecticut, a sacrificial member can be developed near a fatigue-prone zone, induce pre-crack, leave the crack to propagate, and measure the changes of the received power of the tag to validate the damage sensitivity in the field. For a long-term experiment, the member will be made of steel, and its propagation will be checked each month. For a short-term experiment, the member could be made of aluminum or have more significant cracks in the beginning to accelerate the crack propagation, and check the changes of the received power. The goal of this study is to find a reasonable damage index (% change of the received power) at the crack before it could develop to a sudden fracture, so that the cracked region could be retrofitted in time. It is beneficial to involve other traditional sensors (such as strain gage, fiber optic sensors, and digital image correlation) for this task.

4. Task 4: Autonomous monitoring program development

Eventually, the PI envisions this system to be under unmanned autonomous operation through the Internet. To do that, it requires many steps.

- **Power source**: A stable power source such as AC power or solar panel should be installed in the field to supply power for the mobile computer, a reader, and, possible monitoring accessories.

- **Computation source**: A mobile computer should be prepared so that it could support all software components: the RFID reader software, computation core (Matlab Mobile or Wolfram), and internet-related software (Remote Desktop, VNC, FTP, OneDrive, etc.), with all necessary hardware components: high-speed CPU, on-board memory, abundant data storage space, multiple USB3 and serial ports for expandability, etc.

- **Monitoring schedule**: Crack-propagation speed is dependent on material, static loading, dynamic loading cycle, other external sources, and its own status of crack propagation. The monitoring schedule should be set up so that the progression of the crack is effectively monitored.

CHAPTER 8.   REFERENCES

[1]   Haghani R, Al-Emrani M and Heshmati M 2012 Fatigue-Prone Details in Steel Bridges *Buildings* **2** 456–76. DOI: 10.3390/buildings2040456.

[2]   Dexter R J and Ocel J M 2013 *Manual for Repair and Retrofit of Fatigue Cracks in Steel Bridges (FHWA-IF-13-020)* (McLean, VA)

[3]   Mertz D 2015 *Steel Bridge Design Handbook Design for Fatigue (FHWA-HIF-16-002)* vol 12(Washington, D.C.)

[4]   Fisher J W, Albrecht P A, Yen B T, Klingerman D J and McNamee B M 1974 *Fatigue Strength of Steel Beams With Welded Stiffeners and Attachments (NCHRP Report 147)*

[5]   Ngai E W T, Moon K K L, Riggins F J and Yi C Y 2008 RFID research: An academic literature review (1995-2005) and future research directions *Int. J. Prod. Econ.* **112**(2) 510–20. DOI: 10.1016/j.ijpe.2007.05.004.

[6]   Zhang J and Tian G 2014 An evolution of RFID grids for crack detection *Proc., 2014 IEEE Far East Forum on Nondestructive Evaluation/Testing* (Piscataway, New Jersey: Institute of Electrical and Electronics Engineers) pp 358–62. DOI: 10.1109/FENDT.2014.6928296.

[7]   Sadler D J and Ahn C H 2001 On-chip eddy current sensor for proximity sensing and crack detection *Sensors Actuators A Phys.* **91**(3) 340–5. DOI: 10.1016/S0924-4247(01)00605-7.

[8]   Koňár R and Mičian M 2014 Non-destructive testing of welds in gas pipelines repairs with phased array ultrasonic technique *Manuf. Technol.* **14**(1) 42–7

[9]   Tiernan T C and Jarratt R L J 2000 Giant Magnetorestive Sensors and Sensor Arrays for Detection and Imaging of Anomalies in Conductive Materials 1–32

[10]   Zhang Y 2006 In Situ Fatigue Crack Detection using Piezoelectric Paint Sensor *J. Intell. Mater. Syst.*

Struct. **17**(10) 843–52. DOI: 10.1177/1045389X06059957.

[11]   Ihn J and Chang F 2004 Detection and monitoring of hidden fatigue crack growth using a built-in piezoelectric sensor / actuator network : I. Diagnostics *Smart Mater. Struct.* **13** 609–20. DOI: 10.1088/0964-1726/13/3/020.

[12]   Zou L, Bao X, Wan Y and Chen L 2005 Coherent probe-pump-based Brillouin sensor for centimeter-crack detection. *Opt. Lett.* **30**(4) 370–2. DOI: 10.1364/OL.30.000370.

[13]   Chen G, Tang F and Zhou Z 2009 *Coaxial Cable Sensors and Sensing Instrument for Crack Detection in Bridge Structures – Phase I : Field Qualification / Validation Planning (C-06-34)* (Albany, NY)

[14]   Hofer B and Malek S 1988 Crack Detection Arrangement Utilizing Optical Fibres as Reinforcement Fibres 1–4

[15]   Kalansuriya P, Bhattacharyya R and Sarma S 2013 RFID tag antenna-based sensing for pervasive surface crack detection *IEEE Sens. J.* **13**(5) 1564–70. DOI: 10.1109/JSEN.2013.2240155.

[16]   Deshmukh S and Huang H 2010 Wireless interrogation of passive antenna sensors *Meas. Sci. Technol.* **21**(3). DOI: 10.1088/0957-0233/21/3/035201.

[17]   Matsuzaki R and Todoroki A 2006 Wireless detection of internal delamination cracks in CFRP laminates using oscillating frequency changes *Compos. Sci. Technol.* **66**(3-4) 407–16. DOI: 10.1016/j.compscitech.2005.07.016

[18]   Staszewski W J, Lee B C and Traynor R 2007 Fatigue crack detection in metallic structures with Lamb waves and 3D laser vibrometry *Meas. Sci. Technol.* **18**(3) 727–39. DOI: 10.1088/0957-0233/18/3/024.

[19]   Liu H, Bolic M, Nayak A and Stojmenović I 2008 Taxonomy and challenges of the integration of

RFID and wireless sensor networks *IEEE Netw.* **22**(6) 26–32. DOI: 10.1109/MNET.2008.4694171.

[20]   McGovern J B and Randall E A 2001 *Bridge Inspection Manual* (Watertown, Connecticut: Connecticut Department of Transportation)

[21]   Dye Penetrant Testing (DPI). *ECE Global.* www.eceglobal.com/services/inspection-approvals/non-destructive-examiniation-nde/penetrant-testing-pt/ [accessed July 31, 2017].

[22]   Half   cell   potential.   *The   Concrete   Society*.   http://www.concrete.org.uk/fingertips-nuggets.asp?cmd=display&id=443 [accessed July 31, 2017].

[23]   Savage L 2013 Sensing Trouble: Fiber-Optics in Civil Engineering *Opt. Photonics News*

[24]   Wu B, Chen W and Li H 2012 Real-time monitoring of bridge scouring using ultrasonic sensing technology *SPIE 8345, Sensors and Smart Structures Technologies for Civil, Mechanical, and Aerospace Systems* (San Diego, California). DOI: 10.1117/12.914994.

[25]   Carbonation   test.   *Construction   Diagnostic   Centre*. http://www.ndtconcrete.net/index.php?option=com_content&task=view&id=66699&Itemid=48 [accessed July 31, 2017].

[26]   What is RFID? *EPC-RFID Info*. http://www.epc-rfid.info/rfid [accessed June 3, 2016].

[27]   Zhang Q, Crisp M J, Penty R V. and White I H 2015 Reduction of Proximity Effects on UHF Passive RFID Systems by Using Tags with Polarization Diversity *IEEE Trans. Antennas Propag.* **63**(5) 2264–71. DOI: 10.1109/TAP.2015.2403875.

[28]   Dobkin D M 2013 *The RF in RFID: UHF RFID in Practice* (Boston: Newnes)

[29]   Blaber J. DIC Algorithms 2013. http://ncorr.com/index.php/dic-algorithms#1_1 [accessed July 25, 2017].

CHAPTER 9. APPENDIXES

1. Appendix A: Assembly and Mounting of RFID Sensors

The aluminum sample surfaces were cleansed and prepared for the application of epoxy for sensor mounting. To provide a uniform and rough surface for the best adhesion, the sensor mounting area was sandblasted using a Cyclone FT3522 benchtop blast cabinet. An example of the treated surface is shown in Figure 9.1b. Compared to the untreated surface (Figure 9.1a), the sandblasted surface does not reveal the location of the pre-crack line. Therefore, the pre-crack line had to be previously measured and the sensor mounting perimeter had to be marked with a pencil. The resin and hardener should be mixed quickly using a wooden stick in a plastic measuring cup to avoid formation of bubbles and early curing before application (see Figure 9.2).

During initial tests (specifically Samples 1-3), the full interface area for sensor assembly and mounting was covered in 1-mm thick Loctite Epoxy Quick Set adhesive, as in Figure 9.3. After analyzing the results for these samples, it was believed that the adhesive application might be interfering with sensor performance. Adhesive was, henceforth, applied only to the outermost half of the tag antenna patches as shown in Figure 9.4, allowing the central portion of the sensor to move freely with mechanical deformation.
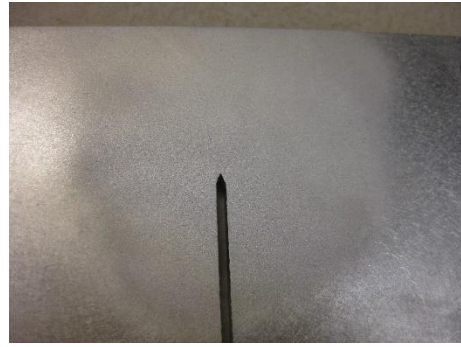
<center>(a)   (b)</center>

Figure 9.1 Sensor mounting surfaces: (a) before sandblasting (sample 1), (b) after sandblasting (sample 3).

<center>Figure 9.2 Consistency of epoxy resin and hardener mix.</center>
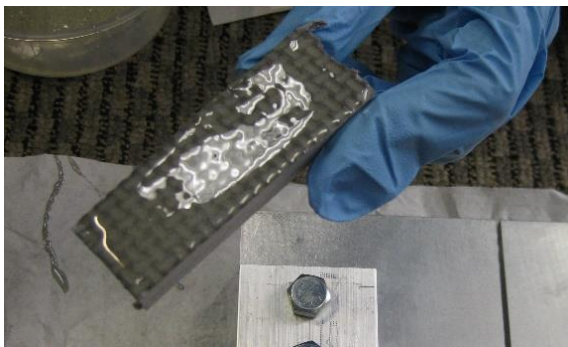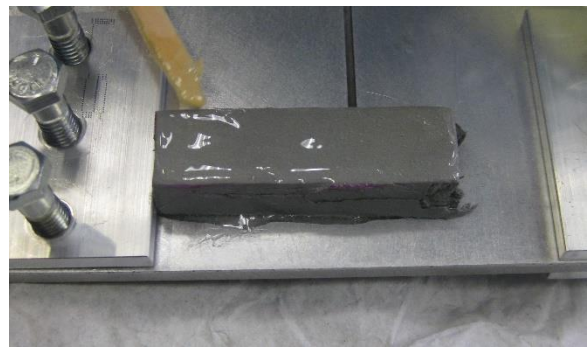
<center>(a)   (b)</center>

Figure 9.3 Full-face adhesive for samples 1-3: (a) sensor mounting, (b) sensor assembly.
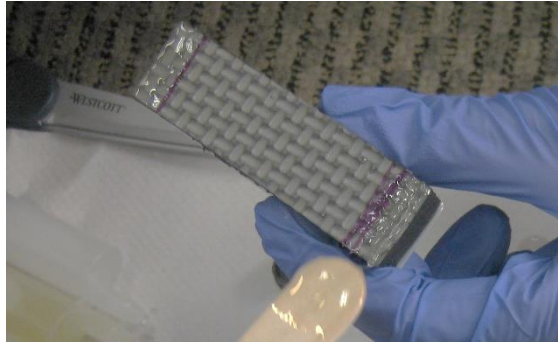
(a)
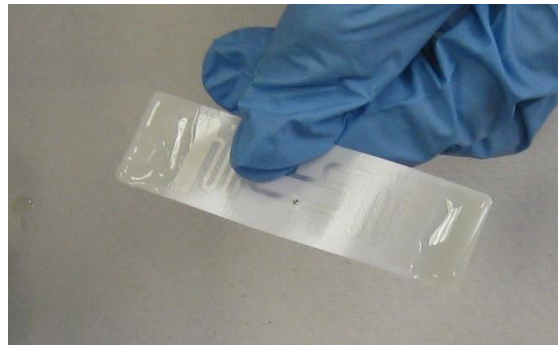
(b)
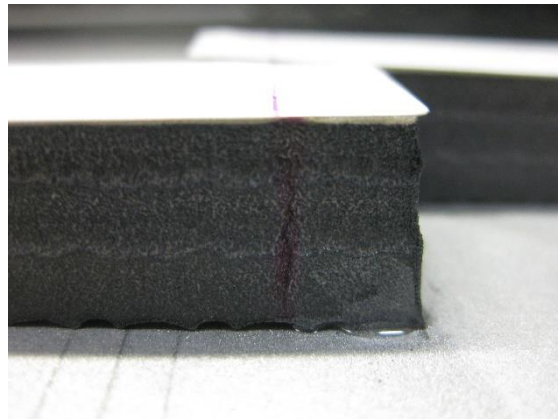
(c)

Figure 9.4 Partial-face adhesive for samples 4 and 1L: (a) sensor mounting, (b) sensor assembly, (c) adhesive thickness in tag T-A of sample 1L.

2. Appendix B: Crack Propagation Test Photos

a. Equipment and Setup

The photos shown below document the equipment and setup used during crack propagation experiments. Figure 9.5 shows the hydraulic universal test machine used during crack propagation testing. The different surfaces of the EVA foam substrate used to assemble the crack sensor are shown in Figure 9.6. Different views of the experimental setup for the different crack propagation tests are shown in Figure 9.7.

Figure 9.5 ADMET eXpert1655 uniaxial testing machine.

(a)   (b)   (c)
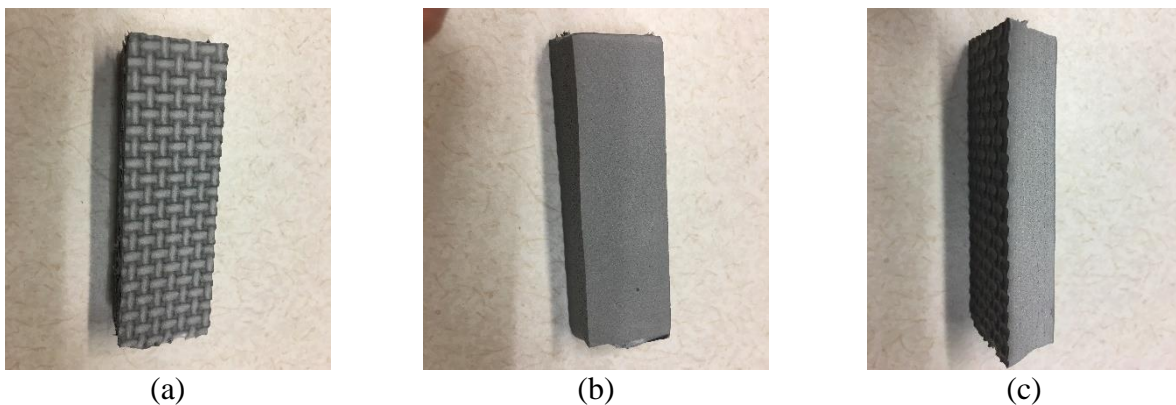
Figure 9.6 Typical EVA rubber substrate with approximate dimensions 0.86 in x 2.91in x 0.5 in: (a) face attached to sample, (b) face assembled to RFID tag, (c) side view.
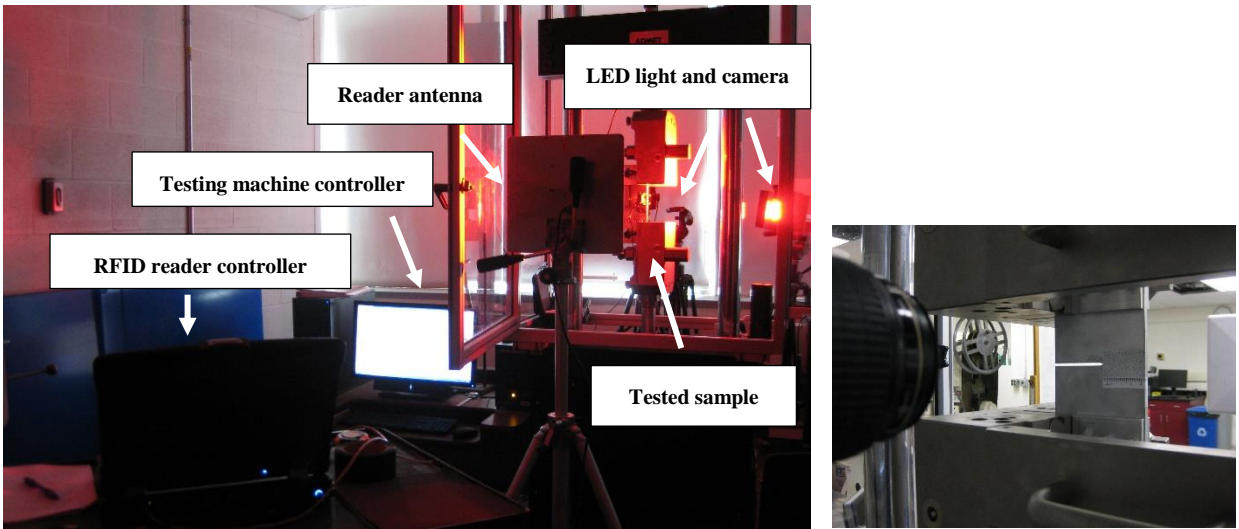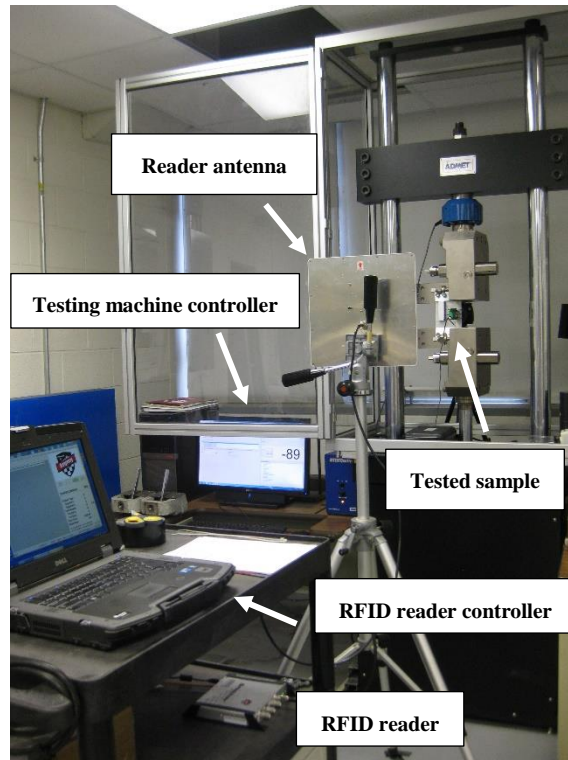
Figure 9.7 Experimental setup: (a) taking images for DIC, (b) view from camera for DIC photos, (c) without taking images for DIC.

b. Pre-Cracking and Speckle Pattern Preparation

The photos shown in this section document the preparation of the specimen for crack propagation testing. Figure 9.8 shows the stages of creating the speckle pattern to be used for DIC. Figure 9.9 shows the specimen undergoing the pre-crack formation and a close-up after pre-cracking.

(a)

(b)

(c)

(d)
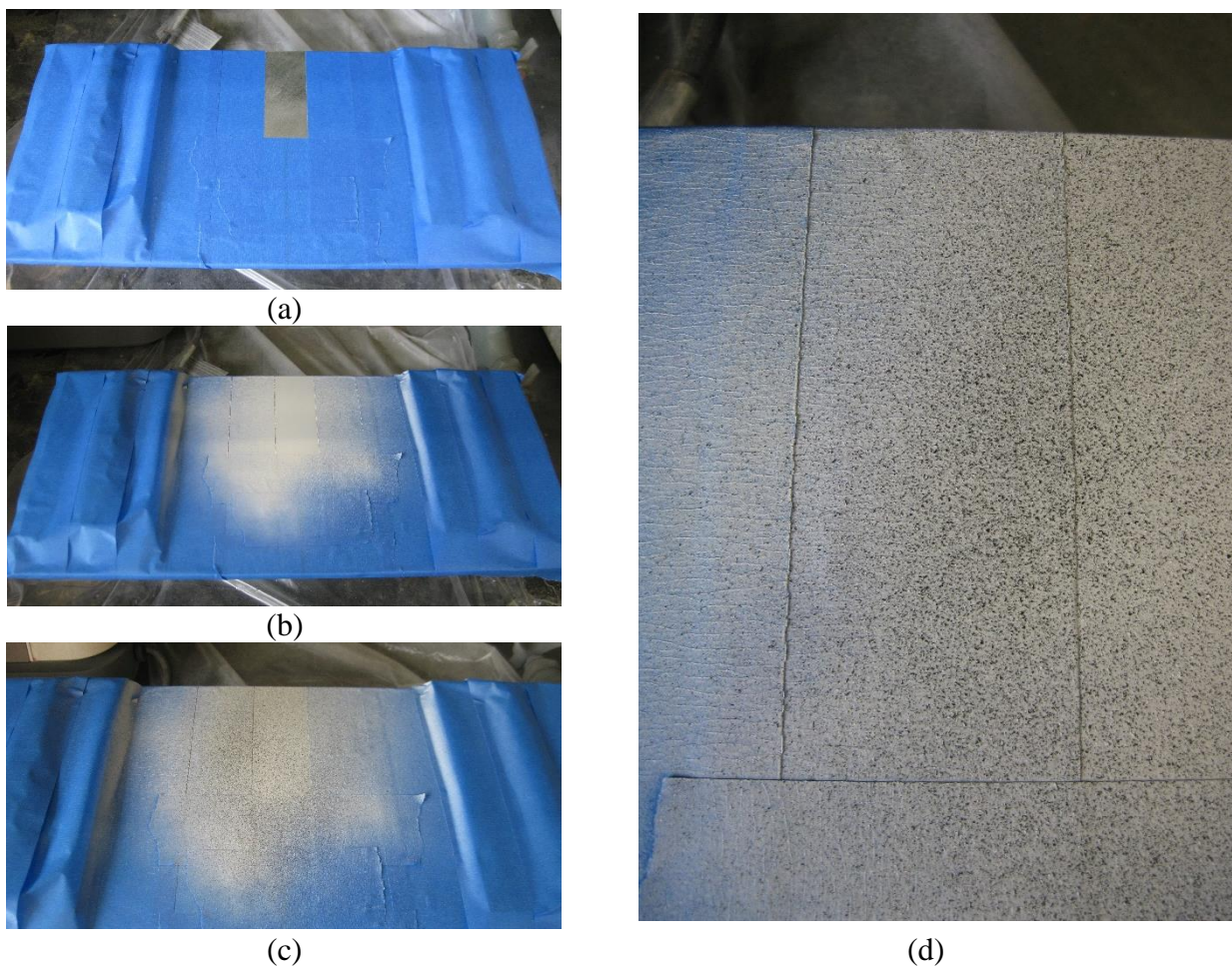
Figure 9.8 Speckle pattern application on sample 1L: (a) sample is covered in masking tape and only the area where crack propagation will occur is left showing, (b) white primer is spray painted, (c) charcoal-colored texture spray paint is applied, (d) close-up of finished speckle pattern.
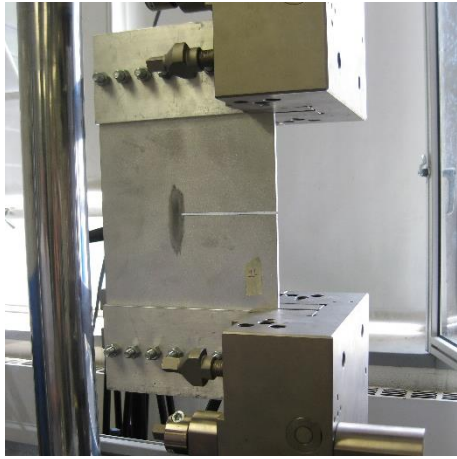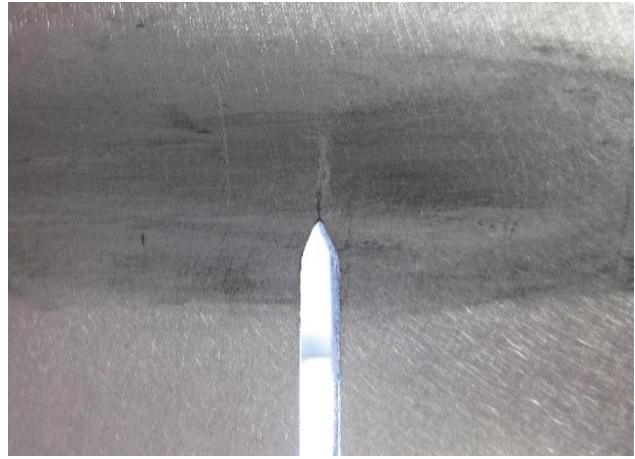
(a)	(b)

Figure 9.9 Pre-cracking of sample 1L: (a) setup, (b) pre-crack line.

c. RFID Sensor Orientation
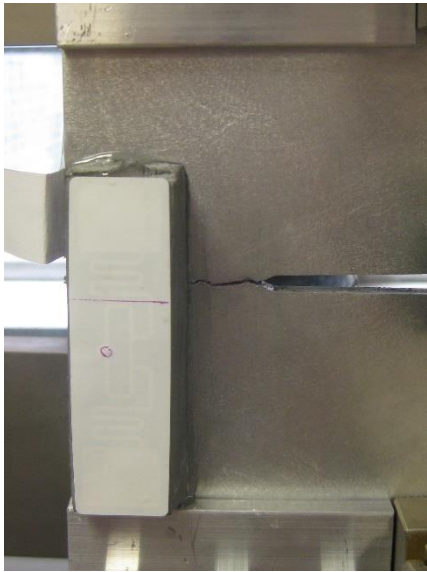
(a) (b) (c)
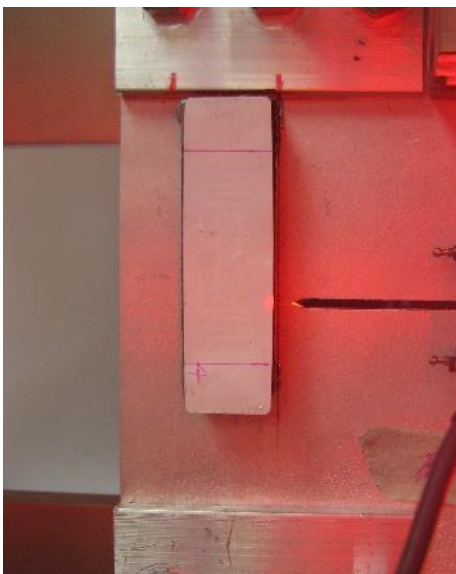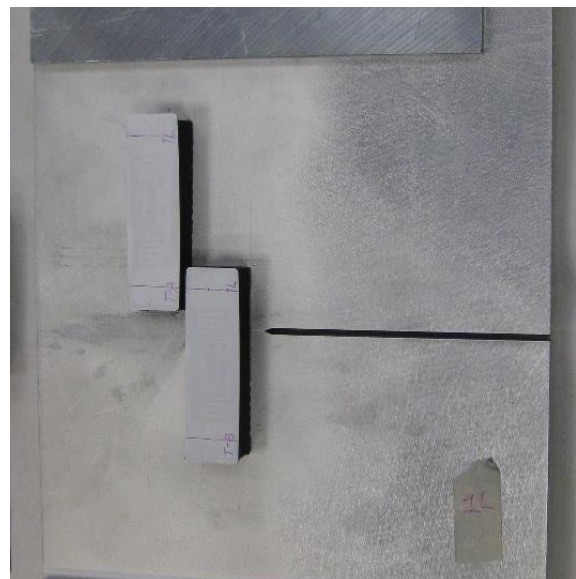
(d) (e)

Figure 9.10 Sensor orientations per sample: (a) sample 1, (b) sample 2, (c) sample 3, sample 4, (e) sample 1L.

d. Sample Breakage

In this section, different angles of the failed specimens for samples 1, 2, 4, and 1L are shown in Figure 9.11, Figure 9.12, Figure 9.13, and Figure 9.14, respectively.
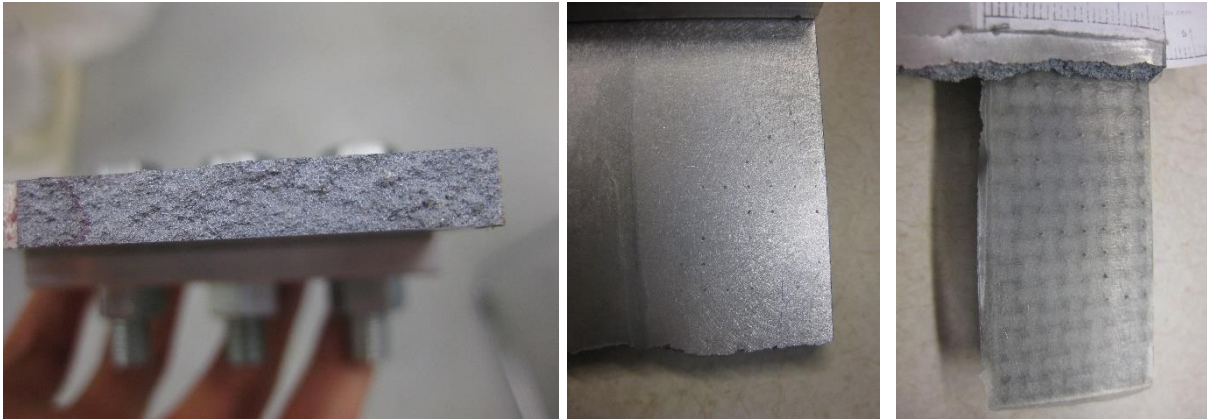
Figure 9.11 Breakage of sample 1.
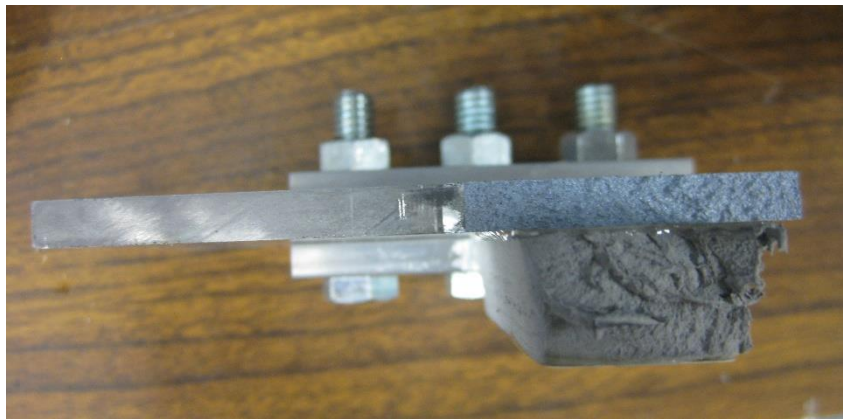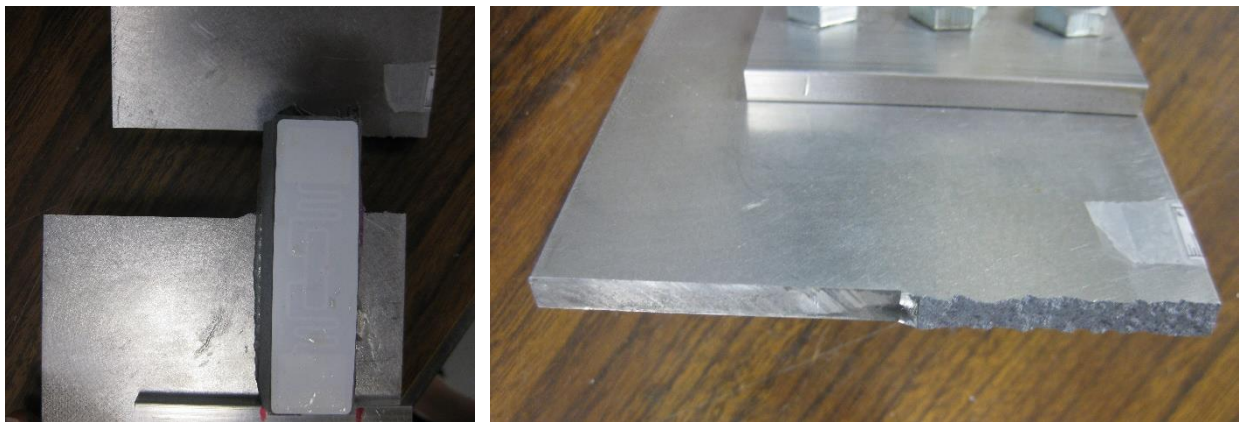
Figure 9.12 Breakage of sample 2.
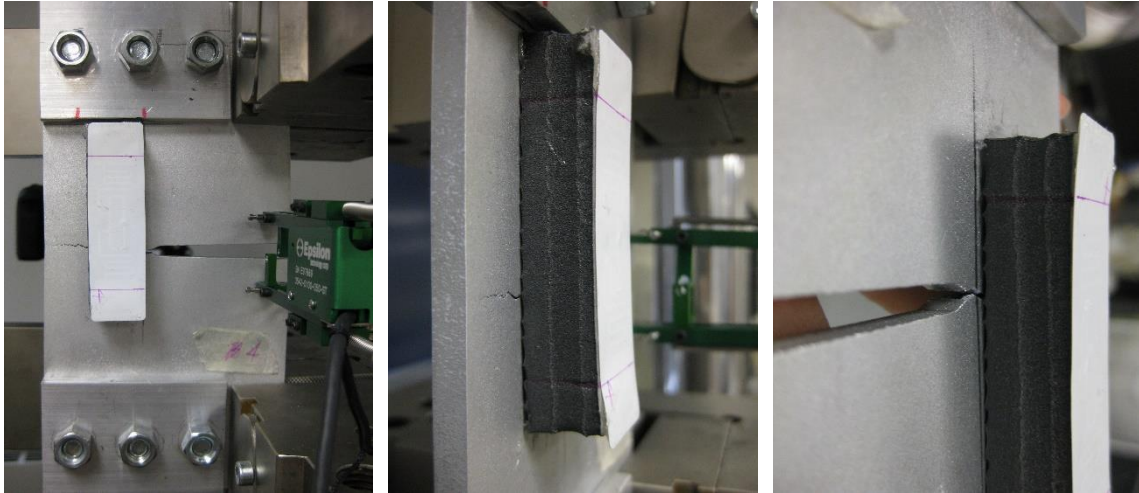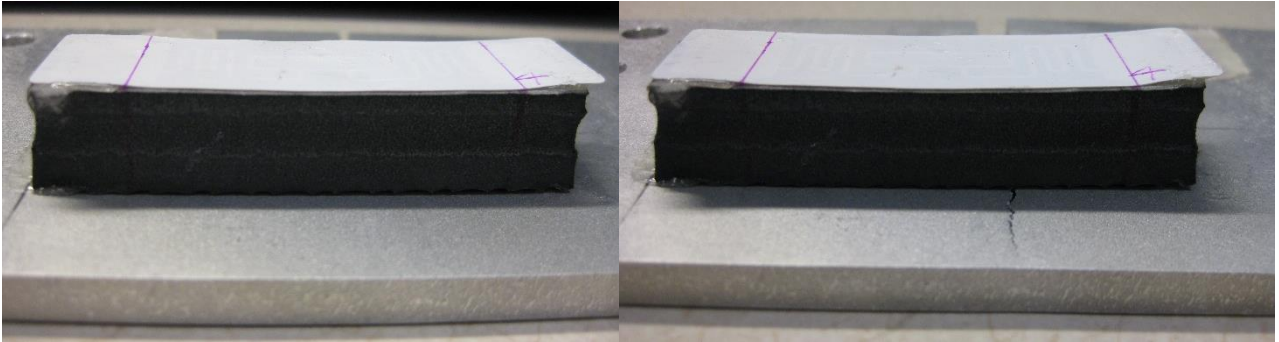
Figure 9.13 Breakage of sample 4.
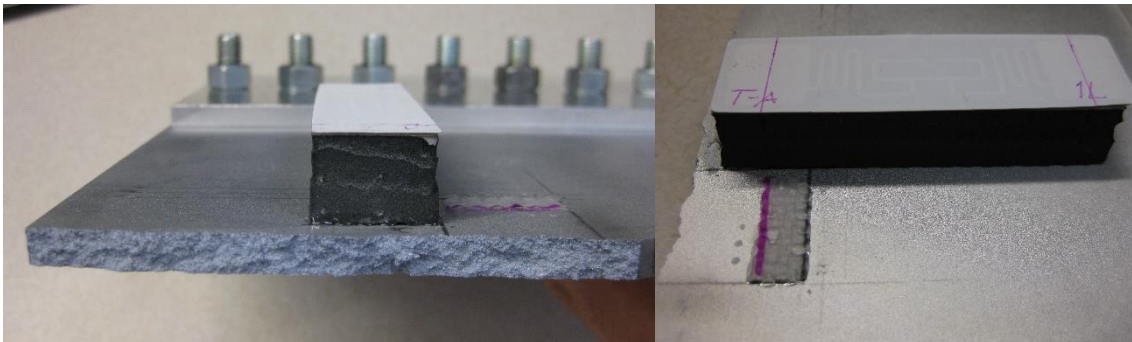
Figure 9.14 Breakage of sample 1L.

3. Appendix C: Specimen Notch Design Calculations and Material Properties

a. Notch Dimension Calculations

The dimensions and configuration of the specimen notches used in this project were determined by consulting the guidelines in ASTM E399-12: Standard Test Method for Linear-Elastic Plane-Strain Fracture Toughness K_{IC} of Metallic Materials, Section 7.2: Specimen Configurations and Section 7.3: Specimen Preparation. In order to determine the notch length a, the standard recommends using the following expression:

$$0.45W \leq a \leq 0.55W \qquad\qquad\qquad C.1$$

where W is the width of the specimen from the action line of the applied force to the edge (3.5 in for the small sample and 7.5 in for the large sample). To ensure slow crack propagation, a ratio of a/W of 0.64 was chosen for the small sample and 0.57 for the large sample. Thus, the notch lengths for the small and large sample were 2.25 in and 4.25 in, respectively.

The notch width N, was recommended to fall within the following range:

$$\frac{1}{16}in < N < \frac{W}{10} \qquad\qquad\qquad C.2$$

The upper bound of this relationship in the small and large plates was 0.35 in and 0.75 in, respectively. The machine used to fabricate the notch left a gap 3/32 in wide, so this was the notch width that was used for small and large specimens.

The standard recommends making a fatigue crack starter notch to produce nearly straight crack propagation. The size of pre-crack would be the greater of 0.05 or $0.025W$ for a straight through notch such as the one used in these experiments. For the small sample, the pre-crack size was 0.0875 in and, for the large sample, 0.1875 in.

b. Material Properties

The material properties of the plate and anti-buckling plates of all crack propagation testing samples are shown in Table 9.1.

Table 9.1 Material properties of specimens.

Material	Part	Yield Strength (ksi)	Young's Modulus (ksi)	Hardness Rating	Elongation (%)
Highly Machinable MIC6 Aluminum	Test plates	15	10,000	Soft (Brinell 65)	3
6061 Aluminum	Anti-buckling plates	35	10,000	Soft (Brinell 95)	12.5

4. Appendix D: Crack Propagation Photos, DIC Parameters, and Strain and Displacement Fields

a. Crack Propagation Photos

(a)

(b)

(c)

(d)

(e)
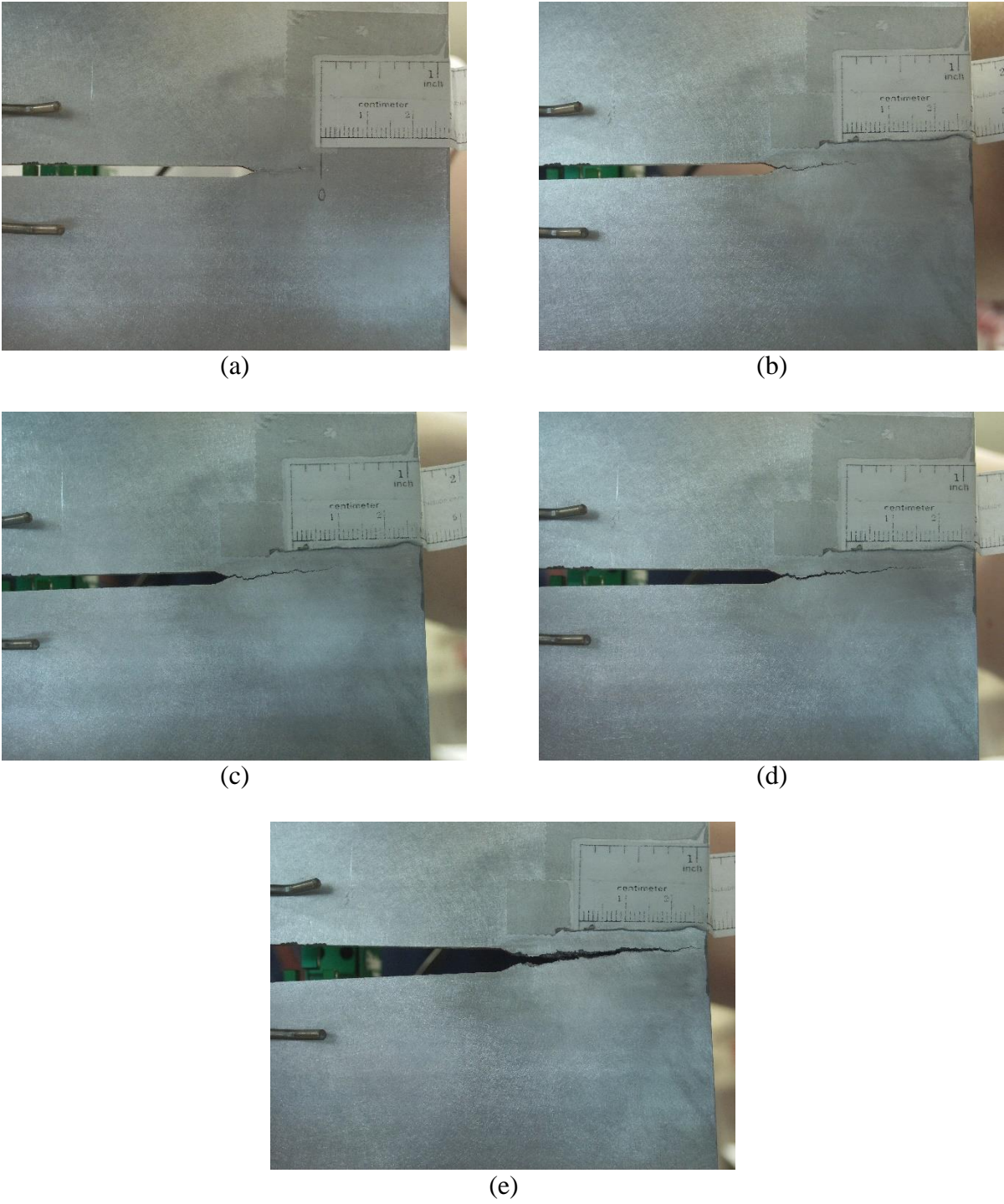
Figure 9.15 Crack propagation photos of sample 1: crack length: (a) 1.5 mm, (b) 3.5 mm, (c) 12.0 mm, (d) 18.5 mm, (e) 27.0 mm.
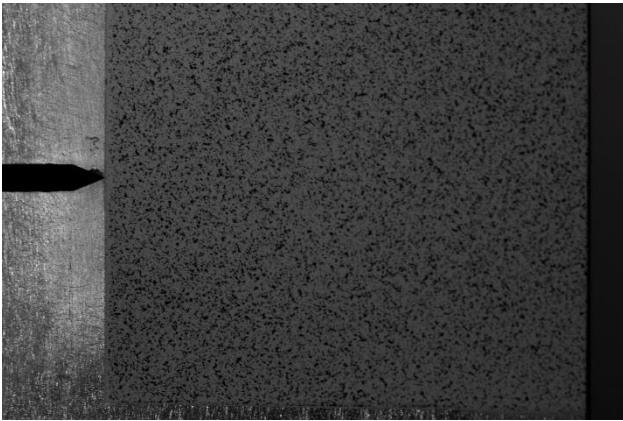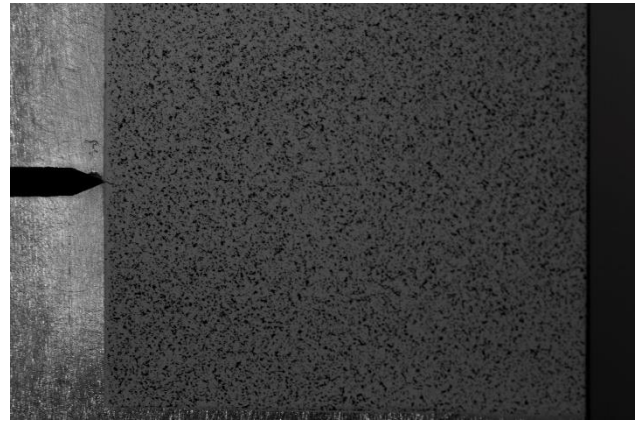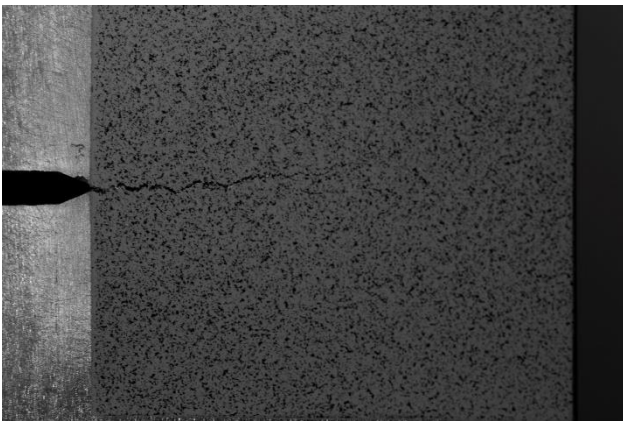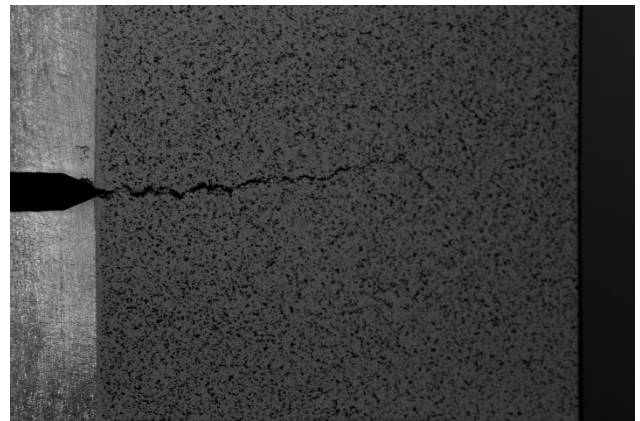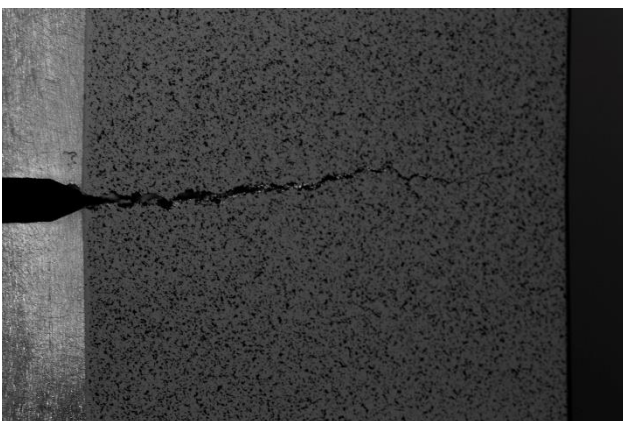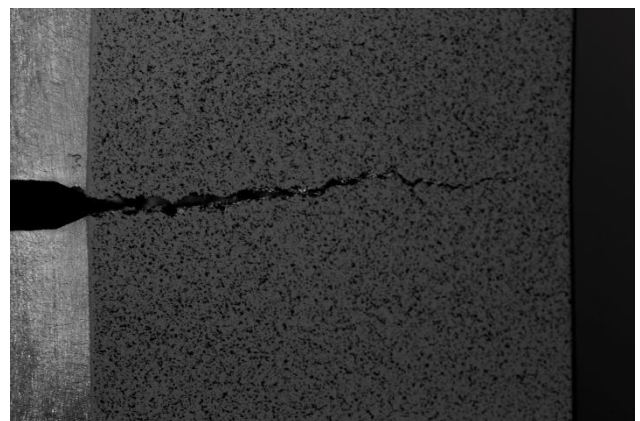
Figure 9.16 Crack propagation photos for DIC of sample 4: frame (a) 4, (b) 10, (c) 16, (d) 22, (e) 30, (f) 41.

(a)

(b)

(c)   (d)
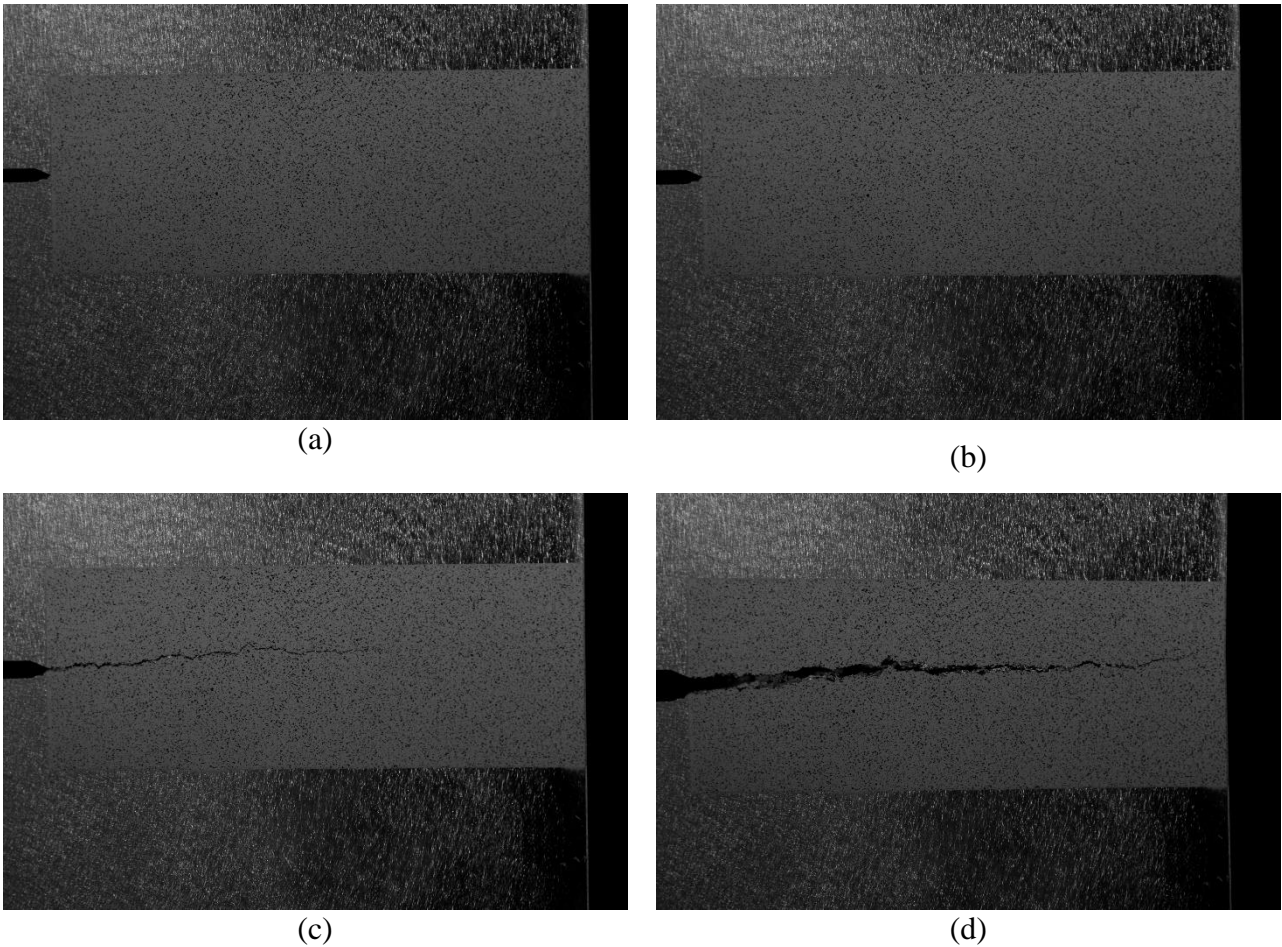
Figure 9.17 Crack propagation photos for DIC of sample 1L: frame (a) 2, (b) 4, (c) 7, (d) 22.

b. DIC Analysis Procedure

In order to carry out a DIC analysis, a reference image is selected along with a group of current images. The reference image is the image of the undisturbed speckle-pattern. For Samples 4 and 1L, the number of current images correspond to the number of steps in the test procedure: 41 for Sample 4 and, 22 for Sample 1L. The region of interest (ROI) is the area of the speckle-pattern, where the analysis will be carried out and the subsets will be traced from the reference image. Figure 9.18 shows the ROI for Samples 4 and 1L.
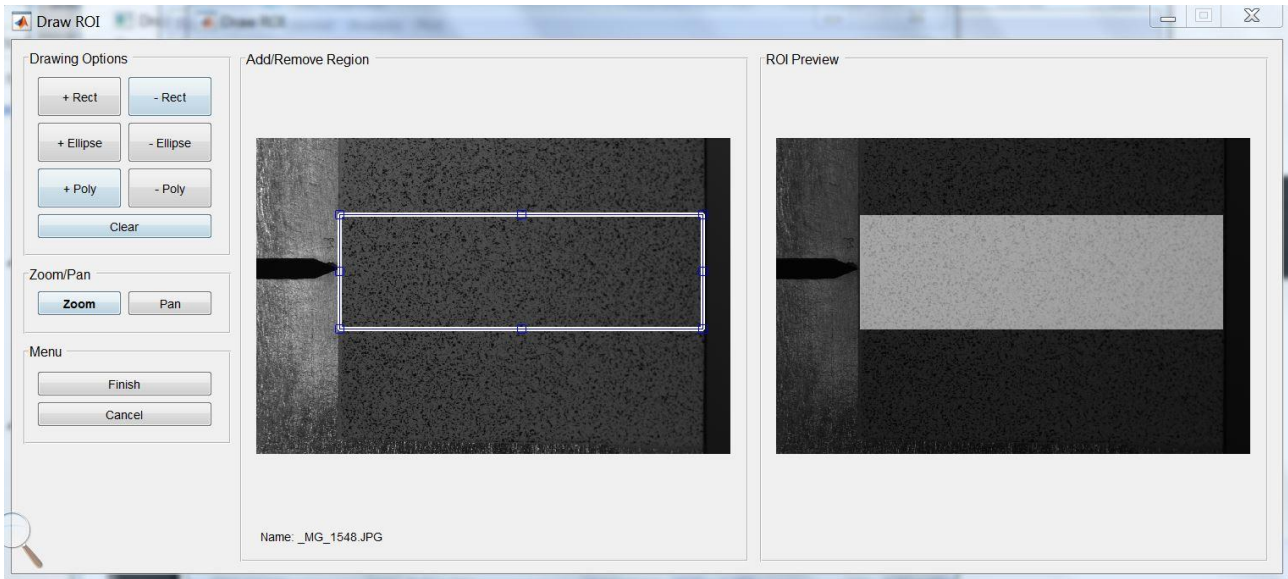
(a)
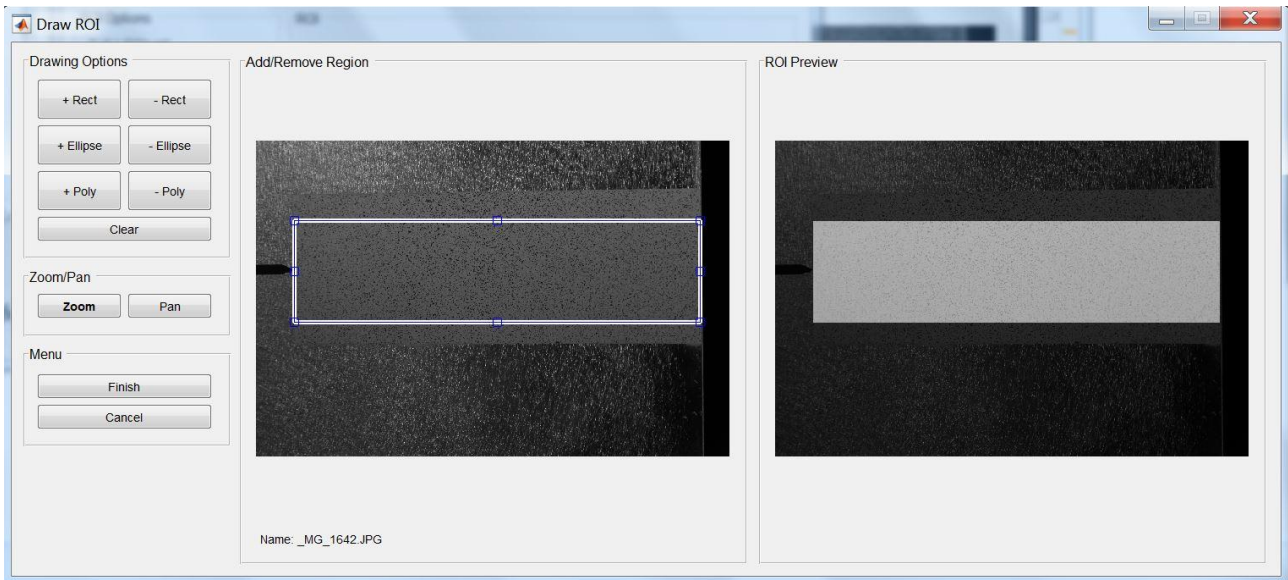
(b)

Figure 9.18 Region of interest for (a) sample 4, (b) sample 1L.

The DIC parameters consist of subset radius and subset spacing. Subset radius refers to the size of the subsets that will be traced on the current images based on the subsets found on the reference image. Subset radius should be as small as possible without producing noisy displacement data. Subset spacing produces a smoother field when it is smaller, but when it is larger, reduces computational costs. The subset radius for both samples was 20, while the subset spacing for the

small and large samples were 2 and 3, respectively. Figure 9.19 shows the subset preview for both

samples with the parameters selected.
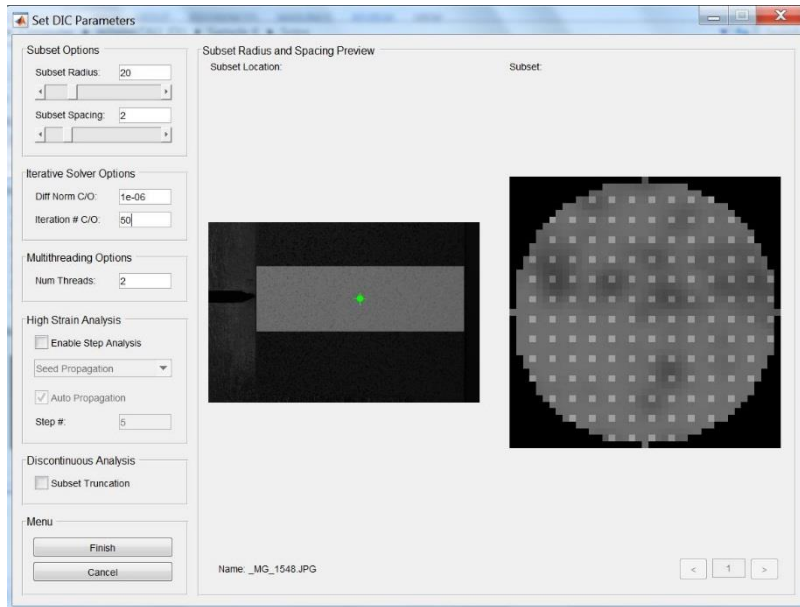
(a)
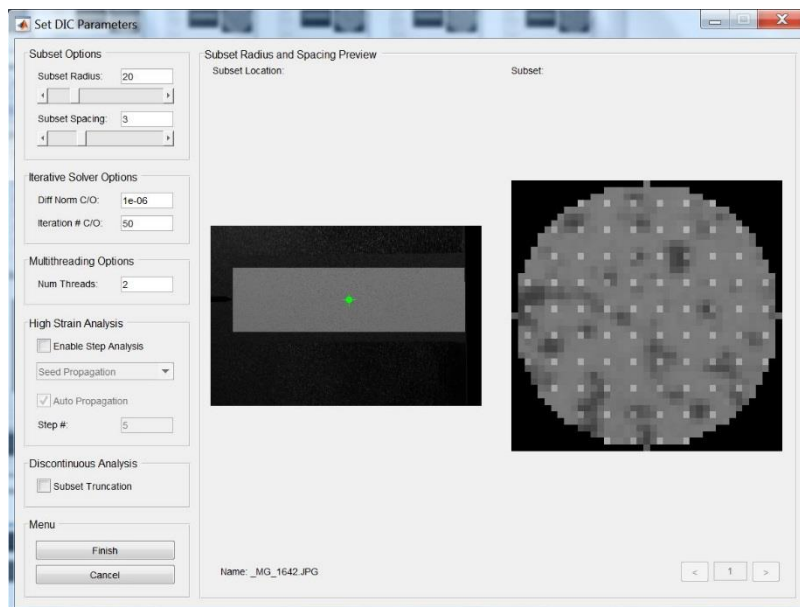
(b)

Figure 9.19 Subset preview for (a) sample 4, (b) sample 1L.

Since the computer utilized for the analysis has multiple computational cores, two cores were chosen to accelerate computation and to provide a smooth analysis without losing data on the displacement maps. As a result, two seeds were symmetrically placed for the analysis in high-deformation regions (see Figure 9.20).
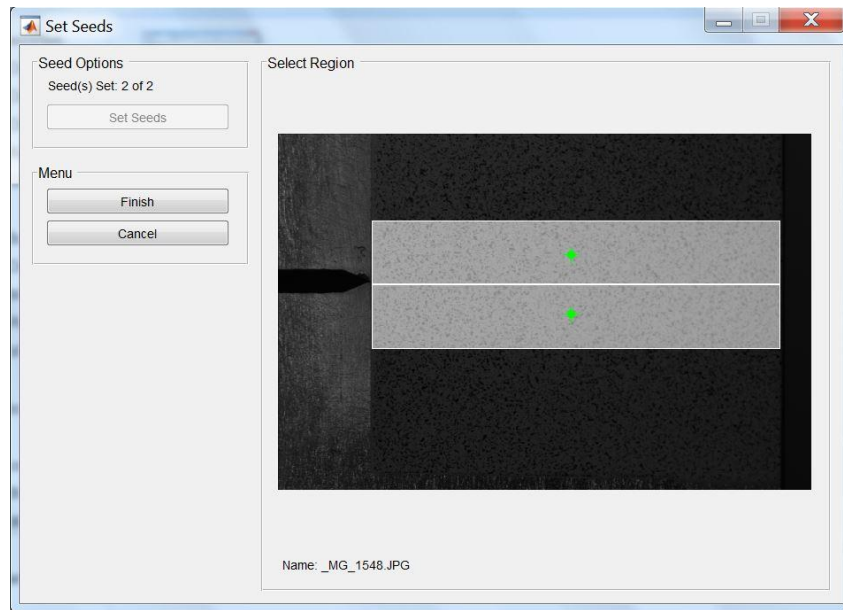
(a)
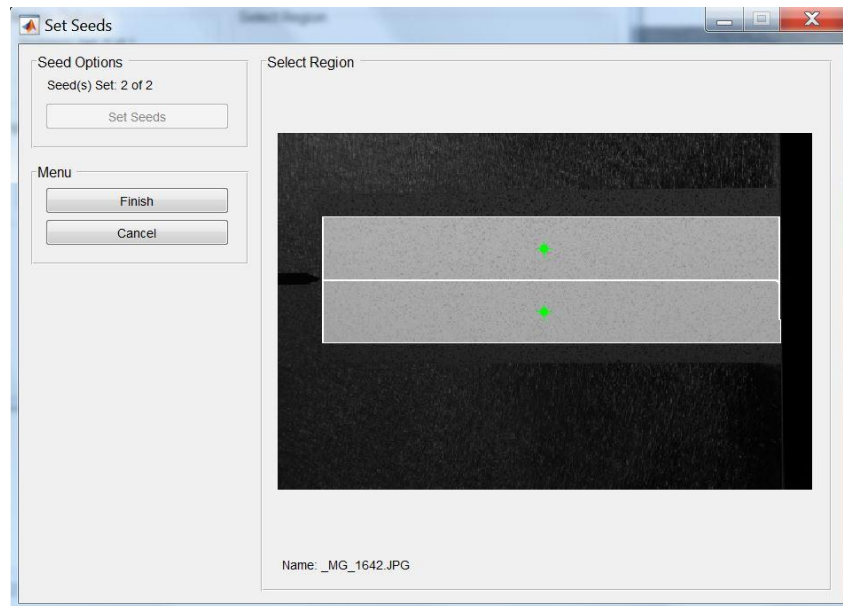
(b)

Figure 9.20 Seed placement in (a) sample 4, (b) sample 1L.

The seeds are processed and a seed preview is shown. The preview shows the correlation coefficient and the number of iterations for the solution to converge. The lower these numbers are, the better the seed analysis is. Table 9.2 shows the most critical values for correlation coefficient and number of iterations in the analysis. Figure 9.21 shows examples of the seed previews for Samples 4 and 1L.
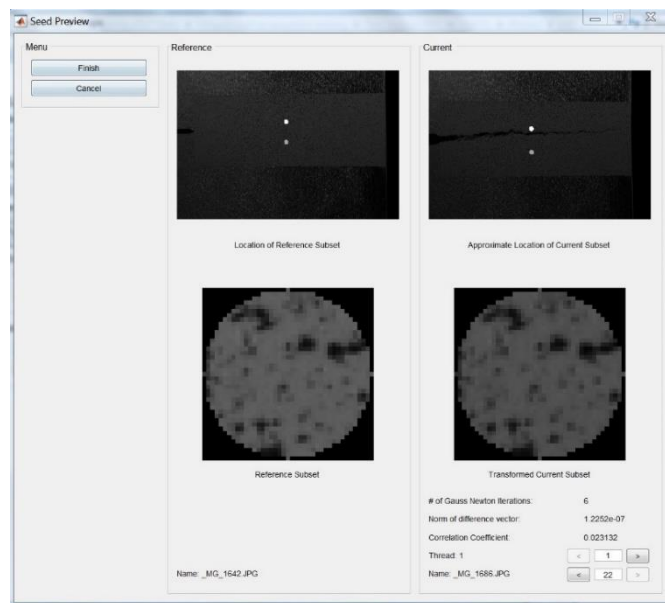
(a)
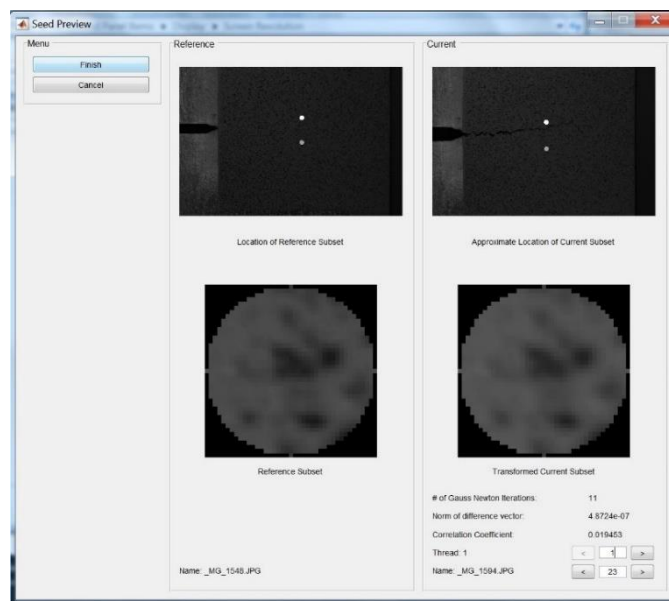
(b)

Figure 9.21 Seed preview of (a) sample 4, (b) sample 1L.

Table 9.2 Critical values for seed previews.

Sample	Seed	Maximum no. of iterations	Maximum correlation coefficient
4	1	11 [i]	0.019453 [ii]
	2	10 [iii]	0.011817 [iii]
1L	1	9 [iv]	0.041311 [iv]
	2	8 [iv]	0.034474 [iv]

[i] Frames 1, 5, 12, 18, 23, 27, 29, 30, 31, 39, [ii] Frame 23, [iii] Frame 33, [iv] Frame 4

After this, DIC analysis was performed. When the analysis was finished, displacement fields were generated. The correlation coefficient for displacement calculation (a different variable) can be cut off at this point. This ensures that areas where subsets had changed dramatically (namely, in the immediate vicinity of the crack region), could be eliminated. The cutoff for Sample 4 was 0.25 and, for Sample 1L, it was 0.6984. These cutoff values were applied to all frames. The unit conversion is also determined at this point by loading a calibration image and drawing a line of known length. In this case, this was the length of total crack propagation. Figure 9.22 shows the window for displacement formatting.
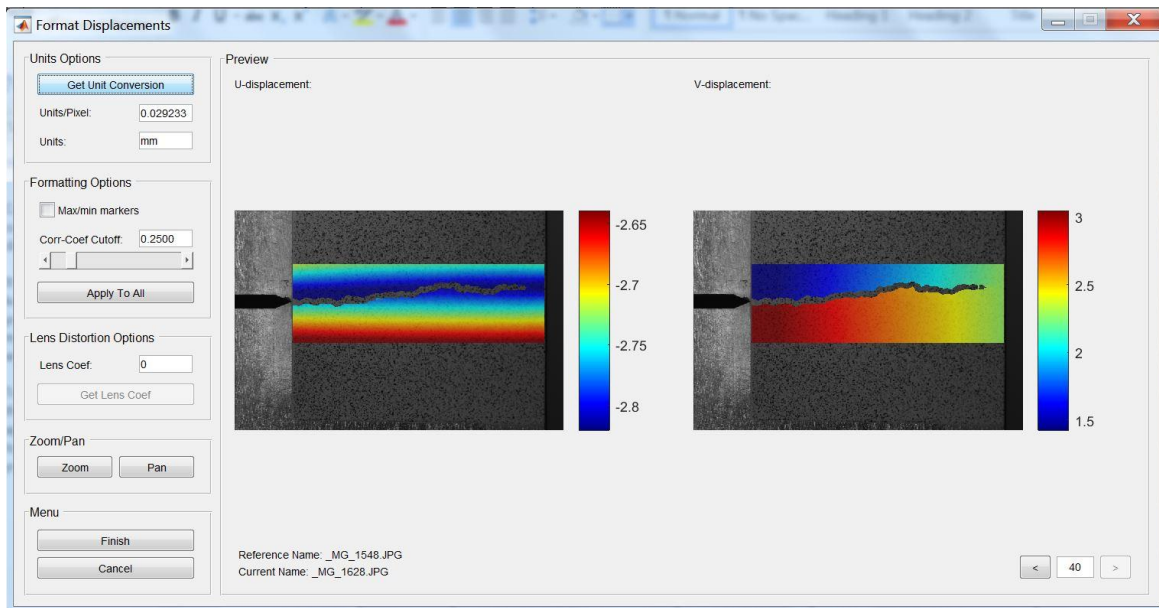
(a)
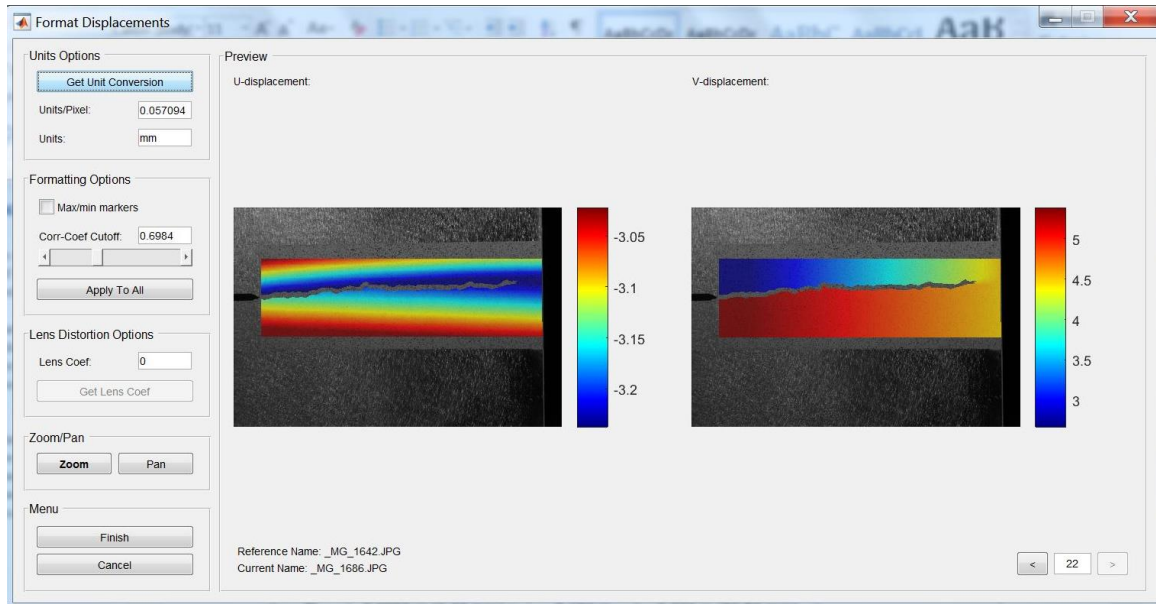
(b)

Figure 9.22 Format displacements window for (a) sample 4, (b) sample 1L.

The principal parameter for strain analysis is the strain radius. This determines the size of a subset that will be simplified to a spatial plane. The key of the strain radius is that it should be sufficiently small so that the displacement data points are as close to the plane as possible, while not resulting in noisy strain data. The strain radius chosen, for both samples, was 5. Figure 9.23 shows the plane approximations for the strain radius selected. After this, strain analysis is completed.
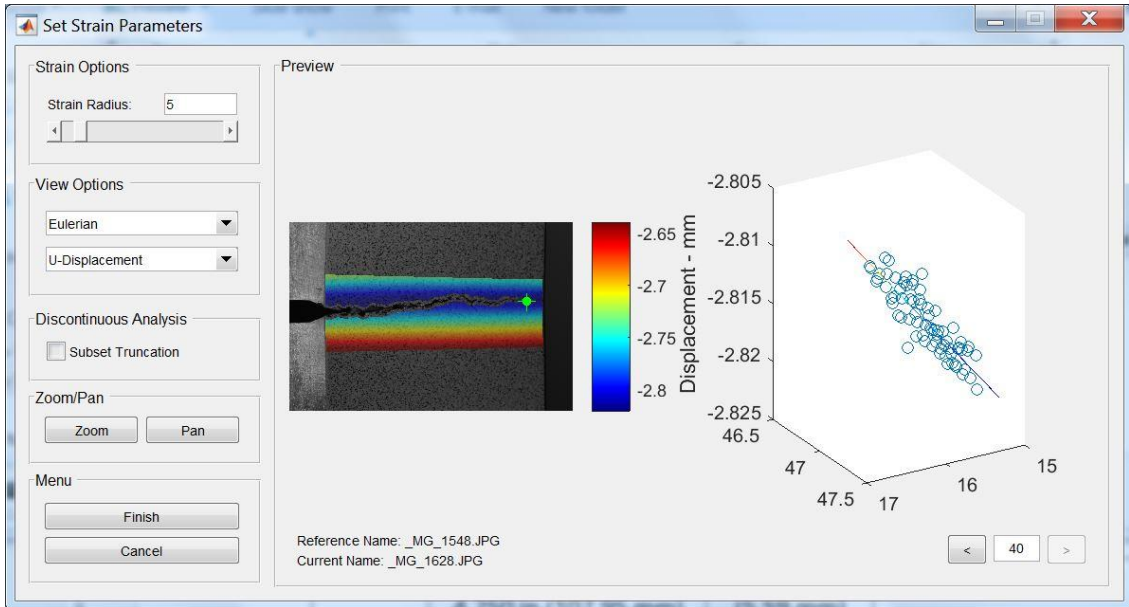
(a)
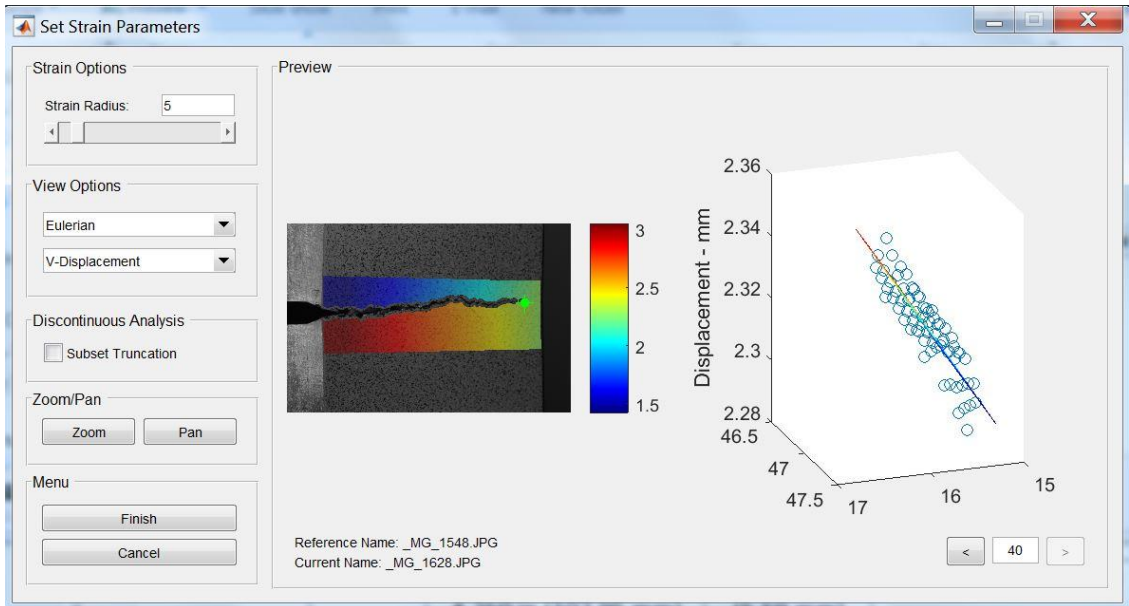
(b)

Figure 9.23 Strain parameters for (a) horizontal displacement in sample 4, (b) vertical displacement in sample 4, (c) horizontal displacement in sample 1L, (d) vertical displacement in sample 1L.
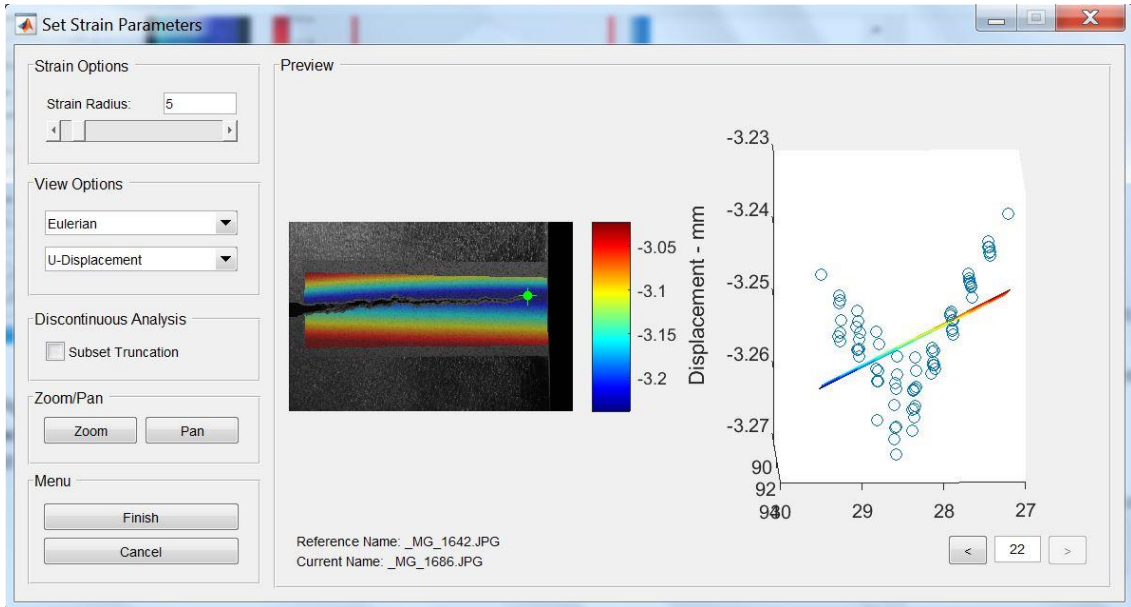
(c)
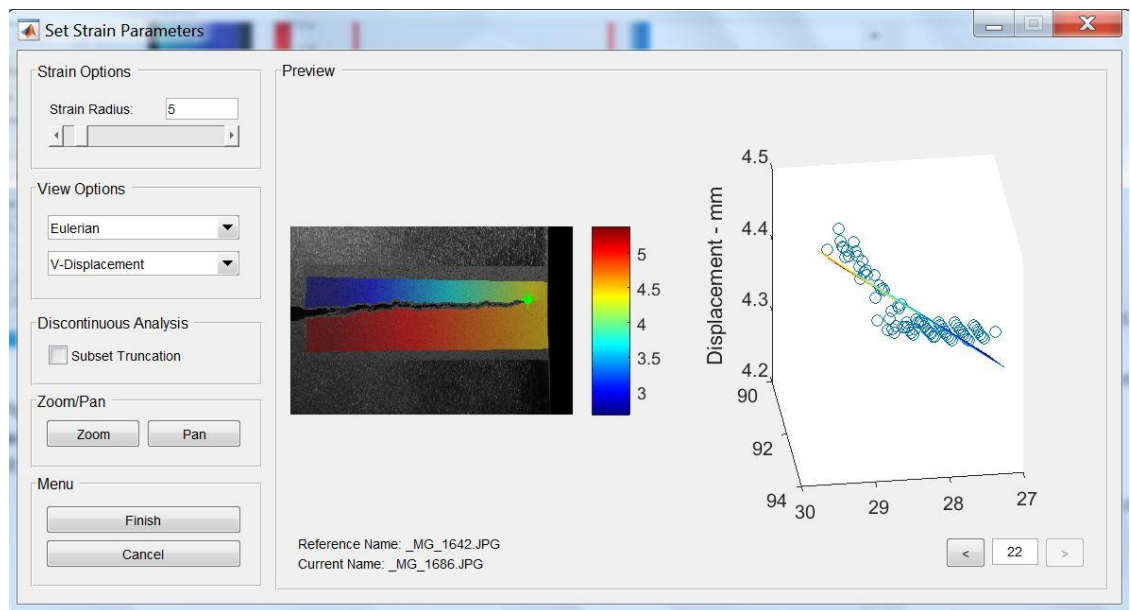
(d)

Figure 9.23. Strain parameters for (a) horizontal displacement in sample 4, (b) vertical displacement in sample 4, (c) horizontal displacement in sample 1L, (d) vertical displacement in sample 1L (continued).

c. Strain and Displacement Fields

Figures Figure 9.24Figure 9.25Figure 9.26, Figure 9.27, Figure 9.28, Figure 9.29 show selections of the vertical strain (ε_{yy}) and horizontal (U) and vertical (V) displacement fields calculated for samples 4 and 1L.

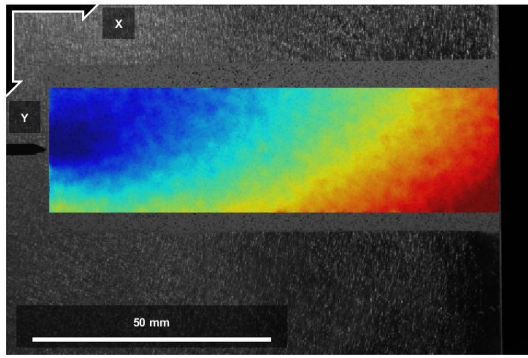(a)   (b)

(c)   (d)

(e)   (f)
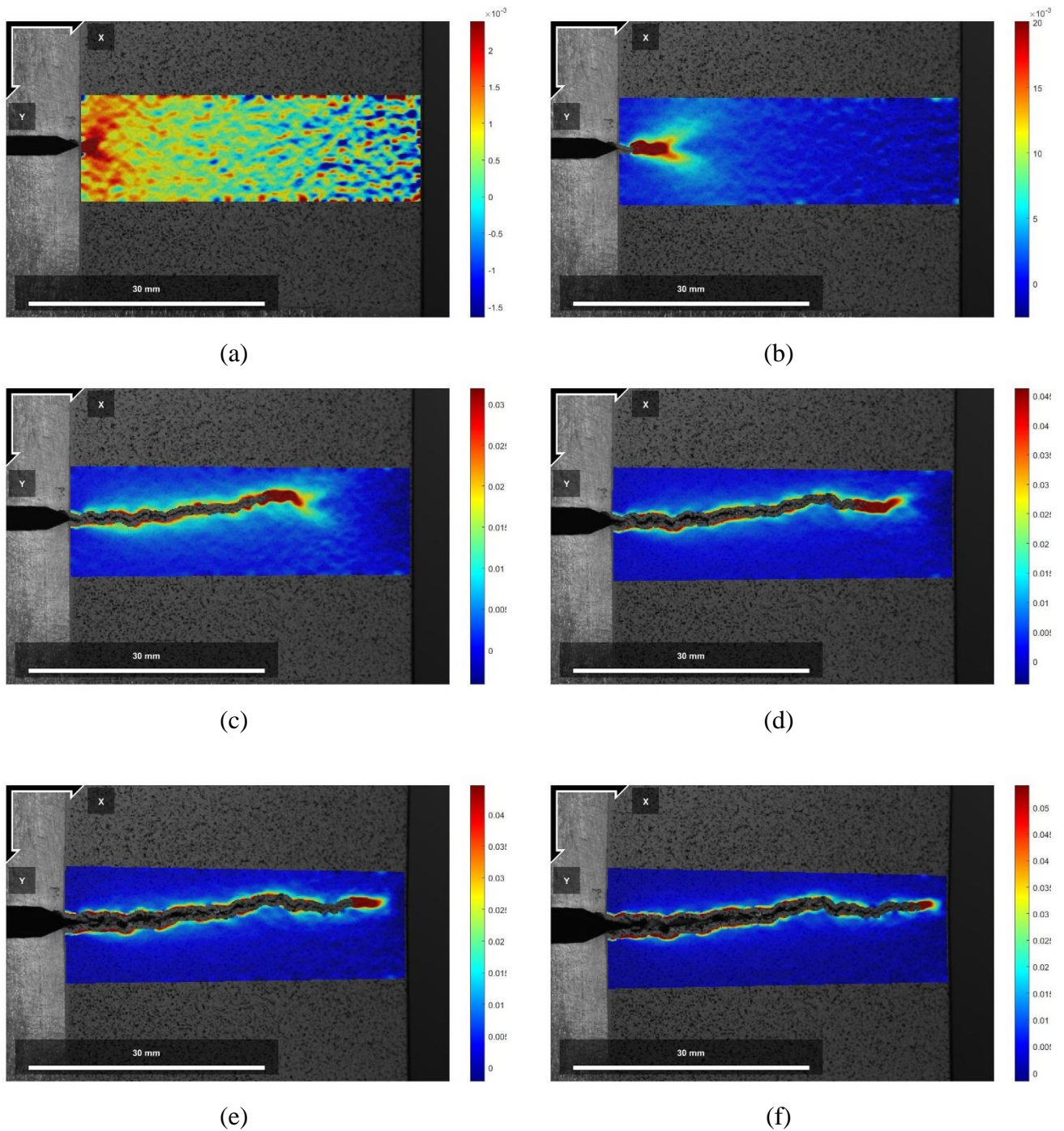
Figure 9.24 Vertical strain field (ε_{yy}) for sample 4: frame: (a) 4, (b) 10, (c) 16, (d) 22, (e) 30, (f) 40.

(a)

(b)

(c)

(d)

(e)

(f)
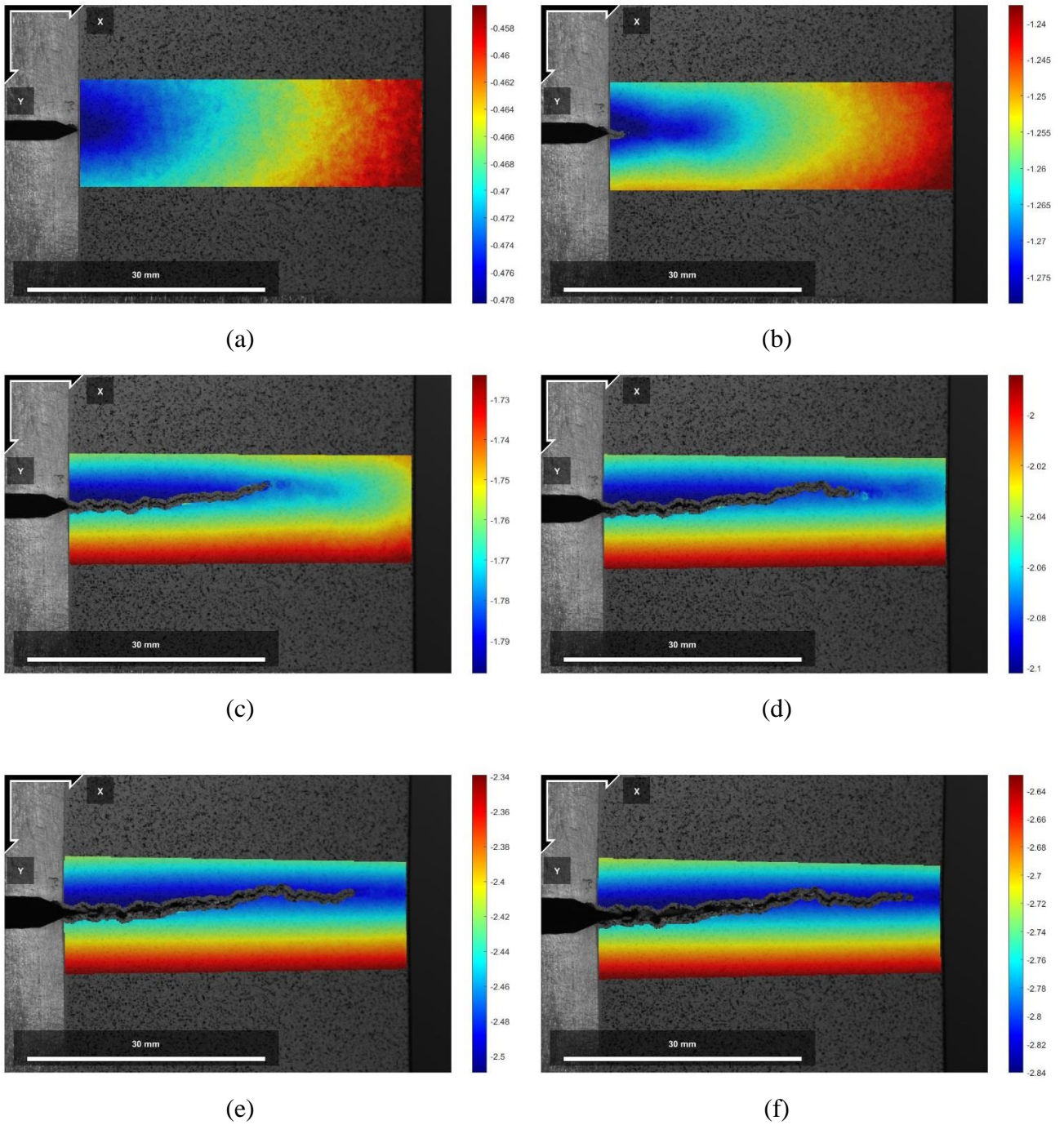
Figure 9.25 Horizontal (U) displacement field for sample 4: frame: (a) 4, (b) 10, (c) 16, (d) 22, (e) 30, (f) 40.

(a)

(b)

(c)

(d)

(e)

(f)
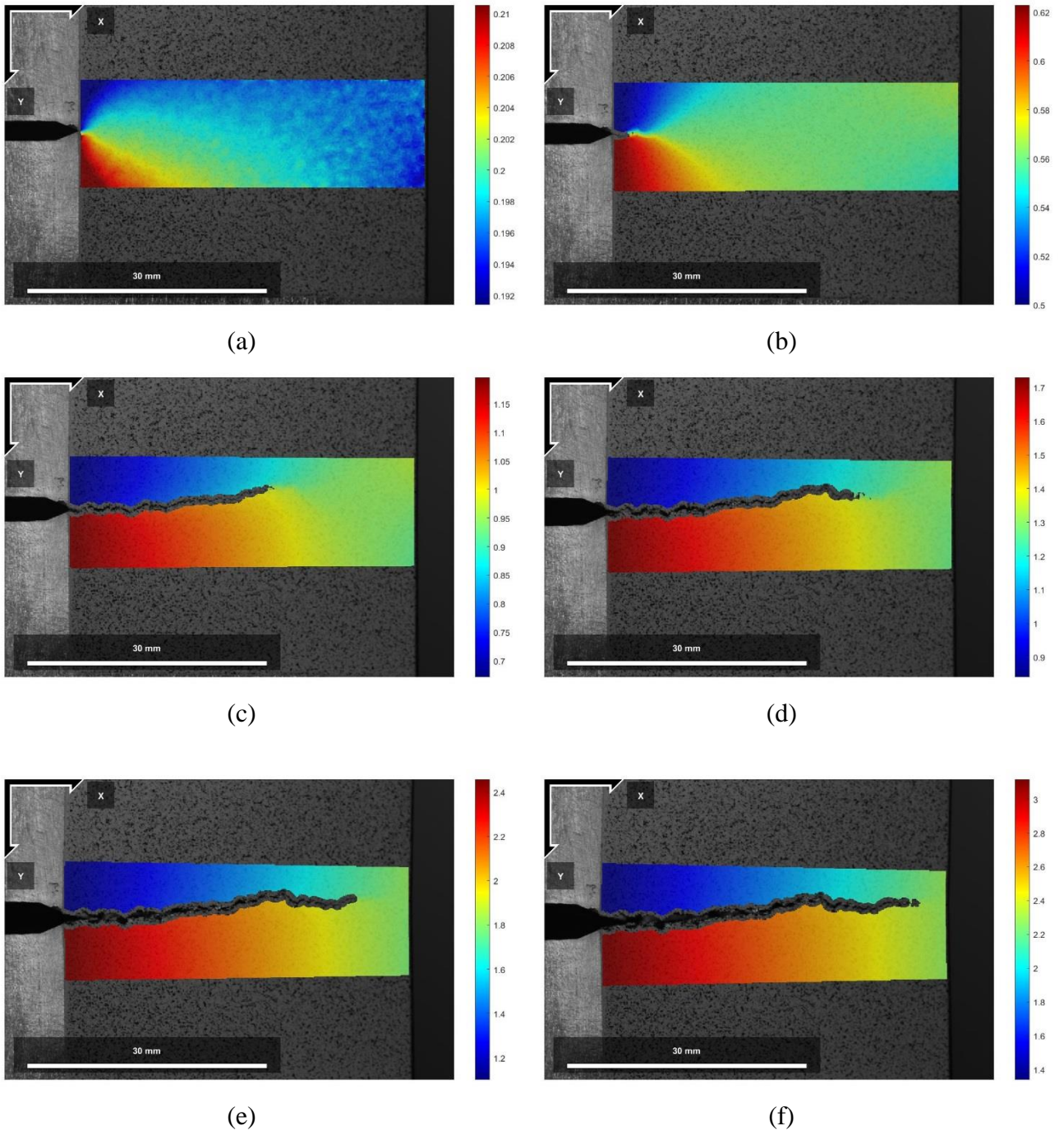
Figure 9.26 Vertical (V) displacement field for sample 4: frame: (a) 4, (b) 10, (c) 16, (d) 22, (e) 30, (f) 40.
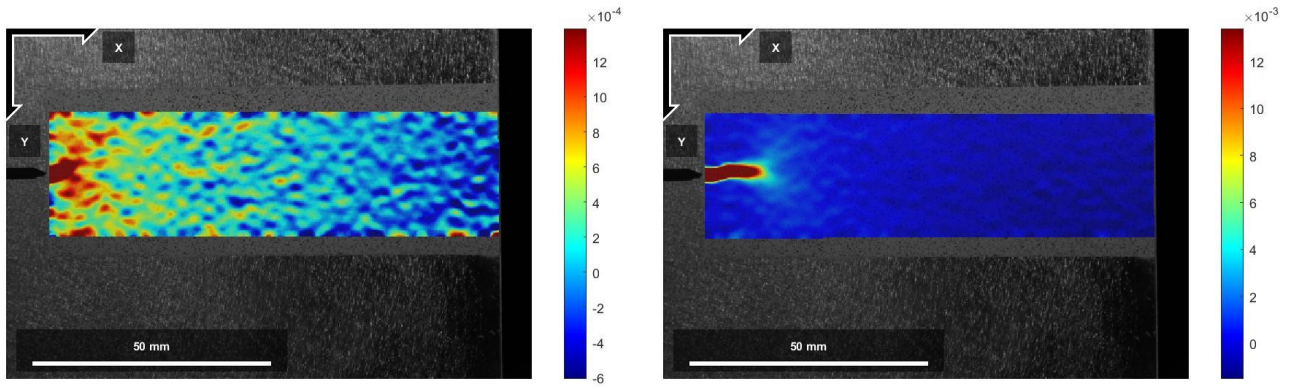
(a)

(b)
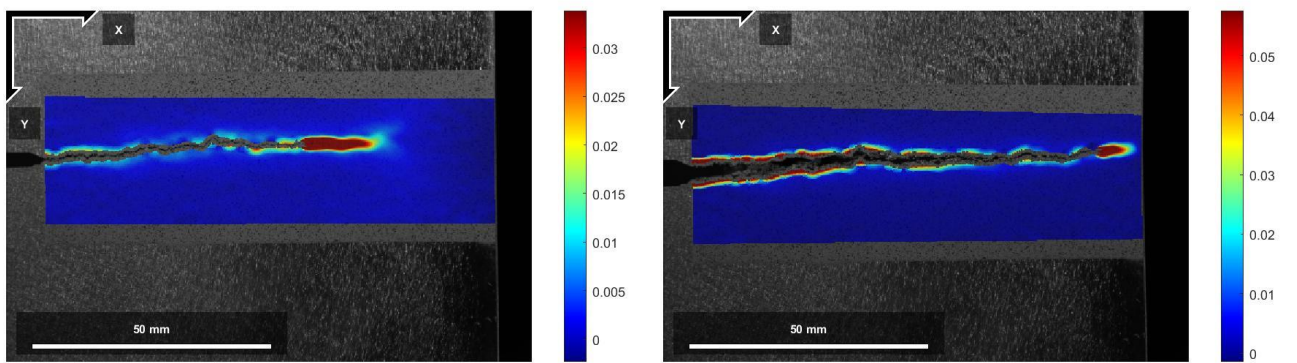
(c)

(d)

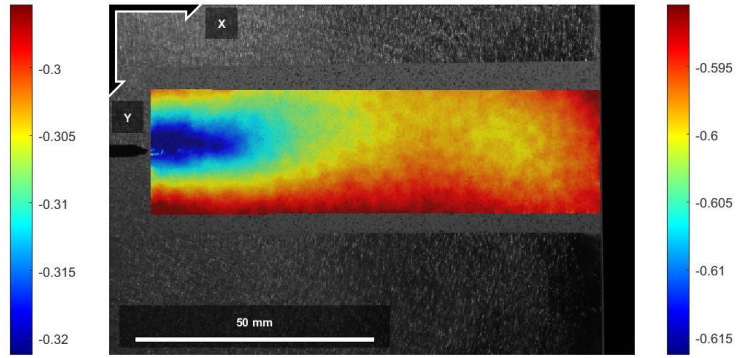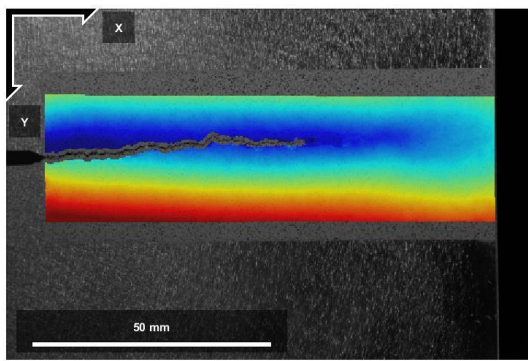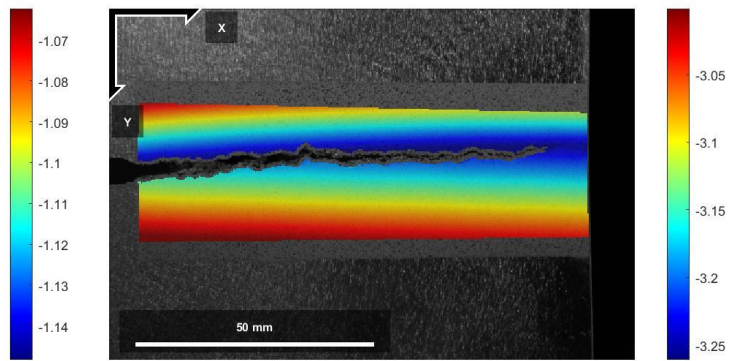Figure 9.27 Vertical strain field (ε_{yy}) for sample 1L: frame (a) 2, (b) 4, (c) 7, (d) 22.

(a)

(b)
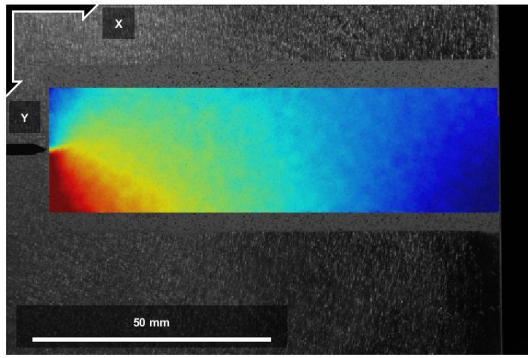
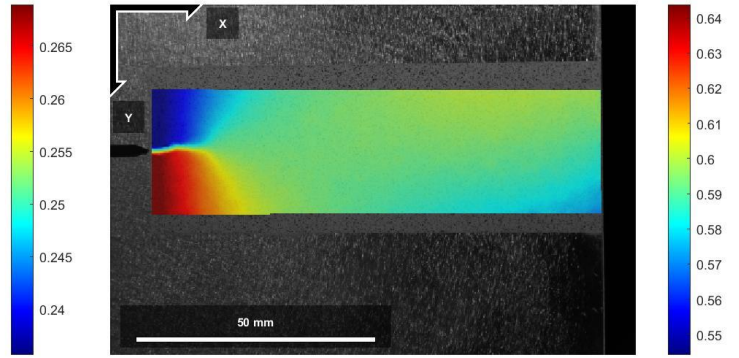(c)   (d)
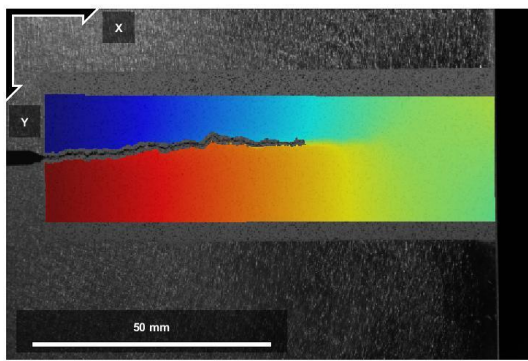
Figure 9.28 Horizontal (U) displacement field for sample 1L: frame (a) 2, (b) 4, (c) 7, (d) 22.
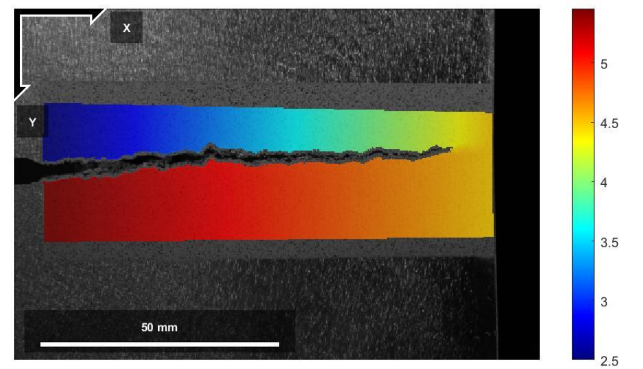
(a)

(b)

(c)   (d)

Figure 9.29 Vertical (V) displacement field for sample 1L: frame (a) 2, (b) 4, (c) 7, (d) 22.